Non-destructive Characterization of Materials by Single-sided NMR

Von der Fakultät für Mathematik, Informatik und Naturwissenschaften der
Rheinisch-Westfälischen Technischen Hochschule Aachen
zur Erlangung des akademischen Grades eines Doktors der Naturwissenschaften
genehmigte Dissertation

vorgelegt von

M.Sc. Nicolae-Octavian Goga

aus Satu Mare, Romania

Berichter: Universitätsprofessor Dr. Dr. h.c. Bernhard Blümich
Universitätsprofessor Dr. Dan E. Demco

Tag der mündlichen Prüfung: 20. August 2007
Diese Dissertation ist auf den Internetseiten der Hochschulbibliothek online verfügbar.

"I am not aware of any other field of science outside of magnetic resonance that offers so much freedom and opportunities for a creative mind to invent and explore new experimental schemes that can be fruitfully applied in a variety of disciplines."

~ Richard R. Ernst ~

Contents

1 Introduction **1**

2 Nuclear Magnetic Resonance **7**

2.1 Basic NMR 7

2.1.1 Magnetic resonance phenomenon 7

2.1.2 Magnetic and electric spin interactions 11

2.1.3 Magnetization relaxation 15

2.1.4 Spin coherences 18

2.1.5 Spin echoes 21

2.2 NMR imaging 25

2.2.1 Principles of NMR imaging 26

2.2.2 Spin system response in heterogeneous samples 28

2.2.3 Frequency encoding 29

2.2.4 Phase encoding 31

2.2.5 Sampling k-space 32

2.2.6 Contrast in NMR imaging 33

3 Single-Sided NMR **37**

3.1 Introduction 37

3.2 Inhomogeneous magnetic fields 38

3.3 Unilateral sensors – the NMR-MOUSE 40

3.3.1 Field profiles 41

3.3.2 Signal-to-noise ratio 43

4 Characterization of Materials by Single-Sided NMR 49

4.1 NMR of polymers 49

4.1.1 Cross-linked polymers 50

4.1.2 Network properties by transverse magnetization relaxation 52

4.1.3 Heterogeneities in rubbery materials 53

4.2 Unilateral NMR relaxometry 55

4.2.1 Method 56

4.2.2 Non-invasive quality control in the tire production 58

4.2.3 Relaxometry on aged PE pipes 63

4.2.4 In situ NMR at a stress-strain device 66

4.2.5 Mechanical testing versus NMR 69

4.3 Single-sided NMR imaging 77

4.3.1 Method 77

4.3.2 Imaging of polymers and biological materials 81

4.4 High resolution NMR profiling 89

4.4.1 Method 90

4.4.2 Single-sided NMR profiling of multi-layer objects 92

4.4.3 Surface UV aging of elastomers investigated with microscopic resolution by single-sided NMR 98

5 Conclusions 107

Appendix 113

References 115

Publications by the Author 128

Chapter 1

Introduction

There is a question I asked myself many times: What is our Universe made of? The simplest answer which inherently comes into my mind is: *particles in motion and their fields*. For the sake of simplicity, one might answer this question based on the "macroscopic" information available to human senses, eventually pointing to atoms and molecules, though, without thinking of those many interactions between them about which Einstein said: "All actions would cease if those powerful elemental forces were to cease stirring within us". Talking about the delicate motion of a magnetic particle in an external field, the Nobel Prize awarded Edward M. Purcell noticed: "It should reside in all the ordinary things around us, revealing itself only to him who looks for it"; and remembering the winter of his first successful NMR experiments while he started looking even on snow with new eyes: "There the snow lay around my doorstep - great heaps of protons quietly precessing in the earth's magnetic field. To see the world for a moment as something rich and strange is the private reward of many a discovery."

What can we learn from all these about the structure of matter? Let us begin with the most direct application of nuclear induction methods, the measurement of nuclear magnetic moments. The basis for this is the resonance condition

$$v = \frac{\mu \boldsymbol{H}_0}{Ih}, \tag{1.1}$$

in which v is the frequency of precession of the axis of the nuclear spin in a magnetic field of strength $\boldsymbol{H}_0$, and μ is the magnetic moment of the nucleus. The number I, is the

nuclear spin quantum number, an integer or half-integer, and h is Planck's constant. Now $\boldsymbol{H}_0$, except for a certain slight correction, is simply the field of the magnet in which the substance has been put, and it can be measured. The frequency of precession, is easily measured with high accuracy, and thus one can determine the quantity μ/Ih .

Regarding the motion of atomic nuclei in a magnetic field one finds in Nuclear Magnetic Resonance (NMR) a powerful tool to investigate structure and motion, and though not all nuclei possess a magnetic moment, one can hardly find an element without at least one isotope sensitive to magnetic fields. Thus, the world of the nuclear spins is a true paradise for theoretical and experimental physicists. It supplies, for example, most simple test systems for demonstrating the basic concepts of quantum mechanics and quantum statistics, and numerous textbook-like examples have emerged. On the other hand, the ease of handling nuclear spin systems predestinates them for testing novel experimental concepts. Indeed, the universal procedures of coherent spectroscopy have been developed predominantly in NMR and have found widespread application in a variety of other fields.

Prof. R. R. Ernst emphasized during his Nobel Lecture in 1992 [Ern1] the former great achievements in magnetic resonance honoured by physics Nobel prizes, "starting with the famous molecular beam experiments by Isidor I. Rabi [Rab1, Rab2, Rab3, Kel1] acknowledged in 1944, followed by the classical NMR experiments by Edward M. Purcell [Pur1] and Felix Bloch [Blo1, Blo2], honoured with the 1952 prize, and the optical detection schemes by Alfred Kastler [Bro1, Kas1], leading to a prize in 1966. Some further physics Nobel prize winners have been associated in various ways with magnetic resonance: John H. Van Vleck developed the theory of dia- and paramagnetism and introduced the moment method into NMR; Nicolaas Bloembergen had a major impact on early relaxation theory and measurements; Karl Alex Müller has contributed significantly to electron paramagnetic resonance; Norman F. Ramsey is responsible for the basic theory of chemical shifts and J couplings; and Hans G. Dehmelt has developed pure nuclear quadrupole resonance. But not only for physicists is nuclear magnetic resonance of great fascination. More and more chemists, biologists, and medical doctors discover NMR, not so much for its conceptual beauty but for its extraordinary usefulness."

Prof. R. R. Ernst himself received the Nobel Prize in Chemistry, in 1991, for the development of the one and two-dimensional NMR techniques. Consequently few more Nobel Prizes related to NMR have lately been given in other domains than physics i.e., Kurt Wüthrich received the Nobel Prize in Chemistry for NMR studies of structure and function of biological macromolecules in 2002 and the Nobel Prize in Medicine, has been awarded to Paul C. Lauterbur and Peter Mansfield in 2003, for their discoveries concerning magnetic resonance imaging. In this context, a great number of magnetic resonance tools have been invented to enhance the power of NMR in view of a variety of applications [Ern2, Bax1, Rah1, Cha1, Fri1, Mar1, Sch1, and Bre1].

The field of NMR has grown rapidly during the last ten years, not least because of the development of computers and sophisticated high-field NMR spectrometers. The concepts and directions in NMR have also changed a lot. Along with the development of high-field NMR spectrometers with ever increasing field strengths and homogeneities, a new fashion of NMR, namely that of the single-sided mobile sensors has vigorously developed.

The advantage of using unilateral sensors to specific problems was already proved in many domains like well logging, agriculture, material science, medicine, etc. Characterizing samples either too bulky (e.g. building materials [Sha1]) or unsuitable (e.g. ferromagnetic materials [Zim1]) to be placed in a conventional MR system posses a different challenge that has been met by unilateral NMR devices. The non-destructiveness and simplicity of the method, alongside low costs and portability of the sensor, have always represented a reason and impetus to use permanent magnets instead of expensive super-conducting magnets. As a consequence, the technology and use of mobile sensors progressed a lot in the last years broadening again the use of NMR. The direct acquisition domain today can encode one of many NMR parameters such as transverse relaxation, space, diffusion, velocity, or frequency. The indirect dimensions are interrogated in a repetitive fashion by filtering the magnetization detected directly and varying a filter parameter in a systematic fashion [Blü1, Blü2].

One of the first and most successful of unilateral NMR magnets was the NMR-MOUSE (Mobile Universal Surface Explorer) [Eid1], originally designed to conduct in situ investigations of rubber products (e.g. car tyres). The NMR-MOUSE is invariably constructed from permanent magnetic material, although it has passed through a series

of incarnations from its inception as a pair of semi-cylindrical magnets [Eid1]. These include the bar-magnet NMR-MOUSE [Blü3] and the most common variation: the U-shaped NMR-MOUSE [Anf1]. The NMR-MOUSE is most suited to the study of polymer materials such as natural rubber [Blü4] due to the ideal combination of long transverse relaxation times and slow molecular diffusion that they exhibit.

This work discusses some novel applications of single-sided NMR in domains like quality control, polymer science and bio-medicine. After introduction, the basic principles of NMR and NMR imaging are presented in Chapter 2, followed by an outline of the particularities of NMR in low and highly inhomogeneous fields in Chapter 3. Here a brief description of the U-shaped- and bar-magnet unilateral sensors is followed by a schematic presentation of their magnetic field profiles. Finally the sensitivity problem in single-sided NMR is discussed.

In Chapter 4, different strategies of using unilateral NMR in quality control, polymer science and bio-medicine are presented. The information on the structure, segmental dynamics, and material heterogeneities provided by the different NMR methods serves to correlate the microscopic properties of aged elastomers with the macroscopic material properties. In this way the mechanisms of chemical aging, physical fatigue and strain can be better understood on the molecular level. The chapter is divided in three main subchapters.

First (in Subsection 4.2), a simple NMR relaxometry method without any spatial encoding is presented. The method found some important applications like: quality control in the tyre production where the homogeneity of intermediate and final products can be directly measured during fabrication, the characterization of physical aging in PE water pipes, the quantification of elongation in strained elastomers in terms of NMR relaxation times as well as the establishment of correlation maps between NMR parameters and macroscopic properties (like elasticity and shear modulus). The latter exhibits special importance in the possibility to non-destructively appreciate by a simple NMR relaxometry experiment the macroscopic properties of the material in objects which do not fit the specific test devices but can be measured with a usual NMR-MOUSE.

Conventional Magnetic Resonance Imaging (MRI) has been developing since 1973 [Lau1, Man1], predominantly in the field of medical research and diagnosis where

three-dimensional anatomical images are now routinely obtained. The images are required to show a high level of image contrast between different tissue types, while the accurate quantitative measurements of parameters (spin density, relaxation times, etc.) are more rarely used to characterize the tissue. Moreover, in materials science studies, there is often less intrinsic value in obtaining three-dimensional images. Rather one seeks to quantitatively measure properties of the sample with sufficient spatial localization so as to characterize either the sample or a sample-process. In Subsection 4.3, the strategy developed to incorporate spatial resolution on single-sided sensors, is summarized. The two-dimensional (2D) and three-dimensional (3D) NMR imaging techniques which can be considered as special forms of multidimensional NMR will be introduced by discussing principles and image contrast. Examples of unilateral NMR imaging of elastomers and biological materials are given by a number of applications that illustrate the performance of the technique in fields like quality control, bio-medicine and material science.

Multi-dimensional imaging has the advantage of providing a plausible view of the object. However, in practice we have found that in many cases the structure of the sample under study changes only along one direction. In such cases one prefers high resolution along one direction instead of 2D or 3D spatial discrimination. In some respects profiling rather than imaging simplifies the experimentation, although this is offset by the fact that most samples of interest are solid, semi-solid, or solid-like (that is, characterised by a short signal lifetime, T_2), unlike the soft tissues studied in medical imaging. The broad linewidths (and hence short life-times) of NMR signals associated with solids makes the imaging process far more difficult.

To resolve the depth structure with high depth resolution a strong and highly uniform static gradient is required. The stable, high magnetic field gradient is sufficient to overcome the broad line-widths of the solid materials allowing samples to be profiled with increased spatial resolution. Recently, microscopic resolution has been obtained with the NMR-MOUSE by mounting the device on a mobile platform, akin to a stray field (STRAFI) imaging probe, except that the magnet is now moved relative to the sample [Per1] rather than vice versa. The “sweet-spot” within this inhomogeneous magnetic field of the sensor can be used to target a sensitive plane in a sample while the plane is stepped through the sample to provide a profile. This technique can be applied

to arbitrarily shaped or large samples by using unilateral magnets to target spatially localized near-surface planes.

In Subsection 4.4 we describe the profiling technique that takes advantage of the strong uniform gradient generated by an optimized magnet geometry to achieve high depth resolution into the object [Per1, Cas1]. This profiling technique quickly found important applications in resolving multilayered structures, where even dynamic processes happening at the surface of the sample as a consequence of an exposure to the environment can be followed in real time.

The main topic of this subsection is the application of the high resolution profiling technique in the study of the interaction of UV irradiation with the elastomer network. High resolution ^{1}H NMR depth profiles have been obtained near the surface of a natural rubber sample after exposing it to UV radiation for several days. An NMR observable related to the sum of the spin echoes in the Carr-Purcell-Meiboom-Gill (CPMG) echo decay was used to characterize the cross-link density changes produced by the action of the UV radiation. The aging profiles were interpreted for the first time based on a model in which the radiation absorption coefficient exponentially depends on the depth in the material. The method can be applied to investigate the effect of other aging agents on the surfaces of elastomers.

Chapter 2

Nuclear Magnetic Resonance

Nuclear magnetic resonance is a physical phenomenon utilized to investigate the molecular properties of matter by irradiating atomic nuclei in a magnetic field with radio waves [Blü5]. The phenomenon is based on the special property of the atomic nucleus, called the magnetic spin moment. Some nuclei posses such a magnetic spin and others do not. When the nuclei which have this property are immersed in a static magnetic field ($\boldsymbol{B}_0$) and then exposed to a second oscillating magnetic field ($\boldsymbol{B}_1$), the NMR phenomenon occurs.

2.1 Basic NMR

2.1.1 Magnetic resonance phenomenon

Magnetic resonance is a branch of spectroscopy that detects the quantum-mechanical transitions induced by electromagnetic radiation in a system of discrete energy levels of electrons or nuclei placed in a static magnetic field. Nuclear magnetic resonance (NMR) employs electromagnetic waves in the radio-frequency range between 1 GHz and 2 kHz.

Nuclear magnetic resonance is one of the most powerful methods for structural and dynamics investigation of matter in different states of aggregation due to the

following features: (*1*) the interactions of nuclear magnetic moments are very weak compared with the thermal energy, therefore, we deal with nuclear paramagnetism. Moreover, the energy delivered by the radio-frequency generator is much larger than the strength of the inter-nuclear couplings. That leads to the possibility to manipulate these interactions in a specific way and to simplify the spectral response. (*2*) The radio-frequency photons have much lower energy than the energy of chemical bonds, therefore, the interaction of electromagnetic radio-frequency (rf) radiation with matter, especially bio-molecules is non-ionising. (*3*) The number of radio-frequency photons with a specific frequency is very large. Hence, the phase of the associated electromagnetic wave is very well defined. The high degree of coherence of radio-frequency radiation is essential for implementation of NMR experiments including magnetic resonance imaging (MRI). The appearance of NMR spectra, and consequently the molecular structure they are able to provide, arises from the discrete nature of the energy levels pertaining to a nuclear spin system. The energy levels are mainly a result of the Zeeman interaction $-\boldsymbol{\mu}\cdot\boldsymbol{B}_0$ between the static magnetic field of induction $\boldsymbol{B}_0$ and the nuclear magnetic moment $\boldsymbol{\mu}$. The quantum-mechanical quantity called spin momentum $\boldsymbol{I}$ is related to the magnetic moment by $\boldsymbol{\mu}=\gamma\mathrm{h}\boldsymbol{I}$, where γ is the magnetogyric ratio and h is the Planck constant divided by 2π. In the absence of the magnetic field the nuclear spin states are degenerated (see Fig. 1a). The application of a static magnetic field $\boldsymbol{B}_0$ induces a magnetic interaction described by the Zeeman Hamiltonian $\boldsymbol{H} = -\boldsymbol{\mu}\boldsymbol{B}_0$. Taking the magnetic field orientation to be along the *z*-direction we get

$$\boldsymbol{H} = -\gamma\mathrm{h}\boldsymbol{B}_0\boldsymbol{I}_\mathrm{z}. \tag{2.1}$$

The eigenvalues $\boldsymbol{E}_m$ of this Hamiltonian can be evaluated from the Schrödinger equation

$$\boldsymbol{H}\left|m\right\rangle = -\gamma\mathrm{h}\boldsymbol{B}_0 m\left|m\right\rangle, \tag{2.2}$$

where $\left|m\right\rangle$ is the eigenstate corresponding to the eigenvalue $\boldsymbol{E}_\mathrm{m} = -\gamma\mathrm{h}\boldsymbol{B}_0 m$. The magnetic quantum number is m where $m = I, I\text{-}1,\ldots,\text{-}I$. Therefore, the equidistant energy differences for the single-quantum transitions $\Delta m = \pm 1$ are given by

$$\Delta\boldsymbol{E} = \mathrm{h}\omega_0, \tag{2.3}$$

where the Larmor frequency is $\nu_0 = \nu_L = \omega_0 / 2\pi$. The energy level diagrams of a spin $\boldsymbol{I} = 1/2$ and $\boldsymbol{I} = 1$ are shown in Figure 1.

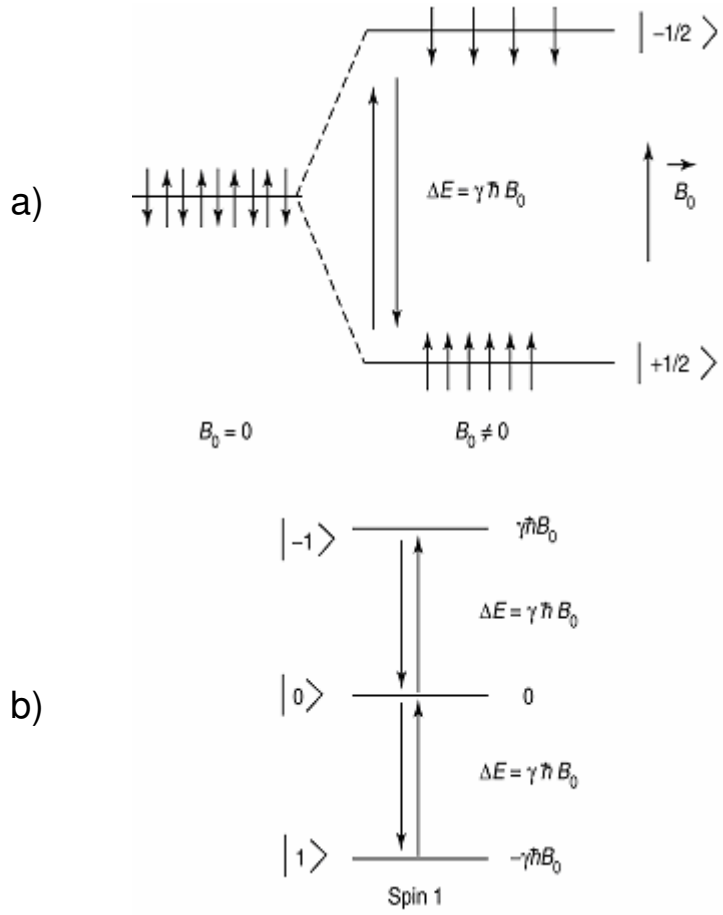

Fig. 2.1 a) Energy levels diagram and allowed transitions of an ensemble of spins with $\boldsymbol{I}$=1/2 in the absence and the presence of $\boldsymbol{B}_0$. The small arrows indicate the orientation of nuclear spins relative to $\boldsymbol{B}_0$. b) Energy diagram and allowed single-quantum transitions for spins with I=1 (Reproduced from ref. [Dem1]).

Another important ingredient for a magnetic resonance experiment is the rf field. Only the magnetic component of the electromagnetic field, i.e., $\boldsymbol{B}_1(t) = \boldsymbol{B}_{10}\cos(2\pi\nu t)$ interacts with the magnetic moment of the nuclei. The amplitude of the rf field is $\boldsymbol{B}_{10}$ and ν is the carrier frequency. This field is produced by a rf coil and leads to a perturbation Hamiltonian [Dem1]

$$\mathbf{H}_P(t) = -\gamma \mathrm{h} \boldsymbol{B}_{10} \cdot \boldsymbol{I} \cos(2\pi\nu t). \tag{2.4}$$

From the time-dependent perturbation theory of quantum-mechanics, it can be stated that a transition between two states $|\Psi\rangle$ and $|\Phi\rangle$ is allowed provided that $\langle\Psi|\mathbf{H}_{\mathrm{P}}|\Phi\rangle \neq 0$. This takes place if $\nu \approx \nu_0$ (i.e., the resonance condition) and the alternative magnetic field $\boldsymbol{B}_1(t)$ is polarized perpendicular to the static magnetic field $\boldsymbol{B}_0$. Concerning a spin $\boldsymbol{I} = 1$ (Fig. 1b), a similar calculation show that only the single-quantum transitions $|0\rangle \rightarrow |1\rangle$ and $|-1\rangle \rightarrow |0\rangle$ (and those in the opposite directions) are allowed in first order approximations and occur at the same frequency, given by Eq. 2.3.

The spin system evolution in the presence of the interspin couplings has to be quantified in the language of quantum-mechanics. This is a reflection of the quantum-mechanical nature of the spins and the fact that the spin couplings encode NMR observables via propagation operators. Nevertheless, nuclear magnetization relaxation processes are described in a semi-classical approach where the thermal bath is treated classically and the spin system quantum-mechanically.

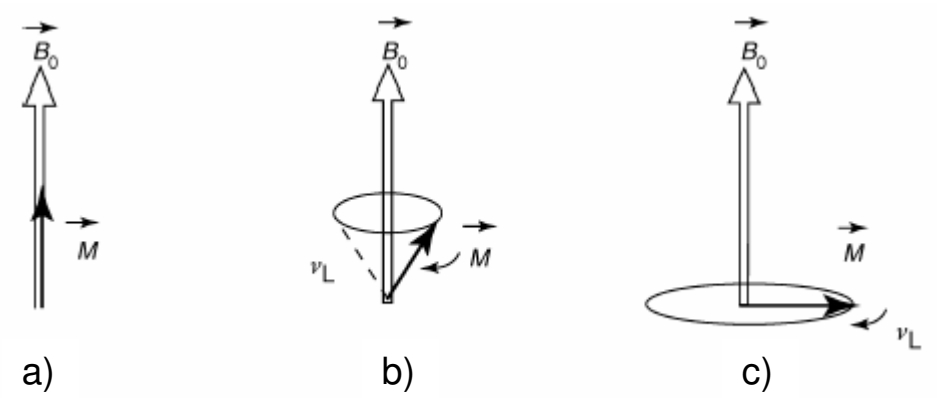

Fig. 2.2 a) At thermal equilibrium, the nuclear magnetization $\boldsymbol{M}$ is collinear with $\boldsymbol{B}_0$. b) Under the action of an electromagnetic perturbation, $\boldsymbol{M}$ is displaced from its equilibrium position. It undergoes precessional motion around $\boldsymbol{B}_0$ at the Larmor frequency $\nu_L=\nu_0$. c) After the action of a 90° rf pulse the magnetization $\boldsymbol{M}$ is brought into a plane transverse to $\boldsymbol{B}_0$.

In general, the NMR experiments are performed at high temperatures employing a large number of spins. These features lead to the possibility to treat some aspects of the experiments classically. The excess of spins oriented along the static magnetic field $\boldsymbol{B}_0$ with respect to those oriented in the opposite direction (c.f. Fig. 2.1a) results in a macroscopic nuclear magnetization $\boldsymbol{M}$ aligned along the static magnetic field, which is

called equilibrium magnetization (cf Fig. 2.2a). It can be displaced from this equilibrium by an appropriate perturbation, for instance, by a rf excitation. It is then subject to a precessional motion around $\boldsymbol{B}_0$ with the Larmor frequency ν_L (Fig. 2.2b). The electromagnetic perturbation which brings $\boldsymbol{M}$ into a plane perpendicular to $\boldsymbol{B}_0$ allows the observation of the Larmor precession through an electromotive force which occurs in a coil whose axis is contained in that plane (Fig. 2.2c). This can be done by rotation of the nuclear magnetization using a resonant 90° rf pulse. The nuclear magnetization $\boldsymbol{M}$ can be oriented anti-parallel to $\boldsymbol{B}_0$ by the action of a 180° pulse. The majority of NMR experiments uses pulse sequences composed of 90° and 180° rf pulses.

2.1.2 Magnetic and electric spin interactions

The nuclear spins can experience various external and internal interactions. These interactions can have magnetic or electric origin. The external interactions are, in general, represented by the Zeeman interactions with static and rf magnetic fields. The chemical shielding, dipole–dipole, spin–spin indirect coupling or *J*-coupling, spin-rotation, and hyperfine couplings represent the major internal magnetic interactions. The quadrupolar interaction has an electrostatic character. All these interactions have a tensorial character, i.e., they depend on the orientation of the principal axes of the tensor relative to the direction of $\boldsymbol{B}_0$. They are relevant to solid polymers below and around the glass transition temperatures. For polymers in solution or for soft polymers fast molecular motions average these anisotropic interactions to isotropic or residual values which can be close to zero.

The separation of the energy levels of the nuclear spin states and of course the resonance frequencies are determined by the spin interaction strengths. The Hamiltonian operator $\mathbf{H}$ of the spin system is the sum of all operators for each individual interaction

$$\mathbf{H} = \mathbf{H}_Z + \mathbf{H}_Q + \mathbf{H}_{rf} + \mathbf{H}_D + \mathbf{H}_\sigma + \mathbf{H}_J, \tag{2.5}$$

where *Z*-indicates the Zeeman interaction, *Q*-the quadrupole interaction, *rf*- the coupling of the spins to the radio frequency field, *D*- the dipole-dipole interaction, σ - the

chemical shift, and *J*-the indirect coupling. The energy levels are the eigenvalues (characteristic numbers) of this operator $\mathbf{H}$.

The Zeeman interaction is the coupling of the nuclear spins to the applied magnetic field. The Zeeman interaction defines the nuclear polarization as:

$$\mathbf{H}_Z = C^Z \mathbf{I}\mathbf{E}\boldsymbol{B}_0, \tag{2.6}$$

where $\mathbf{E}$ is the unit matrix and represents the coupling tensor between the spin vector operator $\mathbf{I}$ and applied magnetic field $\boldsymbol{B}_0$. The factor C^Z is given in Tab. 1 [Blü1]. The NMR frequency ω_0 is defined by the energy level splitting resulting from $\mathbf{H}_Z$.

At high field, *the quadrupole interaction* is the second largest interaction after the Zeeman interaction. It is given by:

$$\mathbf{H}_Q = C^Q \mathbf{I}\boldsymbol{Q}\mathbf{I} \tag{2.7}$$

This interaction is a valuable sensor of the electronic structure. Nuclei with spin quantum number I higher than ½ possess a so called quadrupole moment which couples to the electric field gradient established by the electrons surrounding the nucleus. The interaction is quadratic with respect to the spin vector $\mathbf{I}$ and it is described by the quadrupole coupling tensor $\boldsymbol{Q}$. A quadrupole splitting of the energy levels cannot be observed under fast isotropic motion as in liquids but can be observed in rigid aromatic and aliphatic compounds.

Table 2.1. C^λ factors and symbols of the coupling parameters.

Interaction	λ	C^λ	R^λ	δ_λ	η_λ
Zeeman	Z	$-\gamma$	1	-	-
quadrupole	Q	eQ/[2I(2I-1)η]	0	eq	η_Q
rf	*rf*	$-\gamma$	1	-	-
dipole-dipole	d	$-\mu_0\gamma_i\gamma_j/(4\pi)$	0	r_{ij}^{-3}	0
magnetic shielding	σ	γ	σ	$(2/3)\Delta_\sigma$	η_σ
indirect coupling	J	1	J	$(2/3)\Delta_j$	η_j

The interaction of a nuclear spin with the applied radio-frequency field enables excitation of detectable signal in NMR experiments. This interaction has an analogue

operator with the operator of the Zeeman interaction. The radio-frequency coupling is given by:

$$\mathbf{H}_{rf}(t) = C^{rf}\mathbf{I}\mathbf{E}\boldsymbol{B}_1(t). \tag{2.8}$$

The rf field of strength $\boldsymbol{B}_1(t)$ is applied in the *xy* plane of a laboratory coordinate frame, for example along *x*-axis. In order to have a dominant $\mathbf{H}_{rf}$ over all other interactions except for the Zeeman interaction, it is desirable to apply a strong $\boldsymbol{B}_1$ field.

The dipole-dipole interaction describes the through-space coupling of two magnetic moments. The Hamiltonian operator for this interaction is given by:

$$\mathbf{H}_{\mathrm{d}} = C^{D}\mathbf{I}^{i}\boldsymbol{D}\mathbf{I}^{j}, \tag{2.9}$$

where $\mathbf{I}^{i}$ and $\mathbf{I}^{j}$ are the spin vector operators of the coupling nuclei *i* and *j*. The coupling energy depends on the cube of the inverse separation r_{ij} and this is a highly valuable source of information about the structural geometry of molecules. This interaction is useful for measuring the internuclear distances in solids.

When an externally magnetic field is applied it is shielded at the site of the nucleus by the surrounding electrons. This is called *magnetic shielding*. The resultant local field is given by:

$$\boldsymbol{B} = (1-\boldsymbol{\sigma})\boldsymbol{B}_0, \tag{2.10}$$

where $\boldsymbol{\sigma}$ is the shielding tensor and its average value can be observed in liquids and solids. The shielding depends on the strength of the magnetic field $\boldsymbol{B}_0$. Its Hamilton operator is given by:

$$\mathbf{H}_{\sigma} = C^{\sigma}\mathbf{I}\boldsymbol{\sigma}\boldsymbol{B}_0. \tag{2.11}$$

The isotropic magnetic shielding determines the chemical shift in high-resolution NMR. The resonance frequency ω_{L} is not the same with the NMR frequency ω_0 of the nucleus. The relationship between the two frequencies is given by:

$$\omega_{\mathrm{L}} = (1-\sigma)\omega_0 = 2\pi\nu_{\mathrm{L}}. \tag{2.12}$$

Generally, as the NMR frequency of isolate nuclei cannot be readily measured, the chemical shift is tabulated with reference to a standard. In most of cases, this standard is the resonance frequency of the proton in the TMS (tetra-methyl-silane) molecule. The chemical shift is given by:

$$\delta = \frac{\nu_{\mathrm{L}} - \nu_{\mathrm{standard}}}{\nu_{\mathrm{standard}}} (ppm). \tag{2.13}$$

The indirect coupling is mediated by a polarization of the orbital angular momentum of the electrons. This phenomenon is rather weak in the homonuclear case of light nuclei but it can increase in heteronuclear cases for heavy atoms. The indirect coupling is difficult to be observed in solid-state NMR of organic compounds because of the larger linewidth in solids. Analogue to the dipole-dipole interaction, the Hamiltonian operator for this interaction is given by:

$$\mathbf{H}_J = C^J \mathbf{I}^i \boldsymbol{J} \mathbf{I}^j \tag{2.14}$$

where $\mathbf{I}^i$ and $\mathbf{I}^j$ are the spin vector operators of the coupling nuclei. In this case the trace of the coupling tensor $\boldsymbol{J}$ is different from zero, and contrary to the dipole-dipole interaction the indirect coupling can be observed also in liquids. The energy levels are often intricately split by the $\boldsymbol{J}$ coupling which results in the hyperfine structure of the high-resolution spectra.

In strong magnetic fields, the Zeeman interaction determines the resonance frequencies. Supposing that the other interactions are simple perturbations, the coupling to the radio-frequency field, the chemical shift, the dipole-dipole interaction and the J-coupling can be treated mostly by the first-order perturbation theory. In the case of the quadrupole interaction, this method works exclusively for small quadrupole moments.

In the studies of elastomers by NMR experiments, dipolar and quadrupolar interactions are mainly used. The presence of the high magnetic field imposes a manipulation of the spin system which separates certain parts of the spin interaction Hamiltonian. This process is called truncation and the secular dipolar Hamiltonian of two spins *i* and *j* has the general form [Dem1]:

$$\mathbf{H}_{\mathrm{d}}^{(0)} = -\left(\frac{\mu_0}{4\pi}\right)\frac{\gamma_{\mathbf{I}^i}\gamma_{\mathbf{I}^j}}{r_{ij}^{\,3}}\frac{1}{2}\left(3\cos^2\theta_{\mathbf{I}^i\mathbf{I}^j} - 1\right)\left(3\mathbf{I}^i{}_z\mathbf{I}^j{}_z - \mathbf{I}^i \cdot \mathbf{I}^j\right). \tag{2.15}$$

The factor $\mu_0 / 4\pi$, where μ_0 is the magnetic susceptibility of vacuum, has been introduced in conformity with MKSA units. The magnetogyric ratios are $\gamma_{\boldsymbol{I}}$ and $\gamma_{\boldsymbol{S}}$. The space encoded part of the dipolar Hamiltonian depends on the distance r_{ij} of spins i and

j and the angle $\theta_{\mathbf{I}^i}$ between r_{ij} and $\boldsymbol{B}_0$. The anisotropic segmental motions average the space part of $\mathbf{H}_{\mathrm{d}}^{(0)}$ to a residual value.

Finally, the truncated form of the axially symmetric quadrupolar Hamiltonian for nuclei with spin I larger than 1/2 can be expressed as

$$\mathbf{H}_{\mathrm{Q}}^{(0)} = \boldsymbol{C}_{\mathrm{Q}}\left[3\mathbf{I}_z^{\,2} - \mathbf{I}^2\right]. \tag{2.16}$$

The quadrupolar coupling $\boldsymbol{C}_{\mathrm{Q}}$ is defined by

$$\boldsymbol{C}_{\mathrm{Q}} = \frac{e\boldsymbol{Q}\boldsymbol{V}_{\mathrm{ZZ}}}{4h\mathrm{I}(2\mathrm{I}-1)}, \tag{2.17}$$

where $e\boldsymbol{Q}$ is the quadrupolar moment of a specific isotope and $\boldsymbol{V}_{\mathrm{ZZ}}$ is the Z component of the electric field tensor at the position of the nucleus. In the presence of anisotropic molecular motions, the electric field gradient tensor is averaged to a residual value.

The spin interactions can be classified as inhomogeneous and homogeneous [Meh1]. The NMR spectrum generated by the inhomogeneous spin interaction which is linear in the spin operator $\mathbf{I}_z$, is a sum of independent individual lines. A selective rf irradiation can saturate only a group of spins producing a hole in the spectrum. For the homogeneous lines of a compact sample the NMR spectrum is a sum of individual lines with no shift with respect to each other. The spin interactions bilinear in the spin operators generate these spectra. However, for a powder, the two-spin dipolar interaction produces an inhomogeneously broadened line. The excitation of the spectrum with a selective pulse will affect all the spectral frequencies.

2.1.3 Magnetization relaxation

One of the important sources of information about molecular motions is related to the relaxation of the longitudinal ($\boldsymbol{M}_z$) and transverse ($\boldsymbol{M}_x$ and $\boldsymbol{M}_y$) components of the macroscopic nuclear magnetization. The molecular motions modulate the spin interactions that lead to the exchange of energy between the nuclear energy levels and the lattice or thermal bath represented by the molecular degree of freedom. This process is described by a time constant T_1 the so-called longitudinal relaxation time. The

dephasing of the transverse magnetization components $\boldsymbol{M}_x$ and $\boldsymbol{M}_y$, which is related to the increase of the entropy of the spin system is described by the transverse relaxation time T_2. The molecular motions responsible for the relaxation include: (*1*) overall translational and rotational motions, (*2*) local motions such as internal rotations around C–C bonds or molecular axe of symmetry or segmental motions of polymer chains, and (*3*) exchange between two different distinct chemical sites within the same molecule or different molecules.

In the simplest assumption, the time evolution of the nuclear magnetization under relaxation processes can be described by the Bloch equations (see [Blü1], and references therein)

$$\frac{\mathrm{d}\boldsymbol{M}_{\mathrm{x,y}}(t)}{\mathrm{d}t} = \frac{\boldsymbol{M}_{\mathrm{x,y}}}{T_2},$$
$$\frac{\mathrm{d}\boldsymbol{M}_{\mathrm{z}}(t)}{\mathrm{d}t} = -\frac{\boldsymbol{M}_{\mathrm{z}}(t) - \boldsymbol{M}_0}{T_1}, \tag{2.18}$$

where $\boldsymbol{M}_0$ is the magnetization of the spin system in the thermodynamic equilibrium. The time evolution of $\boldsymbol{M}(t)$ vector under relaxation processes described by equation 2.18 is given by exponential functions. This approximation is not valid in many cases for polymer or other macromolecular systems where complex relaxation mechanisms are present [Del1, Tyc1]. In such cases, a complete treatment requires additional relaxation parameters such as cross-relaxation rates [Del1, Tyc1, Can1, Ern2]. Such a situation occurs whenever the interaction between two spins A and X is characterized by random fluctuations. For this cross-relaxation process A spin magnetizations induces a modification of X magnetization which contributes to the specific evolution of X magnetization. More formally, this coupling can be expressed via the Solomon equations (see for instance, ref. [Can1]) which contain besides the longitudinal relaxation rates of spins A and X also a cross-relaxation rate which reflects the coupling between the A and X spin magnetizations. Several two-dimensional NMR experiments (see below) can measure cross-relaxation rates that enhance our knowledge about molecular motions in complex systems [Can1, Ern2].

The longitudinal magnetization relaxation can be measured using different methods [Blü1, Can1, Kim1, Cal1] based on the scheme:

Initial perturbation — *Evolution* — *Detection*

The initial perturbation brings the spin system into a non-equilibrium state and can be represented by an inversion pulse of 180° (i.e., $\boldsymbol{M}_z(0) \rightarrow -\boldsymbol{M}_0$) or a saturation train of 90° (ie, $\boldsymbol{M}_z(0) = 0$). The detection is performed by a standard 90° pulse under low or high resolution conditions.

The transverse relaxation measurements are performed using a Hahn echo (see below) or Carr–Purcell–Meiboom–Gill (CPMG) pulse sequences [Blü1, Cal1]. The first method uses the pulse scheme: $90^{\circ}_{x} - \tau - 180^{\circ}_{x,y} - \tau -$ Hahn echo and measures the time evolution of the amplitude of the Hahn echo as a function of the echo time 2τ. The CPMG scheme, $90^{\circ}_{x} - [\tau - 180^{\circ}_{y} - \tau -$ Hahn echo$]_N$ allows measuring the transverse magnetization decay in a single scan using a train of *N* Hahn echoes.

The mechanisms of relaxation are produced by local magnetic fields originating from randomly fluctuating spin interactions like homonuclear or heteronuclear dipolar, quadrupolar, and chemical shielding interactions. They induce quantum-mechanical transitions in the Zeeman energy level manifold, whose effect takes the nuclear magnetization back to the equilibrium configuration. When performing a spectral decomposition of these fluctuating local fields $h(t)$ (which are in general, tensorial quantities), we can find a nonzero component frequencies equal to those of the various transitions which exist within the Zeeman energy level diagram. The efficiency of the local magnetic fields to induce transitions can be appreciated by quantities named spectral densities of the form [Dem1]

$$\boldsymbol{J}_i(\omega) = \int_0^{\infty} \overline{h_i(t)h_i(0)} \exp(-\mathrm{i}\omega t)\mathrm{d}t, \tag{2.19}$$

where $h_i(t)$ is the random fluctuating *i* component of the local fields. The bar denotes an average over the ensemble of spin systems. On the other hand, a quantum-mechanical transition can be induced by a fluctuating local field given that a certain degree of coherence is present. The autocorrelation function $C(t) = \overline{h_i(t)h_i(0)}$ is indicative of this coherence that essentially persists for a time equal to the correlation time τ_c. A more

general correlation function is represented by the space–time autocorrelation function $C(x,t)$, where x is a general spatial coordinate meant to represent translational or rotational coordinates. These correlation functions turn out to be necessary in the context of characterizing of two-dimensional exchange spectra [Sch2]. Moreover, a three-dimensional spectrum may provide a three-time distribution, which contains information that cannot be directly retrieved from a 2D exchange spectrum. More detailed information on the nature of the nonexponential loss of correlation in polymers can be obtained from reduced four-dimensional (4D) exchange spectra which is not accessible in the corresponding one-dimensional (1D) relaxation measurements and the 2D exchange spectrum [Sch2].

Molecular processes with a single correlation time are rarely found in partially or strongly disordered solids like semicrystalline or amorphous polymers. A distribution $g(\tau)$ of the correlation times τ has to be introduced in order to evaluate the correlation function [Sch2, Dem1], i.e.,

$$C(\mathrm{t}) = \int_0^\infty \exp\left\{-\frac{t}{\tau}\right\} \mathrm{g}(\tau)\mathrm{d}\tau. \tag{2.20}$$

Such distribution has been shown to span several orders of magnitude for instance in the case of local motions in the glassy state. Instead of the distribution function, other fitting functions for the correlation function $C(t)$ are considered. One of these functions is the stretched exponential Kohlrausch–Williams–Watts function $\exp\left\{-\left(t/\tau_{\mathrm{kww}}\right)^{\beta}\right\}$ that has been found to fit the data quite universally [Sch2, Dem1].

2.1.4 Spin coherences

In all NMR experiments the spin system evolves under internal and external spin interactions. For isolated spins, the spin dynamics can be described in terms of the motion of classical magnetization vectors. Many structural and molecular dynamics problems in NMR involve coupled spins. In this case, it is necessary to recourse to a quantum-mechanical formalism where a density operator describes the state of the system [Ern2]. The density operator $\rho(\mathrm{t})$ is derived from a wave function which describes a so-called mixed state. This state corresponds to a statistical ensemble of

quantum-mechanical objects, which in our case is a collection of nuclei with magnetic moments. Therefore, the statistics specific of these objects and the statistics of an ensemble are simultaneously present. The equation of motion for the density operator is given by the Liouville–von- Neumann equation

$$\mathrm{i}\frac{\partial\rho(t)}{\partial t} = [\mathbf{H}(t), \rho(t)], \tag{2.21}$$

where $\mathbf{H}(t)$ is the Hamiltonian or total energy operator of the system expressed in angular frequency units, which may itself be time dependent.

In general, equation 2.21 does not have an exact solution. Several mathematical methods have been applied to obtain an approximate solution for $\rho(\mathrm{t})$ one of the most efficient and being the Floquet technique [Ern2]. The dynamics of the spin system detected via an observable $\langle \mathbf{O}(t) \rangle$ described by a quantum-mechanical operator $\mathbf{O}$ can be evaluated by

$$\langle \mathbf{O}(t) \rangle = \mathrm{Tr}\{\mathbf{O}\rho(t)\} \tag{2.22}$$

Thus, the expectation value is found by evaluating the trace of the product of the observable operator and the density operator.

A particularly simple interpretation of the density matrix is possible in the eigenbase of the Hamiltonian $\mathbf{H}$. The diagonal element ρ_{rr} is equal to the probability that the spin system is found in the eingenstate $|r\rangle$. The population of state $|r\rangle$ is P_{r} and therefore, $\rho_{\mathrm{rr}} = P_{\mathrm{r}}$. The off-diagonal element is defined by

$$\rho_{\mathrm{rs}} = \langle r|\rho(t)|s\rangle = \overline{c_{\mathrm{r}}(t)c_{\mathrm{s}}^{*}(t)}, \tag{2.23}$$

where the bar indicates an ensemble average. These elements describe a coherent superposition of eigenstates $c_{\mathrm{r}}(t)|r\rangle + c_{\mathrm{s}}(t)|s\rangle$ in the sense that the time dependence and the phase of the various members of the ensemble are correlated with respect to $|r\rangle$ and $|s\rangle$. Such a coherent superposition is simply called coherences. A spin coherence can be associated with a transition between two eigenvalues specified by the eigenstates $|r\rangle$ and $|s\rangle$. If the two states span an allowed transitions with a difference in magnetic

quantum numbers $\Delta M_{rs} = M_r - M_s = \pm 1$, the coherences ρ_{rs} are related to the NMR observables represented by the transverse magnetization components $M_x^{(rs)} \pm iM_y^{(rs)}$. In general, a matrix element of the density operator ρ_{rs} represents p-quantum coherence for which $p = M_r - M_s$, which, for $p \neq \pm 1$, does not lead to observable magnetization and can only be detected indirectly by two-dimensional spectroscopy [Ern1, Mun1].

The density operator $\boldsymbol{\rho}(t)$ has been formulated for the entire quantum-mechanical system. For magnetic resonance applications, it is usually sufficient to calculate expectation values of a restricted set of operators which act exclusively on nuclear variables. The remaining degrees of freedom are referred to as "lattice". The reduced spin density operator is defined by $\boldsymbol{\sigma}(t) = \mathrm{Tr}_l\{\boldsymbol{\rho}(t)\}$, where Tr_l denotes a partial trace over the lattice variables. The reduced density operator can be represented as a vector in a Liouville space of dimension n^2, i.e. [Dem1]

$$\boldsymbol{\sigma}(t) = \sum_{r}^{1,n^2} b_r(t)\boldsymbol{B}_r, \tag{2.24}$$

where n is the dimension of the Hilbert space of all admissible state functions and $\{\boldsymbol{B}_r\}$ is a complete set of orthogonal base operators. A proper selection of this base is often essential to ease the solution of a particular spin dynamics problem. For instance, for systems with spins $I_k = 1/2$ the product of the Cartesian spin operators is a convenient base operator [Ern1, Lev1]. As an example, the complete set of product operators $\{\boldsymbol{B}_r\}$ for two $\boldsymbol{J}$ or dipolar coupled nuclei with spin $I = 1/2$ consists of $2^{2\times 2} = 16$ operators, i.e.,

$$\begin{gathered} \frac{1}{2}\mathbf{E} \text{ (}\mathbf{E}\text{ is the unity operator), } \boldsymbol{I}_{ix}, \boldsymbol{I}_{iy}, \boldsymbol{I}_{iz}, \\ 2\boldsymbol{I}_{ix}\boldsymbol{I}_{jx},\ 2\boldsymbol{I}_{iy}\boldsymbol{I}_{jy},\ 2\boldsymbol{I}_{iz}\boldsymbol{I}_{jz},\ 2\boldsymbol{I}_{ix}\boldsymbol{I}_{jy},\ 2\boldsymbol{I}_{ix}\boldsymbol{I}_{jz}, \text{ for } i, j = 1, 2. \end{gathered} \tag{2.25}$$

The spin modes described by the product operators of expression 2.25 are the matrix elements of the density operator

$$\boldsymbol{\rho} = \begin{pmatrix} P_1 & \mathrm{SQ} & \mathrm{SQ} & \mathrm{DQ} \\ \mathrm{SQ} & P_2 & \mathrm{ZQ} & \mathrm{SQ} \\ \mathrm{SQ} & \mathrm{ZQ} & P_3 & \mathrm{SQ} \\ \mathrm{DQ} & \mathrm{SQ} & \mathrm{SQ} & P_4 \end{pmatrix} \tag{2.26}$$

The above product operators can be detected by properly designed NMR experiments [Ern1, Mun1] and reflect different features of the spin systems related to the structure, spin interaction topology, and molecular dynamics. The most popular spin modes are represented by the single-quantum coherences (SQ) of spin *i*, $\boldsymbol{I}_{ix}$ and $\boldsymbol{I}_{iy}$ that are related to the *x*- and *y*-magnetizations, respectively. Two-spin coherences of spin *i* and *j* consist of superposition of $p = 0$ (zero-quantum (ZQ)) and $p = \pm 2$ (double-quantum (DQ)) quantum coherences. The former is insensitive to the inhomogeneity of the magnetic field and the latter reflects the existence of spin couplings. Not only the existence of ***J***- or dipolar couplings can be detected by editing DQ coherences but also the strength of these couplings can be measured including internuclear distances and dihedral angles [Lev1, Sch3, Bro2].

2.1.5 Spin echoes

The evolution of spin coherences under non-fluctuating spin interactions is a reversible process. The strength and sign of the spin Hamiltonians can be manipulated by rf pulses and/or sample rotation such that the evolution of the spin system during a period of time is refocused during evolution of the spin system at a latter time. The spin interactions described by inhomogeneous or homogeneous spin Hamiltonians lead to inhomogeneous and homogeneous spin-echoes. If a linear superposition of both types of spin Hamiltonians is present, a mixed spin-echo can be generated. The most common used inhomogeneous echoes are: Hahn [Hah1], stimulated [Hah1], and gradient echoes [Kim1, Cal1]. Solid [Pow1] and magic [Sch4, Rhi1, Dem2] echoes are the most familiar types of homogeneous echoes. Actually for isolated spin pairs ½, the solid echo is not homogeneous refocusing only the dipolar interaction between them. This gives an inhomogeneous broadened line in the ^{1}H spectra.

In order to understand how a spin echo can be produced, we shall consider a spin system composed of *N* nuclei, which may or may not interact between themselves. The quantum-mechanical state of such a system can be described by a linear superposition of spin coherences represented by a vector evolving in a Liouville space of dimension 2^{2N} (c.f. Fig. 2. 3) [Dem1]. In this abstract space, the state of the spin system at time $t = 0$ is represented by a configurational point. This state corresponds in many

cases to the single-quantum coherences excited after a 90° rf pulse. The spin system evolves in the laboratory or rotating reference frames for a time τ, and the evolution is described by the propagator operator $\mathbf{E}_{\text{evolution}} = \exp\{-\mathrm{i}\mathbf{H}_{\text{int}}\tau\}$, where $\mathbf{H}_{\text{int}}$ is the spin-interaction Hamiltonian. At the end of this evolution period, a pulse or a complex pulse sequence is applied which change the sign of the Hamiltonian $\mathbf{H}_{\text{int}}$. During the refocusing period of duration τ the evolution operator is now $\mathbf{E}_{\text{refocusing}} = \exp\{-\mathrm{i}(-\mathbf{H}_{\text{int}})\tau\}$. This is formally equivalent to a time reversal, i.e., $\tau \rightarrow -\tau$. For the full evolution period 2τ, the propagator is $\mathbf{E}_{\text{rvolution}}\mathbf{E}_{\text{refocusing}} = \mathbf{E}$, where $\mathbf{E}$ is the unity operator and the spin system reaches the initial state. Hence, a spin echo is generated with an amplitude identical to that of the free induction decay as long as magnetization relaxation processes are neglected.

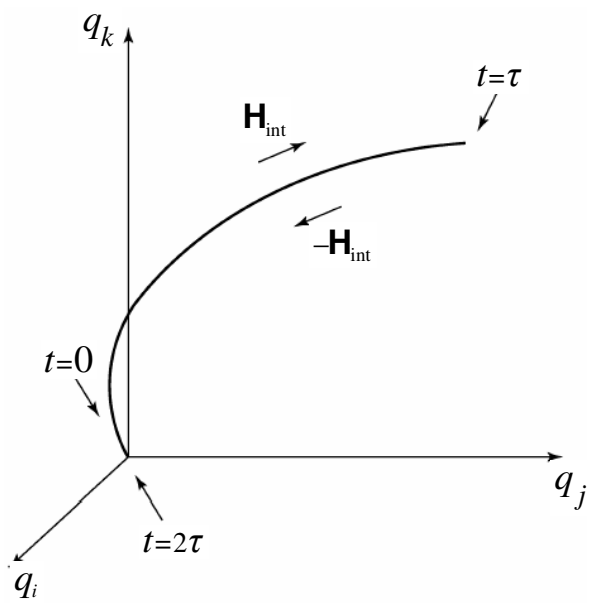

Fig. 2.3 Evolution of the quantum-mechanical state of a spin system in a Liouville space with spin coordinates q_i, q_j and q_k. The evolution from the initial time $t = 0$ to an intermediate time $t = \tau$ takes place under a Hamiltonian $\mathbf{H}_{\text{int}}$ which describes internal and external spin interactions. At this time, a pulse sequence changes the sign of the spin Hamiltonian. The spin system evolves on the same generalized trajectory and after total evolution time $t = 2\tau$ the initial state is refocused under a spin echo [Dem1].

The pulse sequence used for generation of an inhomogeneous spin-echo of the Hahn type is shown in Fig. 2.4a. The spin systems for which this echo can be produced

are characterized by the Hamiltonian $\mathbf{H}_{\text{int}} = -\delta \boldsymbol{I}_z$, where δ describes the inhomogeneity of the magnetic fields or chemical shift distributions. By the action of refocusing $180^{\text{o}}_{\text{y}}$ pulses, the spin operator $\boldsymbol{I}_{\text{z}}$ becomes $-\boldsymbol{I}_{\text{z}}$ and the spin Hamiltonian changes the sign, i.e., $\mathbf{H}_{\text{int}} = -\mathbf{H}_{\text{int}}$. If transverse magnetization relaxation is neglected, the amplitude of the Hahn echo is equal to the amplitude of the free induction decay generated after 90^{o}_{x} preparation pulse (cf Fig. 2.4a). The relaxation encoding is given by the factor $\exp\{-2\tau / T_2\}$, where T_2 is the transverse relaxation time. The Hahn echo represents an important tool for measuring residual dipolar couplings, correlation function of molecular motions, encoding of spatial information, and mass transport. If the $180^{\text{o}}_{\text{x}}$ pulse is split in two 90^{o}_{x} pulses separated by a time τ_2 (c.f. Fig. 2.4b), a stimulated echo is produced at time τ_1 after the action of the last pulse. Under ideal conditions, this spin-echo has an amplitude which is half of that of the FID and the lifetime is much longer than that of the Hahn echo. Therefore, it is an ideal instrument for measuring self-diffusion coefficients.

The scheme used for the gradient echo is presented in Fig. 2.4c. The evolution of the single-quantum coherence excited by a preparation 90^{o}_{x} pulse under a field gradient $\boldsymbol{G}_z$ is refocused by the field gradient with the opposite direction $-\boldsymbol{G}_z$. The amplitude of the echo is affected by the presence of the magnetic field gradients inside the sample. This effect is exploited for enhancement of contrast in Magnetic Resonance Imaging (MRI).

In many rigid or soft polymers, the protons are dipolar coupled in a complex network. Considering only two coupled spins the interaction is inhomogeneous. However, in the case of the multi-spin coupling, the dipolar Hamiltonian is bilinear in the spin operators revealing a homogenous interaction. Pulse sequences can be designed that change the sign of the dipolar Hamiltonian $\mathbf{H}_{\text{d}}$, i.e., $\mathbf{H}_{\text{d}} \rightarrow -k\mathbf{H}_{\text{d}}$, where k is a scaling factor. An example of a homogeneous spin-echo in a coupled multi-spin system is given by the magic echo for which $k = 1/2$ (c.f. Fig. 2.5 b). The most simple homogeneous spin echo is represented by the solid echo (Fig. 2.5a).

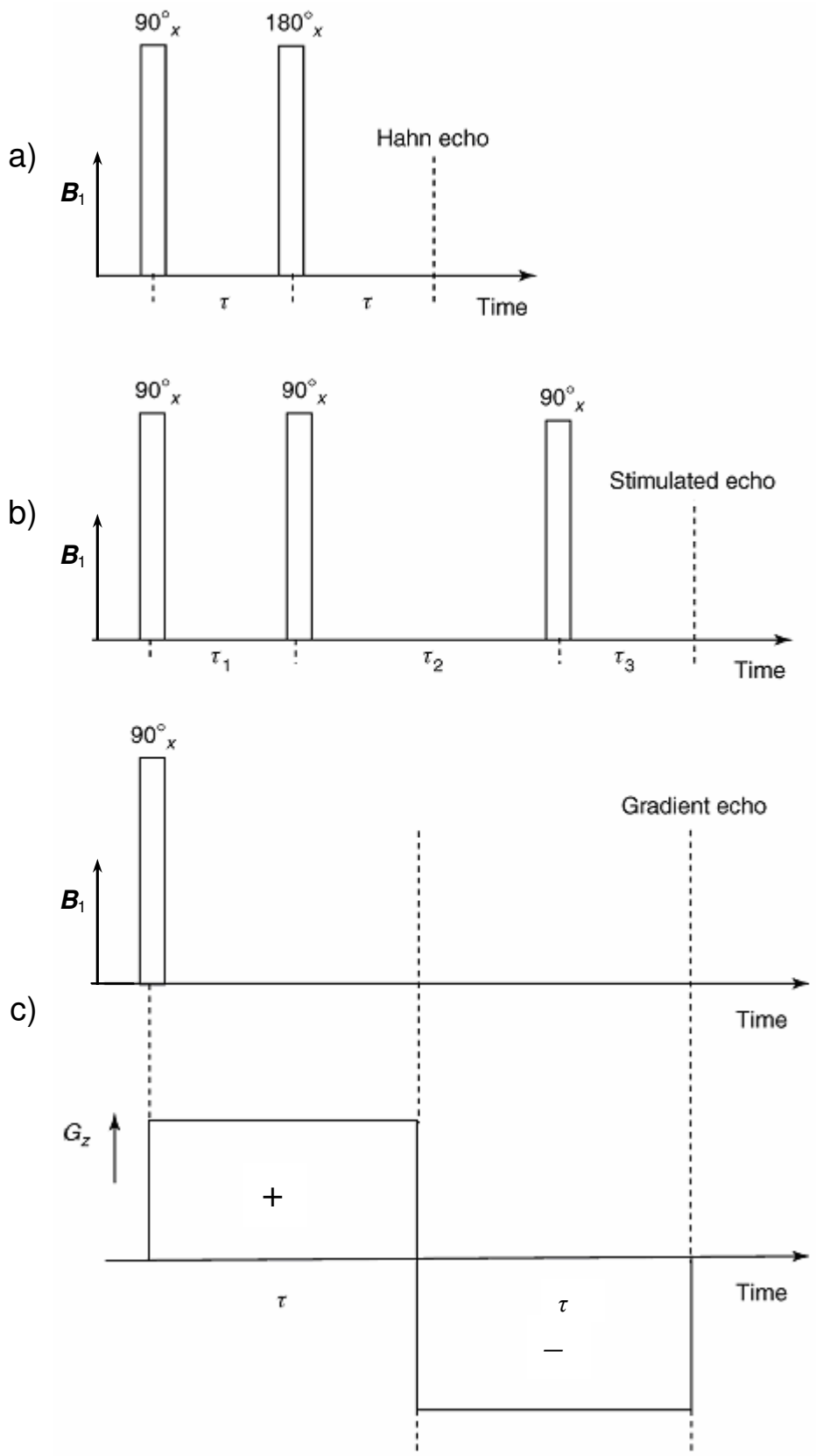

Fig. 2.4. Pulse sequences used for the Hahn echo a), the stimulated echo b), and the gradient echo c).

For a spin system composed of spin $-1/2$ pairs the spin evolution is fully refocused by the solid echo. This is not the case for a multispin dipolar network. These echoes can be used for high resolution NMR spectroscopy of solids, measurement of residual dipolar correlation function, and NMR imaging of rigid polymers.

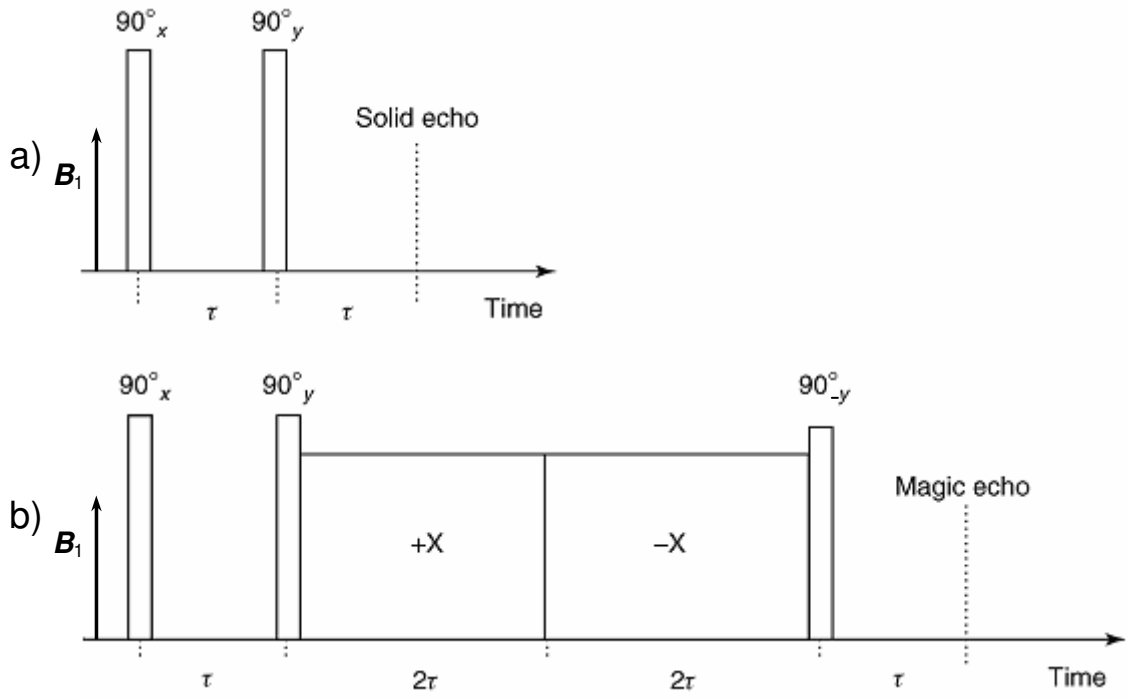

Fig. 2.5 Pulse sequences for the solid echo a) and the magic echo b).

2.2 NMR imaging

NMR imaging is a noninvasive analytical technique used to produce images of arbitrarily oriented slices through optically nontransparent objects. Biological tissues, plants and many synthetic materials can be penetrated by radio-frequency waves without significant attenuation of the signal by absorption or emission. In this sense, objects which are nontransparent to electromagnetic waves at optical frequencies appear transparent to radio waves.

2.2.1 Principles of NMR imaging

In polymers as well as in biological materials, the spatial distribution of the nuclei and the spin interactions as well as motions can be probed by NMR at different length scales using different strategies. The NMR techniques suitable for investigation of spatial structures are identified in Fig. 2.6 together with the appropriate spatial resolution scale [Dem1]. In the nanoscale range, spectroscopic methods based on manipulation of spin interactions can measure internuclear distances and bond angles ([Lev1], and references therein). The field gradients are used for selection of the coherence pathways and encoding of molecular diffusion but many methods perform without the demand for field gradients. In the mesoscopic range, spin diffusion ([Sch2], and references therein) can be used for measuring domain sizes and morphology. The domain of NMR imaging of polymers [Blü6, Blü7, Dem3, Dem4, Cor1], which uses space encoding by field gradients can probe today only macroscopically distributed heterogeneities, i.e., in the order of 10–100 μm.

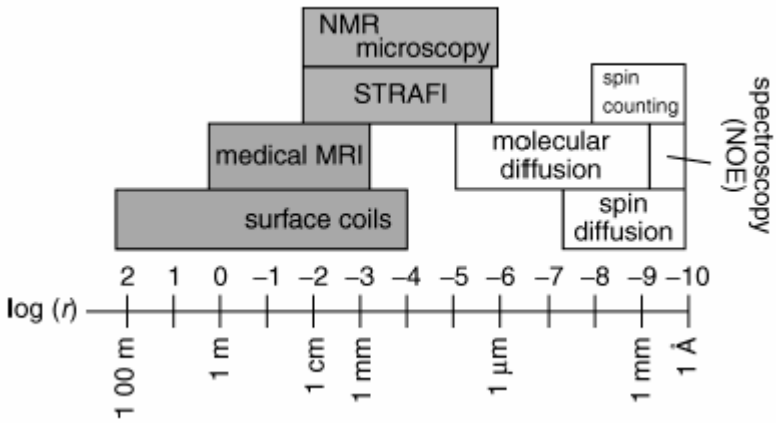

Fig. 2.6 Range of spatial resolution available from different NMR experiments that covers over ten orders of magnitude. The methods using direct space encoding by gradients are shaded, but all other spatial information can be included for creation of image contrast (Reproduced from ref. [Dem1]).

In the last years, the field of spatially resolved magnetic resonance which includes imaging [Blü1], microscopy, and volume localized spectroscopy of materials [Kim1, Cal1] has been advanced by the introduction of several new techniques and improvement of the existing ones designed to overcome, mainly, the dipolar interactions of abundant proton spins in rigid polymers that contribute to broadening of the NMR

resonance lines. The well-known condition $\Delta x = 2\pi\Delta\upsilon_{1/2}/(\gamma G_x)$ (see for instance, Ref. [Man2]) for the spatial resolution Δx^{-1} by frequency encoding, where γ is the magnetogyric ratio, $\Delta\upsilon_{1/2}$ is the full width at half height of NMR spectrum, and G_x is the field gradient strength in the *x*-direction, can define the strategies for improving the quality of NMR images. There are, in principle, two possibilities: either the gradient strength can be increased or the line width is reduced [Man2, Blü8, Str1, McD1]. This can be achieved by manipulation of the spin or the space part of the interaction Hamiltonian or both, or by dilution manipulations [Meh1]. Increasing the gradient, strength might seem the simpler approach. However, the difficulty of using a large gradient is that the receiver bandwidth must be increased to accommodate the spread in resonance frequencies and therefore more noise is introduced into the resultant image. The noise content is proportional to the square root of the receiver bandwidth, and hence the time to acquire a given quality image, in both resolution and sensitivity, depends on the line width. Many solid state imaging techniques use spin coherences refocused by echoes for different purposes: (*1*) to record very short free induction decays present, in general, for solids and/or in the presence of strong field gradients; (*2*) for space encoding during the echo time; (*3*) for line narrowing by homonuclear or heteronuclear dipolar decoupling; (*4*) for reconversion of multiple-quantum (MQ) coherences into detectable single-quantum coherences. The properties of the spin echoes that refocus inhomogeneous and homogeneopus spin interactions have been discussed in the previous section. Also so called time-suspension echoes can be produced which eliminate all internal and external spin interactions. In the maximum of such an echo, each individual spin is fully isolated in the rotating reference frame in the absence of relaxation processes; the time appears to be suspended.

Methods of liquid-state imaging which can be applied, for instance, for analysis of elastomers or polymer swelling have been reviewed on several occasions (see for instance, Refs. [Blü1, Blü7, Man2, Blü8, Str1, McD1]. Many of the methods used to record NMR images of solids can be combined with spectroscopic information. This unique feature and the richness in parameter contrast compensate for the relatively modest spatial resolution in many applications. If the spatial information is phase encoded, ie, indirectly detected, then the spectroscopic dimension is scanned directly, in many cases, by means of spin-echoes and in the absence of gradients. This approach is

referred to as frequency encoding. On the other hand, the spectroscopic information can be phase encoded or detected indirectly in the same way as in conventional two-dimensional spectroscopy. This approach is referred to as phase encoding.

2.2.2 Spin system response in heterogeneous samples

In the following, a heterogeneous sample having magnetically equivalent nuclei with magnetogyric ratio γ and local spin density $\rho(\boldsymbol{r})$ is considered. The space localized thermodynamic equilibrium magnetization corresponding to a voxel with coordinates (x, y, z) of the position vector $\boldsymbol{r}$ is given by $m_0\ (x,\ y,\ z) = C\rho(x,\ y,\ z)$, where C is the Curie constant. In the rotating reference frame at the resonance frequency, the single-pulse NMR spin system response $s(\boldsymbol{r},t)$ can be expressed by the local free induction decay (FID) $f(\boldsymbol{r},t)$ [Dem1],

$$s(\boldsymbol{r},t) = C\rho(\mathrm{r})f(\boldsymbol{r},t). \tag{2.27}$$

Spatially resolved NMR is concerned with unravelling the spatial distribution of $\rho(x,\ y,\ z)$ and measuring associated NMR parameters at individual "volume cells", or voxels at space point specified by the vector $\boldsymbol{r}$. If many contiguous voxels are investigated on a plane, or if a projection is investigated, one refers to NMR imaging, if individual voxels are investigated one refers to volume-selective NMR.

The spin density distribution can be resolved by different techniques. The standard approach exploits the possibility of introducing space dependence to the resonance frequency ω in each voxel by superposing a magnetic field gradient to a homogeneous magnetic field $\boldsymbol{B}_0(0,0,B_0)$ by the use of additional coils. In general, the field gradient is a cartesian tensor with nine components related by the Maxwell equations. In the limit of large static magnetic field and small gradient, the gradient tensor can be reduced to a gradient vector $\boldsymbol{G}$ for an approximate description of the imaging experiments with good accuracy. Then the resonance frequency becomes dependent on the space vector $\boldsymbol{r}$, i.e., $\omega(\boldsymbol{r}) = \gamma(\boldsymbol{B}_0 + \boldsymbol{G}\cdot\boldsymbol{r}) = \omega_0 + \gamma\boldsymbol{G}\cdot\boldsymbol{r}$, where the field gradient vector collects the derivatives of the magnetic field in the z-direction with respect to the space coordinates defined by the component of the field gradient:

$\boldsymbol{G}(\partial \boldsymbol{B}_0/\partial x, \partial \boldsymbol{B}_0/\partial y, \partial \boldsymbol{B}_0/\partial z)$. The total time-dependent signal of an inhomogeneous object of volume $\boldsymbol{V}$ measured in a magnetic field gradient and in the rotating frame at the angular frequency ω_0 is given by [Dem1]

$$\boldsymbol{S}(t) \propto \boldsymbol{C} \iiint_V \rho(x,y,z) f(x,y,z,t) \exp\{\mathrm{i}\gamma \boldsymbol{G} \cdot \boldsymbol{r}t\} \,\mathrm{d}x\,\mathrm{d}y\,\mathrm{d}z. \tag{2.28}$$

In high magnetic field the spatial dependence of the Curie constant can be neglected in a good approximation. In order to illustrate the basic concepts of space encoding time-dependent gradients $\boldsymbol{G}(t)$ shall be admitted. The wave vector $\boldsymbol{k}$ can be introduced which is the Fourier conjugate to the space variable $\boldsymbol{r}$,

$$\boldsymbol{k}(\mathrm{t}) = \gamma \int_0^t \boldsymbol{G}(t)\mathrm{d}t. \tag{2.29}$$

In this notation, the single-pulse response signal in time-dependent main field gradients becomes

$$\boldsymbol{S}(t) \propto \boldsymbol{C} \iiint_V \rho(x,y,z) f(x,y,z,t) \exp\{\mathrm{i}\boldsymbol{k}(t) \cdot \boldsymbol{r}\} \,\mathrm{d}x\,\mathrm{d}y\,\mathrm{d}z. \tag{2.30}$$

This equation is the starting point for the discussion of the basic procedures for spatial resolved NMR.

2.2.3 Frequency encoding

The principle of the spatial resolution of NMR imaging by frequency encoding is discussed in the following in the presence of a pulsed uniform gradient, say $\boldsymbol{G}_x = \partial \boldsymbol{B}_0/\partial x$. After the radiofrequency excitation pulse the quantity $k_x(t)$ grows linearly with time according to Eq. 2.29, i..e., $k_x(t) = \gamma \mathrm{G}_x t$. Thus, k space is sampled in the direction of k_x, and time t and k_x are equivalent variables. If t is replaced by $k_x/(\gamma \boldsymbol{G}_x)$ the spin system response given by Eq. 2.30 becomes [Dem1]

$$\boldsymbol{S}(k_x/(\gamma \boldsymbol{G}_x)) \propto \boldsymbol{C} \iiint_V \rho(x,y,z) f(x,y,z,k_x/(\gamma \boldsymbol{G}_x)) \exp\{\mathrm{i}\gamma \boldsymbol{k}_x \cdot x\} \,\mathrm{d}x\,\mathrm{d}y\,\mathrm{d}z. \tag{2.31}$$

The complex FID signal acquired in this way is composed of contributions evolving according to the local offset resonance frequency $\gamma \boldsymbol{G}_x x$ labelling the nuclei responsible

for this local transverse magnetization, hence, the term frequency encoding. Note that this is the conventional way of encoding in Fourier transform spectroscopy. However, in the context of NMR imaging, signals are processed in terms of the wave numbers k_x rather than of offset frequencies. The Fourier transform over k_x produces the convolution of the Fourier transform of the functions $\rho(x, y, z)$ and $f(x, y, z, k_x/(\gamma \boldsymbol{G}_x))$. If $f(x, y, z, k_x/(\gamma \boldsymbol{G}_x)) \approx f(k_x/(\gamma \boldsymbol{G}_x))$, the Fourier transform of the FID is the space-dependent spectral response $\boldsymbol{F}(x)$ and the Fourier transform of the triple integral is a projection $\boldsymbol{P}(x) = \iint \rho(x, y, z)\, \mathrm{d}y\, \mathrm{d}z$ of the spin density on the x-axis. Then, the Fourier transform of equation 2.31, can be written as

$$\boldsymbol{S}(x) \propto \boldsymbol{C} \int_{x_{sample}} \boldsymbol{F}(x - x')\boldsymbol{P}(x')\mathrm{d}x', \tag{2.32}$$

where x_{sample} represents the sample size in the x-direction. A faithful representation of the spin-density projection $\boldsymbol{P}(x)$ would be obtained by this method of frequency encoding only if the spectrum $\boldsymbol{F}(x - x')$ is a Dirac function $\delta(x - x')$, or a narrow NMR absorption line like for liquid samples.

The above discussion is illustrated in Fig. 2.7. If the samples are liquid, a narrow NMR absorption line is observed for both samples in a homogeneous magnetic field and a projection of the object along the x-axis is measured in the presence of the field gradient $\boldsymbol{G}_x$.

The signal amplitude at each resonance frequency or space coordinate is determined by the number of spins which experience the same magnetic field strength. If the spectrum in a homogeneous field is broad like in the solid samples (bottom traces) then the convolution (c.f. Eq. 2.32) of the projection of the spin density by the line shape becomes noticeable, and the spatial features are smeared out. Thus, the minimum distance Δx which can be resolved is defined by the ratio of the full width at half spectral intensity $\Delta\omega_{1/2}$ of spectral features to the spread of the resonances introduced by the field gradient, ie,

$$\Delta x = \frac{\Delta\omega_{1/2}}{\gamma \boldsymbol{G}_x}. \tag{2.33}$$

Clearly, Eq. 2.33 indicates that when the line width increases, the gradient strength $\boldsymbol{G}_x$ also has to be increased, at least when the resolution Δx^{-1} is to be kept constant.

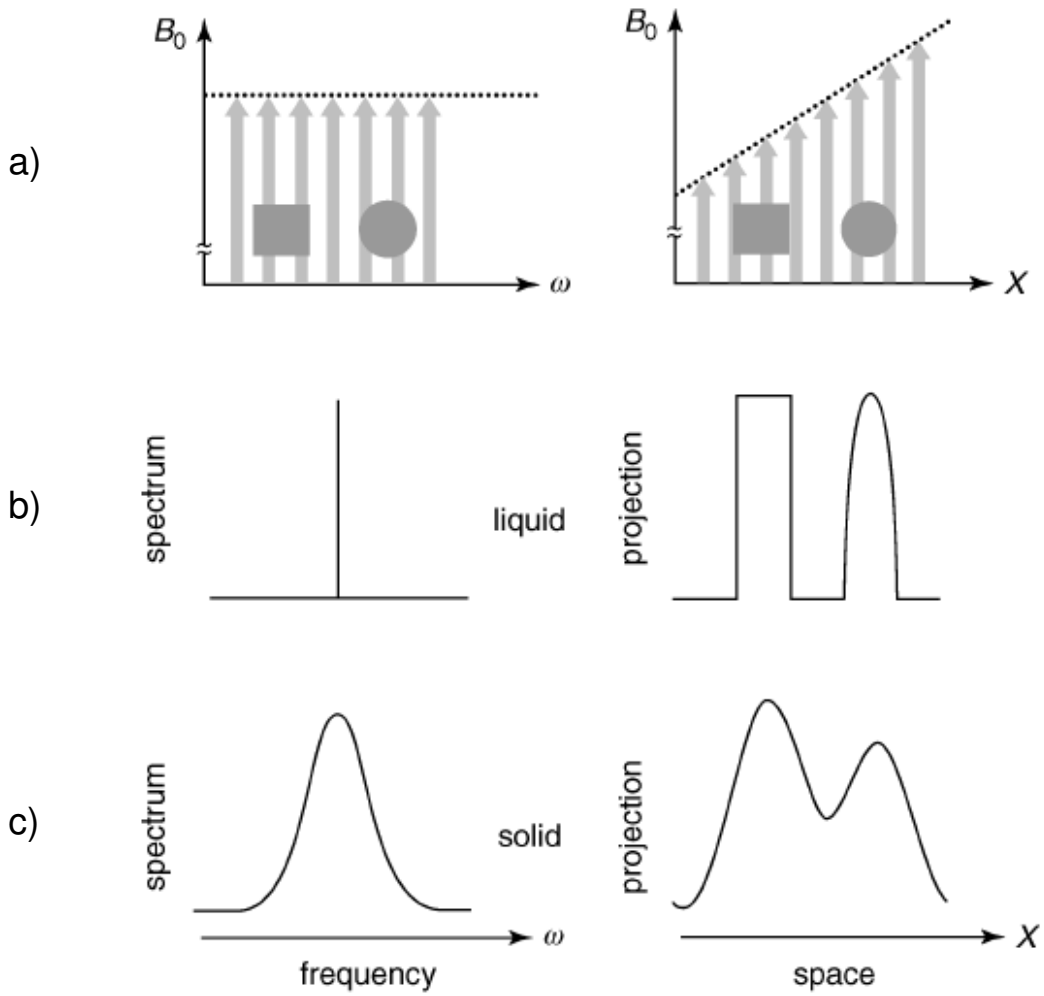

Fig. 2.7 Effect of the field gradient on the NMR signal. The sample consists of a rectangular and a circular object. a) Homogeneous magnetic field (left) and magnetic field with a linear space dependence (right). b) Spectroscopic response for a liquid sample with a single, narrow line in the NMR spectrum. c) Spectroscopic response for a solid sample with a single, broad line in the NMR spectrum [Dem1].

2.2.4 Phase encoding

Broadening of the projection by the NMR spectrum (c.f. Eq. 2.32) can be avoided if the spatial information is detected indirectly in the fashion of the multidimensional Fourier NMR spectroscopy [Ern2]. For instance, a magnetic-field gradient $\boldsymbol{G}_y$ is switched on for an evolution time t_1 following a radio-frequency excitation pulse, and the signal is acquired in a detection time t_2 after the gradient has been switched off. For this 2D scheme, the NMR signal can be written as

$$\boldsymbol{S}(t_1,t_2) \propto \boldsymbol{C} f(t_1) f(t_2) \int_{y_{sample}} \boldsymbol{P}(y) \exp\{\mathrm{i}\gamma k_y y\} \mathrm{d}y, \tag{2.34}$$

where $k_y = \gamma G_y t_1$ and $\boldsymbol{P}(y) = \iint \rho(x, y, z)\, \mathrm{d}x\, \mathrm{d}z$. It becomes clear that there are two ways to perform the experiment: either t_1 is varied in the custom of 2D NMR spectroscopy, or t_1 is kept constant and $\boldsymbol{G}_y$ is stepped in increments $\Delta \boldsymbol{G}_y$. The first case bears no advantage compared to direct frequency encoding discussed above. As time t_1 proceeds, not only does k_y increase, but also the free induction decay $f(t_1)$ evolves and deteriorates the signal intensity and finally the spatial resolution. But, if t_1 is kept constant $f(t_1)$ has a fixed value, and the phase change of the signal in the evolution period depends only on the wave vector $\boldsymbol{k}_y$. Thus, the spatial resolution achievable for phase encoding depends on the maximum gradient strength available and on the signal-to-noise ratio, because the signal strength decreases with increasing $\boldsymbol{k}$.

The digital resolution or the pixel resolution of an NMR image can be much higher than the actual space resolution. The digital resolution $1/\Delta y$ of the NMR imaging in y-direction is determined by the maximum value of $\boldsymbol{k}_y$ or equivalently by the number n_y of complex signal values and the $\boldsymbol{k}$ space sampling intervals Δk_y, i.e., $1/\Delta y = n_y \Delta k_y / (2\pi)$. To avoid signal aliasing, $\boldsymbol{k}_y$ has to be stepped in small enough intervals so that the signal-phase increment $y_{\max} \Delta k_y$ for the maximum object coordinate $y_{\max}$ never exceeds 2π.

2.2.5 Sampling *k* space

Different imaging schemes are often discriminated against the way $\boldsymbol{k}$ space is sampled (for more details see Ref. [Blü1]). Two elementary 2D NMR imaging methods are illustrated in Fig. 2.8: back-projection imaging (BPI, Fig. 2.8a) and 2D Fourier imaging (2DFI, Fig. 2.8b) [Dem1]. Orthogonal gradients are switched subsequently in 2DFI and simultaneously in BPI. As a consequence, $\boldsymbol{k}$ space is sampled in orthogonal coordinates for 2DFI.

When applied simultaneously, the direction of the resulting gradient changes depending on the relative strengths of $\boldsymbol{G}_x$ and $\boldsymbol{G}_y$ gradients. In this way, $\boldsymbol{k}$ space can be

sampled in cylindrical coordinates in BPI. In either case, the image is obtained by the Fourier transformation of the ***k***-space data. Often phase and frequency encoding are combined for acquisition of 2D images (c.f. Fig. 2.8b, left). The gradient $\boldsymbol{G}_y$ is called the phase encoding gradient, while $\boldsymbol{G}_x$ is the frequency encoding gradient. This is one of the most used methods for recording images in elastomeric materials which are soft solids with NMR line widths in the range $\Delta\nu_{1/2} \approx 100\text{Hz}/1\text{kHz}$.

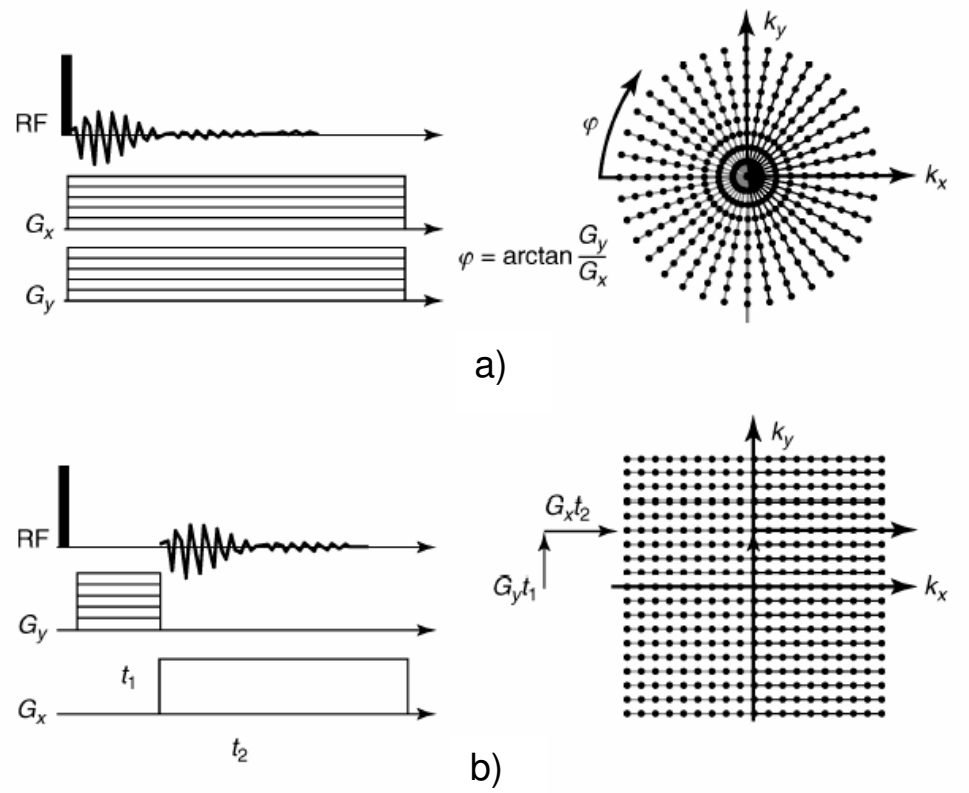

Fig. 2.8 Schemes for acquisition of 2D NMR images. Excitation and detection schemes (left) and maps in ***k*** space, where the NMR signal are acquired (right) [Dem1].

2.2.6 Contrast in NMR imaging

NMR imaging is characterized by a plenty of parameters which can be exploited for producing contrast [Blü9, Blü10]. Many features invisible to other image forming techniques can be visualized with NMR. To exploit the diversity of contrast features, it is useful to optimize the imaging experiment for generation of maximum contrast. The

local contrast C is defined as the relative difference in image intensities M of neighbouring structures i and j [Man2]

$$\mathrm{C} = \frac{\left|\boldsymbol{M}(\boldsymbol{r}_i) - \boldsymbol{M}(\boldsymbol{r}_j)\right|}{\left|\boldsymbol{M}_{\max}\right|} \tag{2.35}$$

where $\left|\boldsymbol{M}_{\max}\right|$ is the absolute maximum of $\boldsymbol{M}(\boldsymbol{r}_i)$ and $\boldsymbol{M}(\boldsymbol{r}_j)$, where $\boldsymbol{r}_i$ and $\boldsymbol{r}_j$ are the space coordinates of the voxels i and j under consideration.

Contrast parameters

The contrast parameters relevant for polymer characterization by NMR imaging are directly related to the spin density, static and fluctuating nuclear spin interactions, and to the mass transport parameters. Even if the above quantities can change on molecular or mesoscopic scale only the variation of them on the space domains larger than the image resolution can be detected in NMR imaging. The residual dipolar and quadrupolar interactions are related to the NMR parameters like van Vleck moments [Meh1] and relaxation times [Abr1]. The fluctuating part of spin interactions leads to a variety of contrast parameters of magnetization relaxation type like spin-lattice relaxation in the laboratory reference frame (T_1), rotating frame ($T_{1\rho}$), transverse relaxation (T_2), solid echo or coherent averaging pulse sequence decay time ($T_{2\mathrm{eff}}$) [Meh1], and dipolar correlation decays [Kim1]. The relaxation NMR parameters are also related to the manipulation of sample by contrast agents like paramagnetic relaxation agents, ferromagnetic particles [Man2], and hyperpolarized xenon [Raf1, Dem5]. The chemical shielding interaction leads to chemical contrast parameters related to the chemical composition as well as molecular orientation. Differences in magnetic susceptibility and the distribution of magnetic fields produced by electrical currents can be also detected via chemical shift [Blü1]. The NMR quantities defining the contrast of NMR images depend on various macroscopic and microscopic physical and chemical parameters of the investigated samples which affect the nuclear spin interactions or molecular transport parameters. They can be classified as internal and external. Moreover, they can be state parameters that are stationary quantities like stress, strain, moduli of shear and compression, cross-link density, distribution and agglomeration of filler particles, molecular orientation, fibril orientation and domain size distribution, distribution of

voids, and the temperature distribution. Transition parameters or kinetic parameters characterize the time evolution of the polymer system. They are determined in *in situ* NMR experiments or in stop-and-go experiments. Examples are characteristic times of chemical and physical aging [Fül1, Blü11] of vulcanization [Fül2] and curing [Arm1] processes of heat dissipation and fluid permeation [Man3, Ran1].

Transition parameters can be determined directly from the analysis of the time evolution of changes in NMR images, but state parameters must be related to NMR parameters either by theory or calibration. Theories that relate the cross-link density of unfilled and filled elastomers to the parameters of transverse relaxation parameters [Sim1] and others relating dynamic storage modulus of polymers to the cross-polarization rate [Par1] have already been published.

A simple approach is based on empirical correlations between NMR parameters and sample properties, which often can be established by calibration of an NMR parameter against a material parameter [Blü12, Sch5]. By use of the stress–strain curve from mechanical measurements, T_2 can be calibrated against stress. The procedure can be used to translate the spatially resolved NMR parameters T_2 into values related to the strength of local stress.

Magnetization filters

The contrast generation in NMR imaging is directly related to the concept of magnetization or coherences filters. Various molecular (internal) or external parameter weights are introduced by the use of magnetization or coherences filters (Fig. 2.9) [Dem1], which block part of the incoming signal originating from the thermodynamic equilibrium magnetization. As a result, there is a gain in selectivity of the output signal at the expense of a deterioration of signal-to-noise ratio. A generic scheme for contrast optimisation in the Fourier NMR imaging is illustrated in Figure 2.9 b), [Blü9].

In general, three periods are distinguished: a filter period, a space-encoding period, and a spectroscopy period. For image contrast other than the often-uninformative spin density, the space-encoding period must be combined either with a magnetization filter or with spectroscopic data acquisition or both. The signal detected after the action of the general pulse sequence designed to introduce image contrast can be written as [Xia1]

$$\boldsymbol{S}(\boldsymbol{k}) = \int \rho(\boldsymbol{r})\boldsymbol{F}_c(\{p\},\boldsymbol{r})\exp[-\mathrm{i}2\pi\boldsymbol{k}\cdot\boldsymbol{r}]d\boldsymbol{r}. \tag{2.36}$$

where the contrast parameter manifold is denoted by $\{p\}$ and $\boldsymbol{F}_c(\{p\},\boldsymbol{r})$ is the combined local contrast function. This function could be a product of several parameter contrast functions, such as

$$\boldsymbol{F}_c(\{p\},\boldsymbol{r}) \equiv \boldsymbol{F}_c(T_1,\boldsymbol{r})\boldsymbol{F}_c(T_{1\rho},\boldsymbol{r})\boldsymbol{F}_c(T_2,\boldsymbol{r})\boldsymbol{F}_c(\delta_i,\boldsymbol{r})\boldsymbol{F}_c(q,\boldsymbol{r})..., \tag{2.37}$$

where for instance, the contrast factors in the right-hand side of equation 2.37 representing the effects of longitudinal (T_1 and $T_{1\rho}$) and transverse (T_2) relaxation times, chemical shift (δ), and the effect of coherent and incoherent molecular translation motions described in the $\boldsymbol{q}$ space [Cal1].

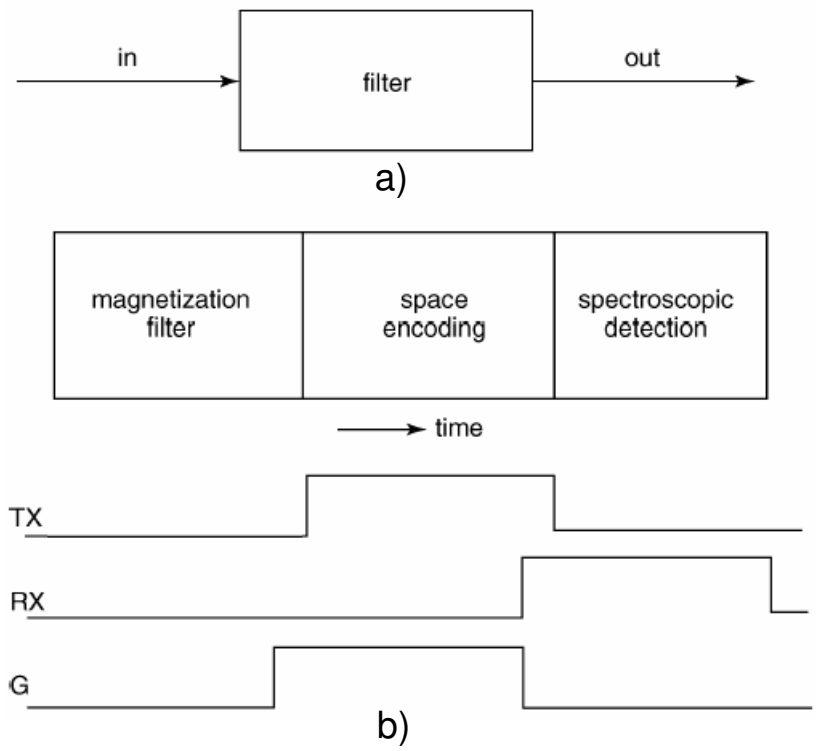

Fig. 2.9 a) A magnetization filter blocks part of the incoming magnetization or spin coherences. b) General scheme for generation of NMR image contrast. Initial nuclear magnetization is filtered by the radio-frequency irradiation (TX) of resonant nuclei before or also during the space encoding period by magnetic-field gradients (***G***). In the absence of gradients, the NMR signal is detected (RX) for the extraction of spectroscopic information [Dem1].

Chapter 3

Single-Sided NMR

In the past decade, many NMR applications that operate in low and strongly inhomogeneous static and radio-frequency magnetic fields have been developed as consequence of the development of NMR surface sensors. A large number of dedicated NMR surface scanners has been built and ever improved for non-destructive investigation of arbitrarily large objects. The strength of this branch of NMR in domains like material science, medicine, oil industry, quality control, etc. has abundantly been proved. An introduction to low-field NMR with a general presentation of single-sided NMR sensors will be the topic of this chapter.

3.1 Introduction

Nuclear Magnetic Resonance (NMR) is a powerful established analytical tool that is widely used for structural and conformational analysis in chemistry, biology, medicine, and materials science [Cal1, Blü1]. Material characterization is mainly carried out by measuring NMR parameters like the chemical shift, the nuclear spin relaxation times, the dipolar coupling, and the self-diffusion coefficient. Furthermore, images can be produced by NMR techniques in which the contrast is determined by these parameters, and NMR is employed to characterize diffusive and coherent molecular motion in a non-invasive fashion.

NMR methods have been initially developed to work in homogeneous fields of strong magnets, but the limited accessible sample volume of these devices restricts the application of NMR in particular for *in situ* studies of large objects. But in addition to conventional NMR, where the sample is adapted to fit into the probe, there is inside-out NMR [Bro3, Bro4, Woe1], which uses open magnet geometries specially adapted to the object under study.

The inside-out concept was born more than half a century ago in the oil industry, where the entire spectrometer is lowered into the well to characterize the underground formation [Kle1, Kle2, Jac1, Mat1]. Later, exploiting the generation of both static and radio-frequency fields external to the sensor, hand-held devices, like the NMR-MOUSE, were developed [Eid1]. These low cost, portable sensors provide excellent versatility and open up new applications for NMR inaccessible to closed magnet geometries.

3.2 Inhomogeneous magnetic fields

The quest for high fields is rationalized by the fact that both, the nuclear magnetization and the frequency range of the chemical shift are proportional to the strength of the polarizing field. However, low and inhomogeneous fields turned out to provide many challenges already at the beginnings of NMR. Consequently, NMR in inhomogeneous fields has extensively been explored in the past decades. The main price unilateral sensors had to pay for having access to large objects was sensitivity. Alongside, the strong magnetic field gradients have been regarded for a long time as another problem, leaving as only alternatives for low-field NMR, the measurements of signal amplitudes, relaxation times T_1 and T_2, and self-diffusion coefficients.

Nowadays, imaging and even high resolution spectroscopy is possible. Here specific echo techniques are implemented, to overcome the effects of field inhomogeneity. From this point of view, NMR in inhomogeneous fields became in many cases NMR in linear fields, a well suitable technique for high resolution NMR profiling [Per1] and 1D imaging [Cas2, Cas3, Per2].

Using rf pulses and the natural gradient of permanent magnets, selective excitation is achieved. Considering the linear field region of the single-sided sensor, the

excitation bandwidth covers a volume with well-defined shape and dimension in space. Here comes the importance of knowing the polarization field profile inside the sample as well as the influence of the sample dimensions on the field profile.

When the sample is small compared to the magnet, the field across the sample can be made high and homogeneous. For samples large compared to the magnet, the field can at best be homogeneous in a small region of the sample, but not across the whole sample. As a rule for single-sided NMR devices, the more homogeneous the field across the sample, the lower is the field strength. Considering as example a 1 μs rf pulse, the maximum excitation bandwidth is about 500 kHz, and the excitation is selective for single-sided NMR devices and large objects.

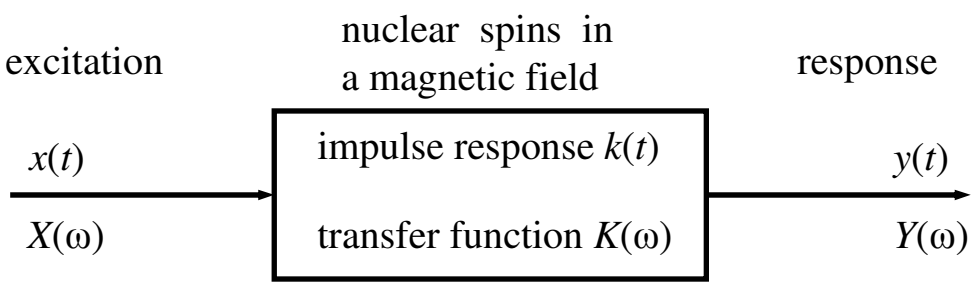

Fig. 3.1 NMR excitation and response in the linear approximation.

Considering the nuclear spins in a magnetic field, they form a system which transforms the rf excitation $x(t)$ into the response or transverse magnetization $y(t)$ (Fig. 3.1). The system is characterized by the impulse response function $k(t)$ which corresponds to the free induction decay. When approximated by a linear system, the NMR response spectrum $Y(\omega)$ is given by the product of the excitation spectrum $X(\omega)$ with the transfer function $K(\omega)$,

$$Y(\omega) = K(\omega)\, X(\omega) \tag{3.1}$$

The transfer function is the Fourier transform of the impulse response function $k(t)$. For pulsed excitation in homogeneous fields, the transfer function is narrow compared to the excitation spectrum of the rf impulse [Blü1]. The response spectrum is then the transfer function (the 1D NMR spectrum). For large objects in inhomogeneous fields, the excitation spectrum is narrow compared to the transfer function, so that the response spectrum is the excitation spectrum. This is the Fourier transform of the

impulse used for excitation.The size and shape of the sensitive volume can be tailored by the profiles of the polarization field $\boldsymbol{B}_0(\boldsymbol{r})$ and the rf field $\boldsymbol{B}_1(\boldsymbol{r})$, and by the choice of rf excitation.

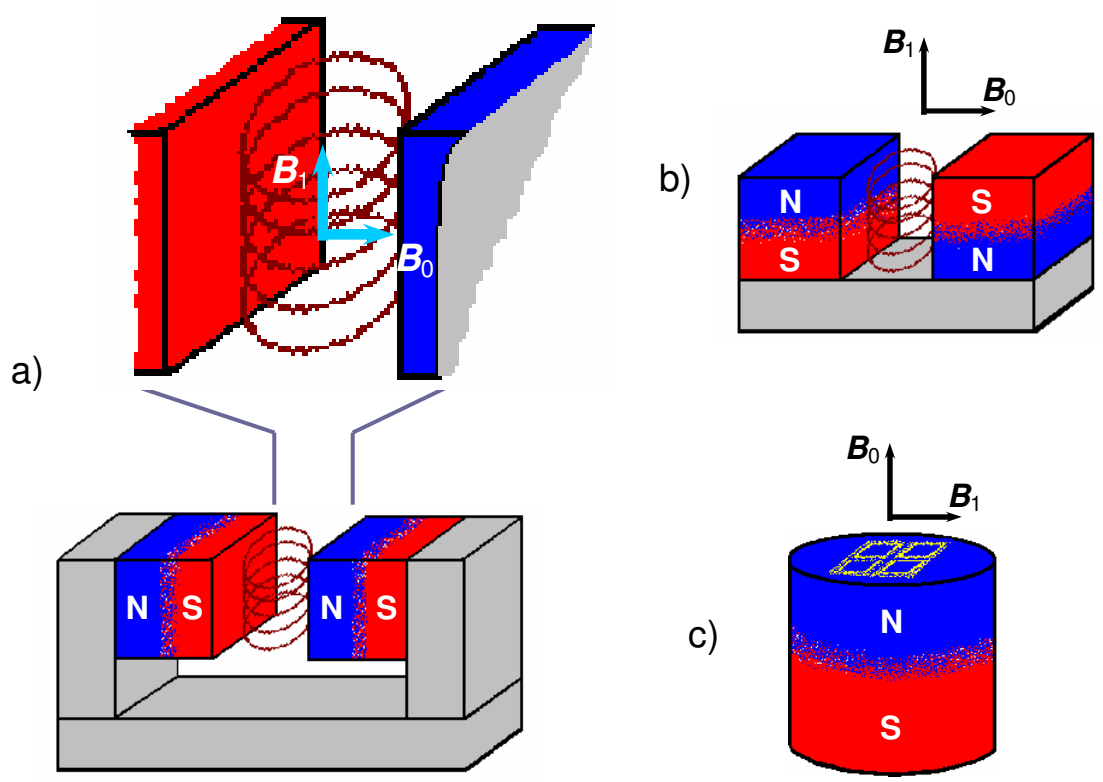

Fig. 3.2 Simple geometries of permanent magnets and rf coils used for NMR. a) Conventional c-shaped geometry where the sample is positioned in the homogeneous field inside the gap and inside the rf coil. b) U-shaped open magnet. The sample is positioned above the gap in the stray fields of the magnet and the rf coil. The magnetic polarization field is parallel to the sensor surface. c) Simple bar magnet with a butterfly coil on one of the faces. The magnetic polarization field is perpendicular to the sensor surface.

3.3 Unilateral sensors – the NMR-MOUSE

The classical geometry for a single-sided sensor employs a magnet in the shape of a “U” or a horseshoe (Fig. 3.2b) [Mat1, Mar2, Eid1, Blü13, Anf1]. This shape is obtained by opening up a conventional c-shaped magnet with a homogeneous field between its poles (Fig. 3.2a) [Pur1, Blo1]. While in conventional NMR devices (Fig. 3.2a), the sample

rests inside the rf coil and between the magnet poles to achieve maximum strength and homogeneity, in unilateral NMR the sample rests near the sensor in the inhomogeneous stray fields of the magnet and the rf coil. This lifts the constraints on the sample size, but introduces variations in magnitude and orientation of the polarization and rf fields $\boldsymbol{B}_0$ and $\boldsymbol{B}_1$, respectively, across a large sample.

Once accepting inhomogeneous fields for the NMR measurement, the most simple NMR sensor is obtained as the simple bar magnet (Fig. 3.2c) [Blü3, Blü14]. If the rf coil is placed on one of the faces, the orientation of the $\boldsymbol{B}_0$ field is perpendicular to the sensor surface, and an rf coil which produces a field parallel to the surface needs to be employed. The different orientations of $\boldsymbol{B}_0$ parallel and perpendicular to the sensor surface are important in the analysis of molecular order, i.e., in materials with non-isotropic segmental orientation due to morphology or external actions like pressure, stress, etc. [Hai1, Hai2].

3.3.1 Field profiles

The NMR-MOUSE is characterized by polarizing magnetic fields with strengths up to 0.5 T and gradients in the range of 2.5 - 22.5 T/m close to the surface of the sensor. In this way, the sensitive volume is restricted to regions near the surface of the object under examination. Most of the applications use u-shaped configurations due to some advantages of this type of geometry in comparison with the bar magnet geometry like: the compact definition the sensitive volume with the large dimensions in a plane parallel to the sensors surface, the “more homogeneous” polarizing field (reduced gradient of the $\boldsymbol{B}_0$ field along the perpendicular direction) as well as the higher efficiency of the surface coils that fit this kind of geometry. One should not neglect the effect of the iron yoke apparently used as holder for the magnets in the case of the u-shaped magnet, but with some other important advantages like the significant increase of the $\boldsymbol{B}_0$ field, and the reduction to almost zero of the stray field at the bottom side of the sensor. The basic u-shaped magnet geometry (Fig. 3.3 a) produces a field, with approximately quadratic profiles along x and z [Mat1, Mar2, Eid1, Bal1, Blü13, Hog1, Har1] (Fig. 3.3 b). With increasing distance y from the magnet surface, the curvature changes from concave to convex along the z-direction while it maintains a convex shape along the x-direction.

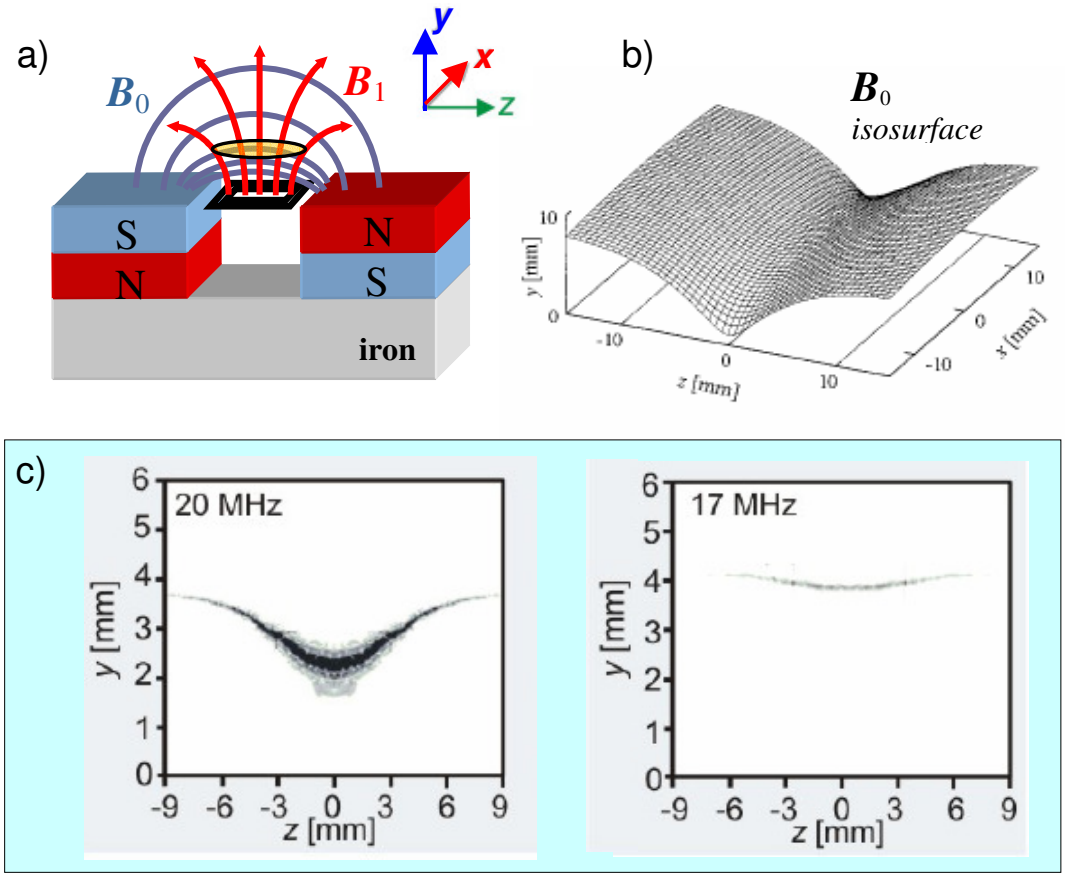

Fig. 3.3 a) The classical u-shaped NMR-MOUSE. The polarizing field $\boldsymbol{B}_0$ is parallel to the surface of the sensor in the region of interest. The $\boldsymbol{B}_1$ field is produced by a squared surface coil creating a sensitive volume with the main dimensions in the lateral *x, z*-plane. b) Calculated $\boldsymbol{B}_0$ isosurface profile close to the surface of the u-shaped magnet [Bal1]. c) The sensitive volume of the u-shaped NMR-MOUSE at different positions along the perpendicular direction [Anf2].

A flat or even concave profile can be obtained in x-direction by adjusting the spacing between two parallel u-shaped sensors [Per1]. For such a sensor, the measurement depth limit can be increased from several mm to few cm either by increasing the dimension of the magnet blocks or the distance between them but maintaining the ratio of the distances. The first approach assumes a larger and heavier sensor while the second approach avoids this inconvenience on the expense of sensitivity. These are the basic ideas behind the profile-NMR-MOUSE which will be presented in Section 4.4. The same happens with the sensitive volume. Close to the magnet it has the cross-sectional shape of a soup dish [Anf2] which flattens out with increasing distance from the coil (Fig. 3.3 c). A mathematical computation of the $\boldsymbol{B}_0$ and

$\boldsymbol{B}_1$ fields in the surface-magnetic-charge respectively the Biot-Savart approximations as well as of the spin system evolution in these fields and finally of the NMR signal of the unilateral sensor are given in [Bal].

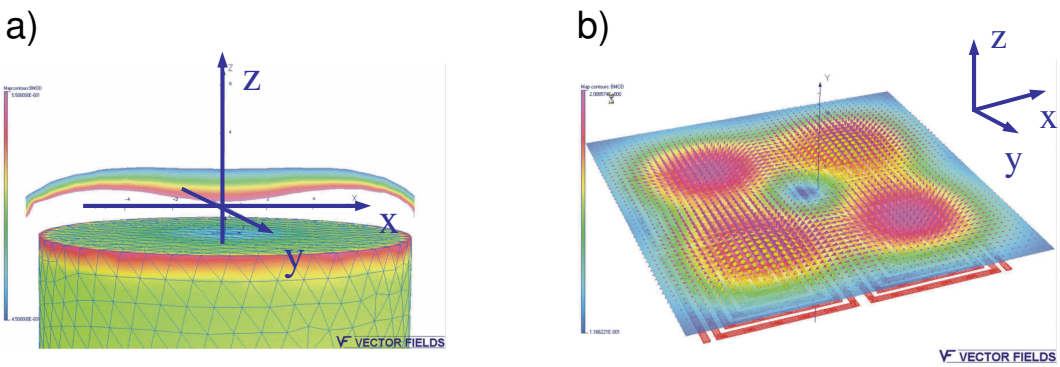

Fig 3.4 a) Schematic representation of the bar-magnet NMR-MOUSE and the Vector Fields simulation of its $\boldsymbol{B}_0$ (x,z) field. b) A coil for the bar-magnet NMR-MOUSE is the butterfly coil. Its $\boldsymbol{B}_1$ (x,y) field distribution at 1.2 mm distance provides a broad coverage in the plane but at several discrete volumes.

Another model of unilateral sensors uses bar-shaped magnets and different types of surface coils like the figure eight coil, the RPA (rubber process analyser) coil, the butterfly coil (Fig. 3.4 b), etc for generation of $\boldsymbol{B}_1$ fields with the main component parallel to the surface of the magnet. The important properties of the bar-magnet NMR-MOUSE are the constant gradient of the static magnetic field $\boldsymbol{B}_0$ in the central part of the magnet extending in the z direction from the pole face into the sample (Fig. 3.4 a). As a result, the field profile is linear in a given region along this direction. This makes possible the measurements of diffusion. Furthermore, the bar magnet concept considerably simplifies the construction of NMR-MOUSE sensors.

3.3.2 Signal-to-noise ratio

General approach

An important issue in NMR and particularly in single-sided NMR is the signal-to-noise ratio (SNR). An reason for the development of high-resolution NMR spectrometers employing super-conducting, rather than iron, magnets has been the fact that the SNR

available is proportional to the Larmor frequency to the three-halves power [Hou1]. But, it is always difficult accurately to compare the performances of different instruments as a variety of factors come into play. Nevertheless, it is generally felt that the improvement obtained is not always the expected one. The usual formula for the signal-to-noise ratio available after a 90° pulse is given by

$$\Psi_{\mathrm{rms}} = K\eta \boldsymbol{M}_0 (\mu_0 Q \omega_0 V_{\mathrm{c}} / 4Fk_{\mathrm{B}}T_{\mathrm{c}}\Delta f)^{1/2}, \tag{3.2}$$

where K is a numerical factor (: 1) dependent on the receiving coil geometry, η is the filling factor, namely the fraction of the coil volume occupied by the sample, $\boldsymbol{M}_0$ is the nuclear magnetization which is proportional to the field strength $\boldsymbol{B}_0$, μ_0 is the permeability of free space, Q is the quality factor of the coil, ω_0 is the Larmor angular frequency, V_{c} is the volume of the coil, F is the noise figure of the preamplifier, k_{B} is Boltzmann's constant, T_{c} is the probe temperature, and Δf is the bandwidth (in Hertz) of the receiver.

We may consider that the primary factors involved in any analysis of SNR are those contained within the equation. Eq. 3.2 contains four unknowns, K, η, Q and F, of which only two (Q and F) are easily measurable. The definition of filling factor $\eta = V_{\mathrm{s}}/2V_{\mathrm{c}}$, where V_{s} is the sample volume, may well be satisfactory for a given solenoid, but its validity for other dimensions and coil configurations can be questioned. Furthermore, the interactions between the various factors are manifold and mostly strong. In these conditions, an exact evaluation is difficult to be done. A different method of calculation which gives a direct insight into the various factors involved and which removes some of the interdependencies inherent in Eq. 3.2. is based on the principle of reciprocity. Considering the induction field $\boldsymbol{B}_1$, produced by a coil carrying unit current, and a magnetic dipole $\mathbf{m}$ placed at point in this field and set rotating about a static field $\boldsymbol{B}_0$ (perpendicular to $\boldsymbol{B}_1$), it may easily be shown that the induced electromotive force (emf) in the coil is given by [Hou1]

$$\xi = -(\partial / \partial t)\{\boldsymbol{B}_1 \cdot \mathbf{m}\}, \tag{3.3}$$

where $\boldsymbol{B}_1$ is the field produced by the unit current at $\mathbf{m}$. It is straightforward that the same dipole displaced at another position, further from the coil, will induce an alternating signal with different (smaller) amplitude. It follows that for a sample of volume V_{s} which has been recently subjected to a 90° pulse, we need only know the

value of $\boldsymbol{B}_1$ at all points in the sample to be able to calculate the emf induced in the coil. Thus, if $\boldsymbol{M}_0$ lies in the *xy* plane,

$$\xi = -\int_{\text{sample}} (\partial / \partial t)\{\boldsymbol{B}_1 \cdot \boldsymbol{M}_0\}\,\mathrm{d}V_\mathrm{s}. \tag{3.4}$$

The calculation of $\boldsymbol{B}_1$ is feasible for most shapes of coil, if it may be considered to be reasonably homogeneous over the sample volume, the calculation is considerably simplified as the integration of Eq. 3.4 becomes trivial, giving

$$\xi = K\omega_0 (\boldsymbol{B}_1)_{\mathrm{xy}} \boldsymbol{M}_0 V_\mathrm{s} \cos \omega_0 t, \tag{3.5}$$

where K is an "inhomogeneity factor" which may if necessary be calculated, $(\boldsymbol{B}_1)_{\mathrm{xy}}$ is the component of $\boldsymbol{B}_1$, perpendicular to the main field $\boldsymbol{B}_0$. The phase has been neglected. The magnetization $\boldsymbol{M}_0$ is given by

$$\boldsymbol{M}_0 = N\gamma^2 \mathrm{h}^2 I(I+1)\boldsymbol{B}_0 / 3k_\mathrm{B}T_\mathrm{s}, \tag{3.6}$$

where N is the number of spins at resonance per unit volume, γ is the magnetogyric ratio, and T_s, is the sample temperature. As $\omega_0 = -\gamma|\boldsymbol{B}_0|$ it follows from Eq. 3.5 and 3.6 that the emf induced in the coil is proportional to the square of the Larmor frequency.

The next step is to take into account the noise. In a correctly designed system, this should originate solely from the resistance of the coil. As the dimensions of the coil are inevitably much less than the wavelength of the radiation involved, the radiation resistance is negligible, and it should therefore be possible to predict the thermal noise present purely on the basis of the equation [Hou1]

$$V = (4k_\mathrm{B}T_\mathrm{c}\Delta f R)^{1/2}. \tag{3.7}$$

where T_c, is the temperature of the coil and R its resistance. Unfortunately, the calculation of R may not be performed accurately, and it is solely this factor which leads to uncertainty in the theoretical prediction of signal-to-noise ratio. At the frequencies of most interest in NMR (say >5 MHz) the "skin effect" associated with the magnetic field generated by a current ensures that that current flows only in regions of the conductor where there is also a magnetic flux. Thus, for a long, straight cylindrical conductor, the current flows in a skin on the surface [Hou1]. In this conditions the calculated result is

$$R = (1/p)(\mu\mu_0\omega_0\rho(T_\mathrm{c})/2)^{1/2}, \tag{3.8}$$

where l is the length of the conductor, p is its circumference, μ is the permeability of the wire, and $\rho(T_c)$ is the resistivity of the conductor, which is a function of temperature. The situation is considerably more complicated if the conductor is not cylindrical, and worse still, if there are many conductors in close proximity, as is, in effect, the case with a coil, the magnetic field created by the current of one conductor influences the distribution of current in another.

By combining Eq. 3.5 with 3.8 we arrive to an expression for the SNR [Hou1],

$$\Psi_{\mathrm{rms}} = \frac{K(\boldsymbol{B}_1)_{\mathrm{xy}} V_{\mathrm{s}} N \gamma \hbar^2 I(I+1)}{7.2 k_{\mathrm{B}} T_{\mathrm{s}}} \cdot \left(\frac{p}{F k_{\mathrm{B}} T_{\mathrm{c}} l \zeta \Delta f} \right)^{1/2} \cdot \frac{\omega_0{}^{7/4}}{[\mu \mu_0 \rho(T_{\mathrm{c}})]^{1/4}}. \tag{3.9}$$

where ζ is the proximity factor and F is the noise figure of the preamplifier. At a first sight, this equation appears unmanageable, but this is in fact not the case. First, the unknowns η and Q of Eq. 3.2 are absent as they have been replaced by a single function ζ, which, from experience, is reasonably well known, and second, the number of factors in Eq. 3.9 which are variable in a given experimental situation is small. These factors are: $K(\boldsymbol{B}_1)_{\mathrm{xy}}$, the effective field over the sample volume produced by unit current flowing in the receiving coil, p the perimeter of the conductor, and l the length of the conductor, which are all dependent on the coil geometry and others like the temperature of the coil T_c, the material of the coil $\rho(T_c)$, and finally the quality of the preamplifier, F.

The major advantage of Eq. 3.9 is that it is applicable to any coil geometry, for which ζ changes insignificantly having a change of configuration provided by the separation of the windings negligible in comparison with the overall dimensions of the coil. Necessary to be said is that, in contradiction with Eq. 3.2, Eq. 3.9 is not valid for a solenoid.

Signal-to-noise ratio in single-sided NMR

The original expression for the SNR derived by Hoult [Hou1] cannot be employed in the strongly inhomogeneous fields of single-sided sensors like the NMR-MOUSE, as off-resonance excitation, an inhomogeneous rf field, and a limited sensitive volume within a large object have to be taken into account. Here the $\boldsymbol{B}_0$ and $\boldsymbol{B}_1$ fields cannot be taken anymore as uniform, so that a distribution of transverse magnetization has to be considered depending on the space dependent $\boldsymbol{B}_0$ ($\boldsymbol{r}$) and $\boldsymbol{B}_1$ ($\boldsymbol{r}$) field profiles and the

used pulse sequence as well. Furthermore, due to the strong $\boldsymbol{B}_0$ ingomogeneity the pulses become selective leading in the case of pulse length modulated flip angles to pulse length modulated sensitive volumes. For this reason, pulse-amplitude modulation is preferred in single-sided NMR. Meanwhile the 90° pulses excluding a small fraction of the sensitive volume are not perfect 90° pulses leading to decays of the transverse magnetization with a $T_{2\mathrm{eff}} > T_2$, and the sensitive volume changes with the echo number.

Considering the extreme case of strongly inhomogeneous but linear fields, a new expression of the SNR has been computed for or a particular magnet and coil geometry and a given pulse sequence [Per3] and, although for computational reasons some approximations have been introduced, the result is in good accordance with the measured values. Considering the same expression for the noise as in the general case, the particular form of the root-mean-square SNR for a u-shaped NMR-MOUSE is given by [Per3]:

$$|S/N| = \left\{ \frac{2\pi^{1/2} N \gamma^{5/2} \mathrm{h}^2 I(I+1)}{2^{1/2} 6 (k_\mathrm{B} T)^{3/2}} \right\} \times \left\{ \frac{\boldsymbol{B}_0{}^2}{\boldsymbol{G}_{0y}} \right\} \times l^2 \left\{ \frac{\boldsymbol{B}_{1\perp}}{iR^{1/2}} \right\}^{3/2} \times P^{1/4} \tag{3.10}$$

This equation is the product of four terms. The first term depends only on the sample, the second one on the magnet, the third one on the rf coil, and the last one on the spectrometer which supplies the rf power. But the dependence is only with $P^{1/4}$, so that an improvement of S/N by a factor of two requires a factor of 16 in rf power. The second and the third factor are crucial for the design of the sensor. The SNR depends on the inverse gradient strength, i. e. on $\boldsymbol{G}_{0y}^{-1}$, while in conventional NMR it scales with $\boldsymbol{G}^{-1/2}$. In addition, the sensitivity depends on the rf coil by the factor $\boldsymbol{B}_{1\perp}/iR^{1/2}$ to the power of 3/2 instead of 1 as a result of the fact, that the rf coil is critical for excitation and detection while in homogeneous fields it is critical only for detection. Eq. 3.10 is valid for single-sided NMR sensors with a strong gradient in the perpendicular direction. Although it has been derived for a u-shaped sensor [Per3], it will be valid approximately also for the bar-magnet NMR-MOUSE. Here the $\boldsymbol{B}_0$ gradient also points along the perpendicular direction, and an rf coil that is suitable for such type of sensor does not generate a constant field profile either. The dimension of the coil defines the lateral size of the sensitive volume here too.

Chapter 4

Characterization of Materials by Single-Sided NMR

Single-sided NMR is a powerful analytical tool for non-destructive characterization of materials. The tested samples cover a great range of applications: from elastomers of great importance in materials science, to the most complicated biological structures, the essence of biomedicine. The investigation can be simple NMR relaxometry with a bar or u-shaped magnet NMR-MOUSE, profile imaging, and up to 2D and 3D imaging using a unilateral NMR tomograph [Cas2, Cas3, Per2]. Applications of one- and multi-dimensional single-sided NMR for characterization of heterogeneous polymers as well as some of the first applications of the unilateral NMR imaging technique in bio-medicine will be presented in the following.

4.1 NMR of polymers

An important objective in materials science is the establishment of relationships between the microscopic structure or molecular dynamics and the resulting macroscopic properties. Once established, this knowledge then allows the design of improved materials. Thus, the availability of powerful analytical tools such as NMR is one of the key issues in polymer science. It allows one to study structure, and molecular dynamics.

NMR in its different variants provides information from the molecular to the macroscopic length scale and on molecular motions from 1 to 10^{10} Hz. It can be applied to crystalline as well as to amorphous samples which is of particular importance for the study of polymers. Moreover, NMR can conveniently be applied to polymers since they contain predominantly nuclei that are NMR sensitive such as ^{1}H and ^{13}C.

The information at the molecular level can be correlated with macroscopic properties of polymers and provides the basis for a better design of material properties for specific applications. NMR can provide information on such important areas as the chain dynamics in elastomers, the local structure, residual couplings (induced by chemical cross-links and topological constraints), dynamic order parameters, internuclear distances, intermolecular interactions, the effects of fillers on molecular motions, and segmental orientation under mechanical stress and others.

4.1.1 Cross-linked polymers

The cross-linking of a rubber converts the plastic raw mixture into the rubber-elastic network. The cross-linking is usually realized by connecting the unsaturated positions of the backbone or side groups of different polymer chains to each other. The long macromolecular polymeric chains which are locally interconnected by cross-link points form a complex elastomer network (Fig. 4.1) Cross-link density and parameters relating to the network structure can be measured by analysis of the transverse magnetization decay and the longitudinal relaxation. The end-to-end vector $\boldsymbol{R}(x,y,z)$ represents the geometrical distance between two cross-link points and it is oriented with a β angle to the static magnetic field $\boldsymbol{B}_0$. The shorter segments are the Kuhn segments (statistical segments) and the number of Kuhn segments (N) between two cross-link points gives important information about the cross-link density (C). The basic relation for the mechanical determination of cross-link density is given by [Gas1]:

$$C = \frac{\rho \boldsymbol{R} T}{M_{\mathrm{c}}} \propto \frac{1}{N}, \tag{4.1}$$

where, ρ is the density of the elastomer network and M_c is the molecular weight of the chain segment. The relation above shows that the cross-link density is inversely proportional to the number of Kuhn segments.

Cross-linked elastomers possess a special property called viscoelasticity. It is also known as anelasticity and refers to materials that exhibit both viscous and elastic characteristics when undergoing plastic deformation. Viscous materials, resist shear flow and strain linearly with time when a stress is applied. Elastic materials strain instantaneously when stretched and just as quickly return to their original state once the stress is removed. Viscoelastic materials have elements of both of these properties and, as such, exhibit time dependent strain. Whereas elasticity is usually the result of bond stretching along crystallographic planes in an ordered solid, viscoelasticity is the result of the diffusion of atoms or molecules inside of an amorphous material

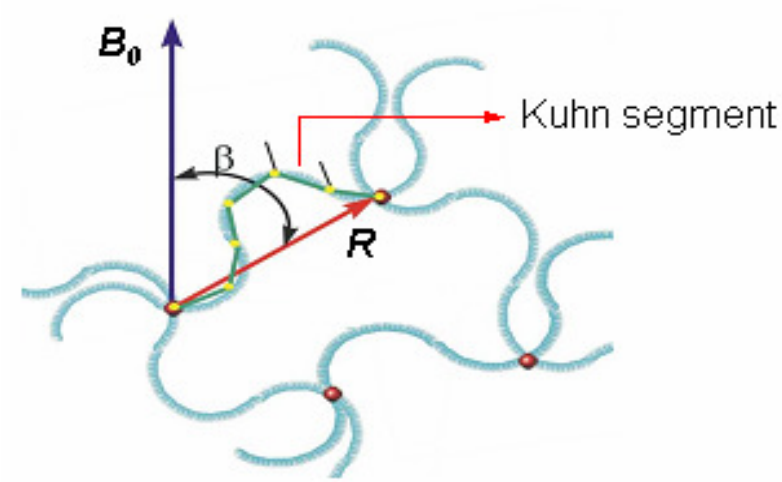

Fig. 4.1 The complex cross-link elastomer network.

Visco-elasticity can be measured by using oscillating stress-strain experiments at different frequencies and detecting the response of the material. During a deformation, the energy introduced is stored by an elastic part and is dissipated by the viscous part. The dissipation factor is given by [Gas1]:

$$\tan\delta(\omega) = \frac{G''(\omega)}{G'(\omega)}, \tag{4.2}$$

where, G' and G'' are the storage and dissipation moduli and they give a quantitative description of a visco-elastic behavior. The moduli are modeled by a combination of spring and dashpot elements simulating elastic and viscous properties, and they can be described as functions of frequency or time.

4.1.2 Network properties by transverse magnetization relaxation

NMR transverse magnetisation relaxation experiments are extensively used for quantitative analysis of the density of chemical cross-links, temporary and trapped chain entanglements and physical network junctions which are formed in filled rubbers, semicrystalline and ion containing elastomers, and for determination of molecular-scale heterogeneity of polymer networks ([Lit1], and references therein).

The simplest model to describe chain statistics from the NMR point of view is a chain of freely jointed segments of fixed length [Coh1]. Such a chain may be rescaled in several hierarchical steps according to the time scale of the motions which takes place at different space scales, compared to the time scale defined by the NMR spin interactions. All intra-chain motions are assumed to be fast enough to average elementary interactions, whereas junction average positions appear static.

Considering a linear chain of N statistical segments, fixed at its extremities, an average orientation is induced along the chain by these constrains. To estimate the effect of this average orientation on NMR parameters, the simplest picture is to consider that each segment carries isolated pairs of spins, usually protons (two-spin approximation) [Dem1]. Within this framework, the time evolution of the transverse magnetization $\boldsymbol{M}_{\mathrm{xy}}(t)$ for a spin pair attached to a chain may be written in the very simple form

$$\boldsymbol{M}_{\mathrm{xy}}(t) = \mathrm{Re}\left[\boldsymbol{M}_0 \exp\left\{-\frac{t}{T_2}\right\} \exp\{i\omega_{\boldsymbol{R}} t\}\right], \tag{4.3}$$

where $\boldsymbol{M}_{\mathrm{xy}}(t)$ is the initial polarization, T_2 is the transverse relaxation time related to the fluctuating part of the dipolar Hamiltonian, and $\omega_{\boldsymbol{R}}$ is the residual dipolar interaction in angular frequency units. Other theories of transverse relaxation ([Fed1], and references therein) are more complex. Considering a highly disordered polymer network, the end-

to-end vector components $\boldsymbol{R}(x, y, z)$ may be supposed to obey ideal, the Gaussian statistics, ie,

$$\boldsymbol{P}(\boldsymbol{R}) = \left(\frac{3}{2\pi Na^2}\right)^{3/2} \exp\left\{-\frac{3}{2}\frac{\boldsymbol{R}^2}{Na^2}\right\}, \tag{4.4}$$

where a is the length of the statistical segment. The overall evolution of the complex transverse magnetization is then obtained by averaging equation 4.3 over the end-to-end vector distribution. This yields [Sot1]

$$\boldsymbol{M}_{\mathrm{xy}}(t) = \mathrm{Re}\left[\boldsymbol{M}_0\left(1-\frac{2}{3}iD_{ij}N_e^{-1}t\right)^{-1/2} - 1/2\left(1+\frac{1}{3}iD_{ij}N_e^{-1}t\right)^{-1} \exp\left\{-\frac{t}{T_2}\right\}\right], \tag{4.5}$$

where D_{ij} is the dipolar coupling constant for a spin pair and N_{e} is the effective number of statistical segments. At short times, ie, for $\Delta^2 N_e^{-1} t^2 = 1$ the transverse relaxation decay has a Gaussian behaviour corresponding to the presence of the residual dipolar couplings.

4.1.3 Heterogeneities in rubbery materials

Several types of heterogeneity may occur in rubbery materials: (*1*) molecular scale heterogeneity, which is caused by the chemical heterogeneity and network defects on the molecular level; (*2*) morphological heterogeneity of rubbery compounds due to a spatially heterogeneous distribution of components and filler in the compound; (*3*) spatial heterogeneity due to a difference in curing conditions such as temperature and concentration of vulcanisation agents throughout the sample volume. The main processes that lead to the defects are as follows [Dem1]:

Mixing processes

Technical elastomers are blends of up to about 30 different compounds like natural rubber, styrene–butadiene rubber, silicate and carbon-black fillers, and mobile components like oils and waxes. Improper mixing leads to inhomogeneities with corresponding variation in mechanical and thermal properties. An important source of heterogeneities of this type is represented by filler clusters. Even the variance of the

distribution statistics of active filler may lead to heterogeneities detected as an average over a volume cell or voxel with the spatial resolution of NMR imaging.

Vulcanisation

Heterogeneous structures arise from effects of thermal conductivity, which lead to space-dependent temperature profile during the vulcanization process depending on the position of the heat source and on heat dissipation. As a result, inhomogeneous cross-link densities may be established [Smi1]. If the process of cross-linking is incomplete the defects represents by the free chains are also presents. The changes in segmental mobility from progress of the vulcanization reaction and from the associated sample temperature distribution can be monitored directly by the NMR imaging *in situ* [Fül2]. In the covulcanization of blends and sheets from different formulations, inhomogeneities in cross-link density max arise from differences in solubility and diffusion of curatives [Kle3].

Aging

The aging can be physical, chemical or mechanical depending on the aging agent. Physical aging processes are often induced by ultraviolet (UV) irradiation or other ionization radiations [Pal1] as well as exposure to heat together with chemical aging factors like oxygen, and biological mechanisms. Depending on the load applied, different mechanical aging processes are observed [Den1]. The action of electromagnetic radiation with high energy of the associated photons as well as nuclear irradiation will produce chain scission with decrease in the cross-link density and associated increase in chain mobility. Thermal oxidative aging usually leads to the formation of hardened surface layers in natural rubber (NR) as well as synthetic rubber (styrene-*co*-butadiene rubber (SBR) [Fül1, Blü11, Blü15, Knö1, Knö2, Chu1]. Typically, these layers approach a thickness of 200–300 μm and inhibit progress of the aging process further into the bulk of thin sample. The material hardening is explained by an increase in cross-link density. In the absence of oxygen, chain scission may dominate at elevated temperatures with an associated increase in the segmental mobility. Other types of aging involve aggressive fluids and gases. In this context, a sample of degraded rubber hose gas been investigated [Sar1], but also the degradation of

polyethylene pipes and the enzymatic degradation of biologically synthesized polymers [Spy1] have been studied through NMR imaging. Related investigations have been carried out on asphalts [Mik1]. Aging associated with swelling of the rubber particles has been observed in crumb-rubber modified asphalts [Mik2].

Mechanical load

Static mechanical load by strain leads to stretching of random-coil polymer chains in the direction of sample elongation and chain compression in the orthogonal directions. The value of the residual dipolar and quadrupolar couplings is increased by the mechanical load, and moreover, the distribution of the correlation times is also modified. Therefore, many NMR parameters sensitive to the residual dipolar couplings and slow motions can be used for characterization of the local stress–strain effects in heterogeneous elastomers [Kli1, Sch6, Sch7, Blü12]. Dynamic mechanical load leads to sample heating where the temperature distribution in dynamic equilibrium is determined by the temperature-dependent loss-modulus and the thermal conductivity of the sample. Because transverse relaxation rate (approximated by the T_2 relaxation) scales with the temperature, a T_2 map provides a temperature map of the sample [Pow1].

4.2 Unilateral NMR relaxometry

NMR relaxometry is a powerful method for the investigation of elastomers. Compared to conventional NMR the concept of the NMR-MOUSE does not restrict the sample geometry. Moreover, the method is fully non-destructive. The open magnet defines a sensitive spot with a characteristic magnetic field above its surface, from where the NMR signal is measured. The main characterization procedure requires that a correlation exists between the relaxation times and the material property of interest. An important example is the linear relationship between the spin-spin relaxation time T_2 and the cross-link density of elastomers, which is explored to determine the homogeneity and the degree of vulcanization of intermediate and final products in the rubber manufacturing business [Zim2].

4.2.1 Method

Transverse relaxation in NMR occurs when spins in different energy states change coherences. This results macroscopically in the loss of transverse magnetization. The precession of the transverse magnetization at the Larmor frequency is responsible for the detectable magnetic resonance signal. In the absence of an externally applied radio-frequency energy, the transverse magnetization decays exponentially to zero with a characteristic time constant of T_2, or more strictly T_2* (see Fig. 4.2), where T_2* is the spin-spin relaxation time composed of contributions from molecular interactions and inhomogeneities in the magnetic field.

The value of the relaxation time in a particular spin system depends on the spin interactions and the time scale of molecular motion [Blo3]. Both change with the state of the studied matter. Consequently, i.e., the cross-link density (which can indirectly be related to the molecular mobility of the polymer chains), can be monitored by transverse relaxation time measurements. The dipolar coupling for protons being of the order of KHz, T_2 which is sensitive to slow motions is strongly affected even by small changes of the effective dipolar coupling revealing differences in the cross-link density. The degree of crystallinity has a similar effect on T_2 and can be characterized with good accuracy in terms of relative values and their changes when compared to reference values.

Another determining factor for relaxation is the inhomogeneity of the polarizing field. The NMR signal after a $90_y°$ pulse (FID) decays much faster in the field gradients of single-sided sensors than in the highly homogeneous fields of super-conducting magnets. It is a consequence of the spatial distribution of isochromats which summed over the whole sensitive volume partially average out, ending up with an additional loss in transverse magnetization. For rigid polymers the FID decays fast (tens of microseconds to few milliseconds) due to the long correlation times (reduced molecular mobility). In this case the dead times of usual rf coils appear to be quite long for detection, truncating the FID and in most cases making impossible to acquire even a part of it.

The problem can be solved by using different pulse techniques presented in Chapter 2. The $180_x°$ radio-frequency pulses used to generate the echoes rephase the spins which have undergone T_2* decay. The gradual decline in the signal from

subsequent echoes reflects the transverse magnetization decay. The most important feature here is the experimental time. The measurement i.e., of a simple Hahn echo decay [Hah1, Hah2] although leads to a reliable value of T_2, it requires repetition of the experiment for many increments of the echo-time (t_E) so that the measurement time often turns out to be too long especially when many averagings are required. Consequently, when NMR relaxation is referred to mobile NMR, one mostly talks about the relaxation measured by CPMG-type (Carr, Purcell, Meiboom, Gill [Car1, Mei1]) multi-echo trains (Fig. 4.2), as multi-echo techniques are faster than single echo schemes. However, the relaxation time extracted from the envelope of the CPMG echo train is not the T_2 measured in homogeneous fields but an effective value (T_{2eff}) due to off resonance effects and non-ideal flip angles in the inhomogeneous $\boldsymbol{B}_0$ and $\boldsymbol{B}_1$ fields [Hue1, Bal1]. Moreover, typically T_2 is shorter than T_{2eff} as starting with the second echo, T_{2eff} is modulated not only by the Hahn echo decay, but also by the decay of the stimulated echoes, which is encoded by T_1 [Gut1]. This fact denotes a dependency of T_{2eff} on the $\boldsymbol{B}_0$ and $\boldsymbol{B}_1$ field profiles of the sensor, namely T_{2eff} measured with different single-sided sensors inside the same material in identical experimental conditions may be different.

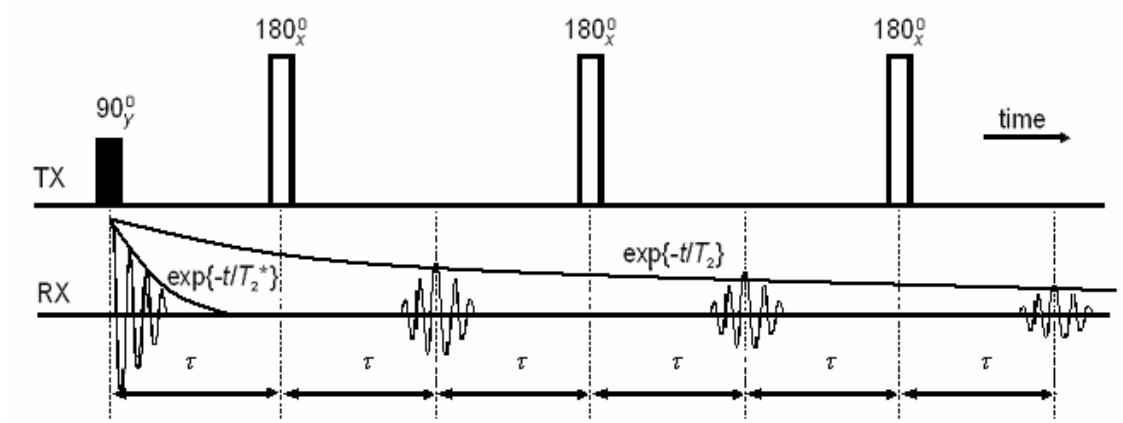

Fig. 4.2 Multi-echo CPMG sequence for stroboscopic observation of the magnetization decay. The envelope of the echo train is obtained at each echo centre by integrating the central part of the echo.

To extract the T_{2eff} information from the echo decays, different methods can be used. Fitting the magnetization decay envelope with a mathematical model function is the most commonly used approach. Consequently, the values of T_{2eff} can be extracted

with an accuracy which is limited by the fitting error. The simplest fit function is an exponential function (and in this case an average $T_{2\mathrm{eff}}$ over the material is obtained) or a sum of exponentials. However the echo decay, may present in some cases a more complex mathematical behaviour, i.e., for cross-linked elastomers where an accurate approach supposes the fitting of the decay not with an exponential, but rather with a function similar to the one given by Eq. 4.5. Consequently, the fit function has to be chosen in particular according to the specific material under study.

When a multi-term function is used, it is straightforward to consider that each term (exponential, gaussian, etc.) corresponds a different structural component of the material. In the case of a multi-exponential not only the molecular mobility of each phase but also their ratios can be calculated as the ratios of the exponential amplitudes. However the use of many exponentials assumes many fit parameters difficult to be controlled and interpreted if their number increases too much.

As a solution to this problem, in many cases, a stretched exponential function gives an equally good fit with only three fit parameters with an average $T_{2\mathrm{eff}}$ of the material over the whole sensitive volume,

$$f(t) = A \exp\left\{-\frac{1}{b}(t/T_{2\mathrm{eff}})^b\right\}. \tag{4.6}$$

The normalization of the exponent assures, that an exponential function is obtained for $b = 1$ and a Gaussian one for $b = 2$ [Blu16]. Its interpretation in terms of a material model, however, is not straightforward.

Another approach for extracting $T_{2\mathrm{eff}}$ from multi-echo decays is the normalization and integration of the total signal. It provides a quantity which is proportional to the average $T_{2\mathrm{eff}}$ of the material and is usually given in arbitrary units. Thus, without any calibration with $T_{2\mathrm{eff}}$, it can only be used to measure $T_{2\mathrm{eff}}$ ratios and relative variations.

4.2.2 Non-invasive quality control in the tire production

The quality control at different stages of the fabrication process is of great importance in the tyre industry. Typically any rubber formulation is tested on a rheometer to assess the material and vulcanization properties by means of rheometer torque. While these tests provide important information for the manufacturers, the final product cannot be probed

in this way. Mechanical properties of cross-linked elastomers are influenced not only by the volume-averaged cross-link density but also by the network heterogeneity such as distributions of residual sol, dangling chains, chain loops, and the heterogeneity of the cross-link density. Rubber products are 3D networks of macromolecular chains filled with various additives, such as waxes and mineral fillers or carbon black. The formation of cross-links and the distribution of filler particles are statistical. There are short and long inter-cross-link sections as well as regions with few and regions with many filler particles.

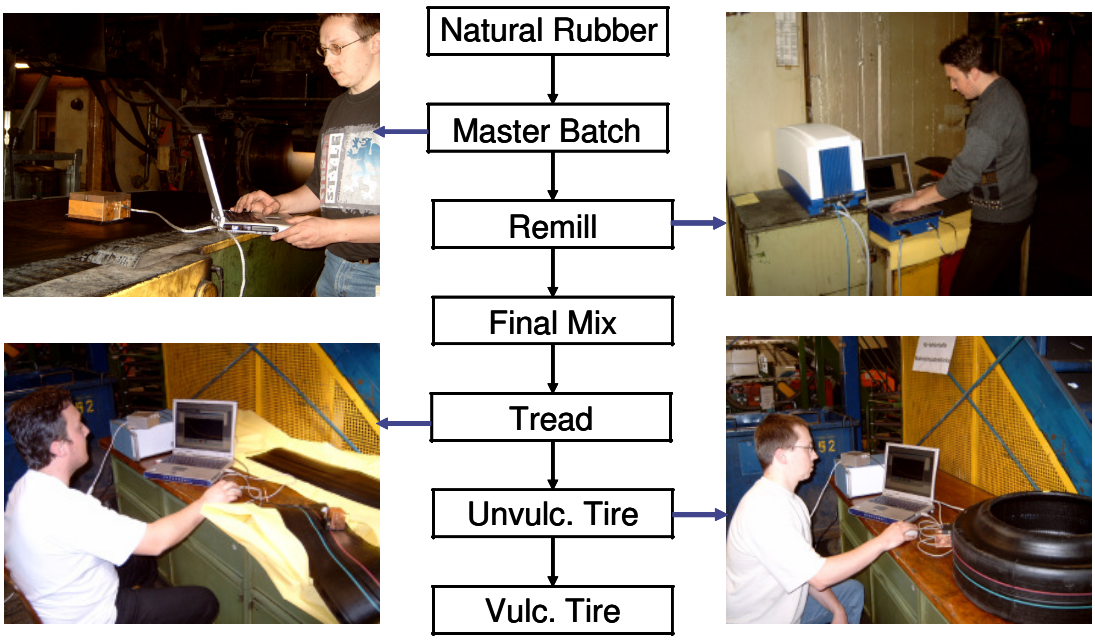

Fig. 4.3 Following the complete production of a tire by NMR in the factory. The photos are taken from different moments of the production showing the ease of investigations with the single-sided mobile

Unilateral NMR sensors like the NMR-MOUSE are powerful devices for quality control and nondestructive measurements not only of test samples but also of production intermediates and final products. Due to the high reproducibility of the measurements (about 1 %), the NMR-MOUSE can be employed for statistical analysis of the homogeneity of rubber samples [Gog1]. The NMR-MOUSE be carried and positioned to different spots of a flat sample. The samples can be investigated entirely non-destructively up to several millimeters in depth by placing the NMR-MOUSE in the spot to be measured. The size of each spot is determined by the size of the sensitive volume of the NMR-MOUSE. Typically it is a few square centimeter large and ca. 1 mm thick.

Compared to a rheometer and conventional NMR devices, the NMR-MOUSE offers the advantages of non-destructiveness, mobility, and the possibility to measure in the presence of ferromagnetic materials [Gog1].

The aim of this study was to test the NMR-MOUSE on-line as a non-destructive quality controller in the car tire production. A focal point was here the identification of processing steps where the sample homogeneity is most critical for the quality of the final product.

Samples

The first mixture in the tire fabrication process is the master batch. In the investigated case it contained three polymers (BR, SSBR, and NR) and fillers. Subjected to silanization at 100° C and after remixing at 50-60° C the next intermediate, the remill is obtained. Mixing the remill, with further additives yields the final mix. This final mix is calendered into sheets and thermally processed to obtain the tread sheets. These are joined together with steel belts and other components to build the tire which is subsequently vulcanized. Five tires were analyzed, each of them at five different positions around their external surfaces. The test positions on the tires have been marked, so that after vulcanization the measurements could be done at the same points.

Experimental

The dispersions in the raw polymer at different steps of the production were tested by the NMR-MOUSE following the complete process of tire fabrication (Fig. 4.3). The sensor was a bar-magnet MOUSE with a butterfly coil, operating at a radio-frequency of 18.3 MHz for protons. For each type of sample the rf circuit of the NMR-MOUSE was properly matched.

Table 4.1: NMR parameters for measurements in the tire factory

Parameter	value
Recycle delay	1.00 s
Scans	150
Frequency	18.30 MHz
90 – pulse	1.50 μs
180 – pulse	3.00 μs
Echo time t_E	50.00 μs
No. of echoes	200

To determine the relaxation time $T_{2\mathrm{eff}}$, the CPMG pulse sequence was employed using the same measurement parameters for the vulcanised and the unvulcanised tires. The experimental parameters are given in Table 4.1. In most elastomers the decay is non-exponential. Nevertheless, the decay time constant, $T_{2\mathrm{eff}}$ is a characteristic signature of the molecular mobility of the material.

$T_{2\mathrm{eff}}$ of the material was determined by fitting the experimental echo decay envelopes with a stretched-exponential model function (Eq. 4.6). The error in determining $T_{2\mathrm{eff}}$ estimated from consecutive measurements under the same experimental conditions at the same spot of the sample was less than 1%. Extensive signal averaging was employed for the final products containing ferromagnetic materials to compensate the loss in sensitivity.

Results

It was observed by means of the average $T_{2\mathrm{eff}}$ ($\overline{T_{2\mathrm{eff}}}$) that the first three mixtures have different hardness. Moreover, the homogeneity increases from the remill to the final mix (Fig. 4.4a. The highest is $\overline{T_{2\mathrm{eff}}}$ of the remill, which is also the least homogeneous. In the next step $\overline{T_{2\mathrm{eff}}}$ of five tread sheets was measured at five different positions and averaged for each sheet. The same tread sheets were processed in tires and the relaxation values measured at the same spots on the unvulcanised and the vulcanized tires. The resultant values are compared in Fig. 4.4b for all tires.

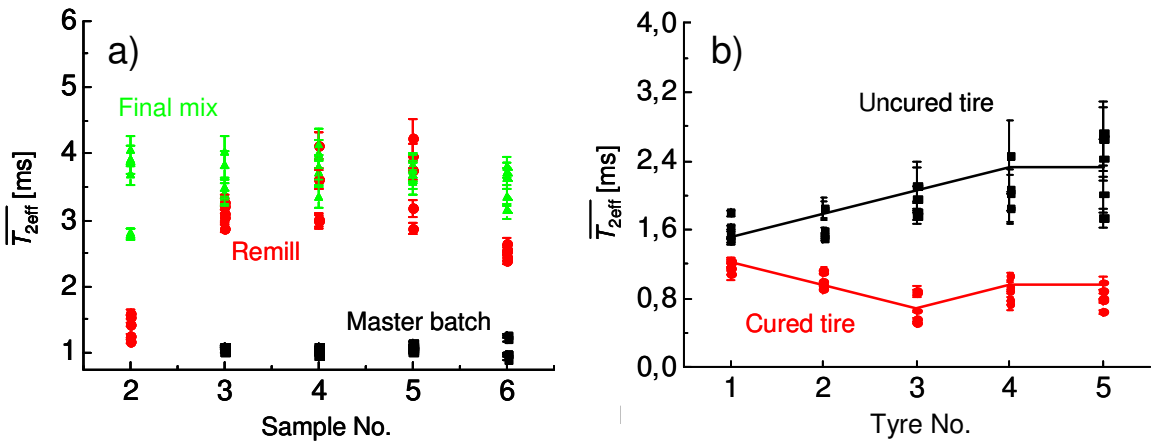

Fig 4.4 a) $\overline{T_{2\mathrm{eff}}}$ measured with the NMR-MOUSE for the master batch, the remill, and the final mix. b) $\overline{T_{2\mathrm{eff}}}$ distributions at 5 different measurement positions for 5 different tires unvulcanised and vulcanized.

$\overline{T_{2\text{eff}}}$ is shorter for the vulcanized rubber due to the cross-links produced during vulcanization. The homogeneity of the cured product increases as a result of diffusion of the components during the vulcanization process. The softer the unvulcanised material, the better is its homogenization by component diffusion. Nevertheless, the homogeneity of the pre-vulcanized product is very important as the most homogeneous is the tire no. 1, which was most homogeneous already before curing. The presence of the steel belt was a disturbing factor leading to some changes in the field profiles of the sensor and acting as antenna for the external noise, fact showed by the larger error bars.

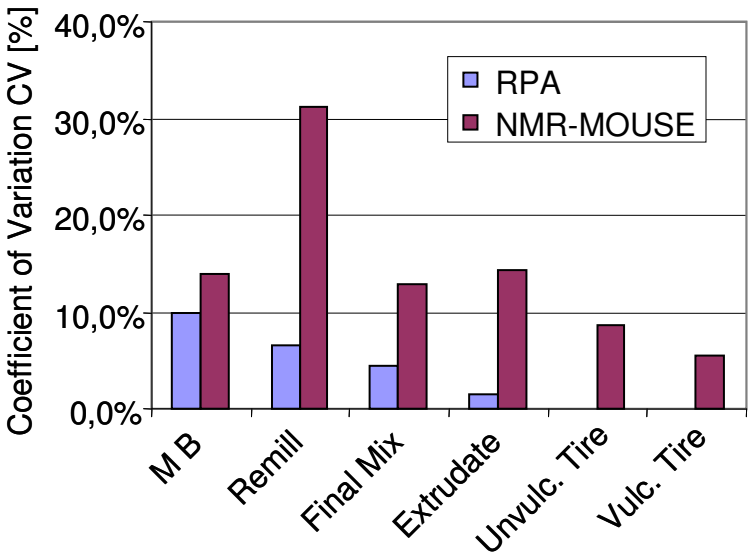

Fig. 4.5 Spread of RPA and NMR parameters for the different intermediate products during tire fabrication. The CV values of the RPA and NMR-MOUSE data demonstrate that the homogeneity essentially improves from one production step to the next, but NMR is more sensitive to variations in

For comparison, the samples were also tested by a Rubber Process Analyzer (RPA). The coefficients of variation (CV) of the initial RPA torque from the Payne diagrams and the CV values from the $\overline{T_{2\text{eff}}}$ measurements are compared in Fig. 4.5. The overall dependence is similar: the homogeneity of the products increases from one step of the production to the next. However, the largest spread in data was obtained for the master batch with RPA whereas it was obtained for the remill with NMR. The spread in CV is larger for NMR than for RPA, indicating that NMR is more sensitive to variations of material properties. This shows that RPA and NMR provide similar but not identical

information. The RPA measurements are very sensitive to the filler, while NMR relaxation is more sensitive to the chain segment mobility. Furthermore, RPA is not suited to investigate the finished product. This can only be done by NMR.

4.2.3 Relaxometry on aged PE pipes

The NMR relaxation parameters as for example transverse magnetization relaxation, are sensitive to segmental fluctuations in a frequency range of a few kilohertz, which is typical for the slow molecular motions. In this range, the molecular motion is directly related to the mechanical properties of solid polymers. All these properties depend on the strength of the residual dipolar interaction, which determines the decay of the NMR signal.

As $T_{2\mathrm{eff}}$ is related to the structure, the spread in $T_{2\mathrm{eff}}$ characterizes the heterogeneity of the material. Often, the inhomogeneities appear during fabrication, as a consequence of improper mixing and processing. Furthermore, usage and ageing induce major changes in the material structure. The changes in temperature, pressure, or aging processes induce differences of relative crystallinity that can be monitored by NMR in general and mobile NMR in particular.

Experimental

To detect the ageing effects in used polyethylene (PE) products, the unilateral NMR relaxometry method was implemented. Several PE pipes with visible defects on their external surfaces (Fig. 4.6a and 4.7a) were investigated. These pipes were used for several years underground as water pipes in the conditions of continuous pressure and temperature fluctuations.

The measurements were carried out in small steps along the external surfaces of the pipes, at depths of about 2 mm. The device was a “U”-shaped NMR-MOUSE operating at a resonance frequency of 17.3 MHz for protons. The pulse sequence was the CPMG multi-echo sequence. The temperature fluctuations during experiments were small so that this influence could be neglected. The experimental parameters are presented in Table 4.2. Five measurements were carried out in each point for data

averaging. The relaxation curves have been fitted with a bi-exponential function. Due to the field inhomogeneities, the $\overline{T_{2\mathrm{eff}}}$ values are mixtures of T_1, T_2, and $T_{1\rho}$ with a higher contribution of the transverse relaxation time.

Table 4.2. Experimental parameters for $T_{2\mathrm{eff}}$ measurements on PE pipes

Parameter-Name	Parameter-Value
Radio-frequency Value	17.3 MHz
90° Pulse Length	3 μs
Recycle Delay	0.7 s
Echo Time	0.035 ms
Number of Echoes	256
Number of Scans	1024

Results

The two constants, $\overline{T_{2\mathrm{effL}}}$ (a long $\overline{T_{2\mathrm{eff}}}$ value) and $\overline{T_{2\mathrm{effS}}}$ (a short $\overline{T_{2\mathrm{eff}}}$ value), characterize two main phases: an amorphous phase and a crystalline phase of the polymer. However there are intermediate phases too, which can be observed if more exponentials are included in the fitting function, but a good separation between them is often difficult to achieve. Heterogeneities usually represent structural and molecular mobility changes that occur on time scales that affect the relaxation rates. Most often the two relaxation times are not affected symmetrically.

Fig. 4.6 b depicts the $\overline{T_{2\mathrm{effL}}}$ values for one of the PE pipes. A zoom in of a major crack on the pipe surface is displayed (Fig. 4.6a). The measurement points are marked along the crack, and in positions where no major ageing effects are optically visible. The error bars represent the average standard deviations of the $\overline{T_{2\mathrm{effL}}}$ values acquired from the same spot of the sample during several consecutive measurements carried out in the same experimental conditions. In the first four measurement points (from left to right) $\overline{T_{2\mathrm{effL}}}$ is large suggesting a material with higher segmental mobility. These data points lay around the value of 0.87 ms inside the experimental error range proving that the material is quite homogeneous. In the crack position, $\overline{T_{2\mathrm{effL}}}$ decreases to values around

0.80 ms with a minimum of 0.73 ms. These points, out of the error range of the zone without visible damage, suggest a different network structure, a harder or less elastic material. This can be a result of increased crystallinity or strained polymer chains around the crack. Furthermore the fluctuations of $\overline{T_{2\mathrm{effL}}}$ in the damaged zone are high suggesting a highly inhomogeneous material.

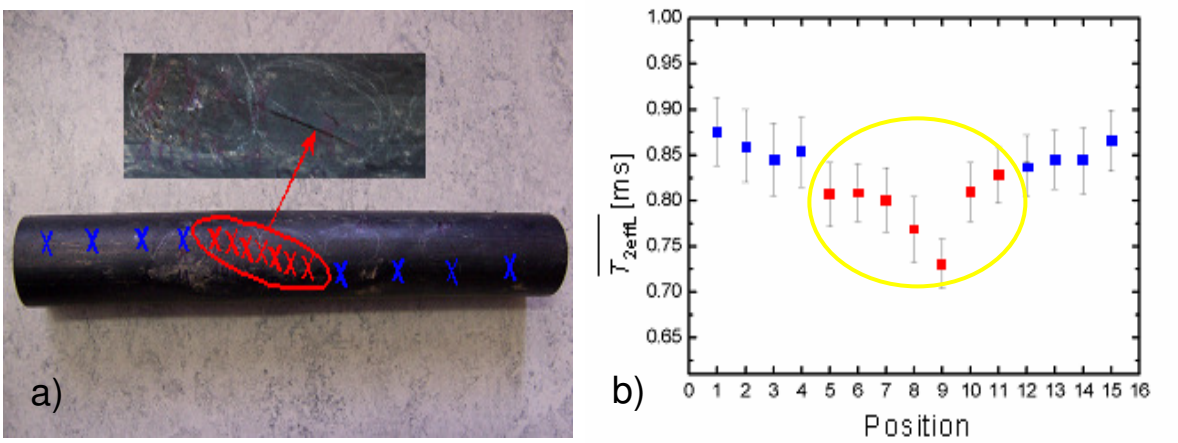

Fig. 4.6 a) Aged PE pipe with a visible crack (zoomed in) on its surface. b) $\overline{T_{2\mathrm{effL}}}$ was measured in the marked points (the values obtained along the crack are encircled).

Figure 4.7a depicts another pipe with a cross cut. The measurements were done using the same experimental parameters as in the previous setup. $\overline{T_{2\mathrm{effL}}}$ was measured on the pipe in eleven points: six positions along the cut and five reference positions far away from the damaged zone. For this pipe the same dependence of $\overline{T_{2\mathrm{effL}}}$ as for the first pipe was observed. Around the defect, $\overline{T_{2\mathrm{effL}}}$ decreases suggesting a harder material with less segmental motion. The variations in $\overline{T_{2\mathrm{effS}}}$ followed the same trend in both cases but with smaller relative variations.

Strong mechanical impact can induce changes in the initial semi-crystalline structure of PE. The morphology changes by reordering of the polymer chains, first in the amorphous and at higher impact also in the crystalline domains. This behavior corresponds to an increase of the relative amount of the crystalline phase in the damage position. The decrease of $\overline{T_{2\mathrm{effL}}}$ in the crack zone compared to the reference zone without visible damages can be attributed to this effect.

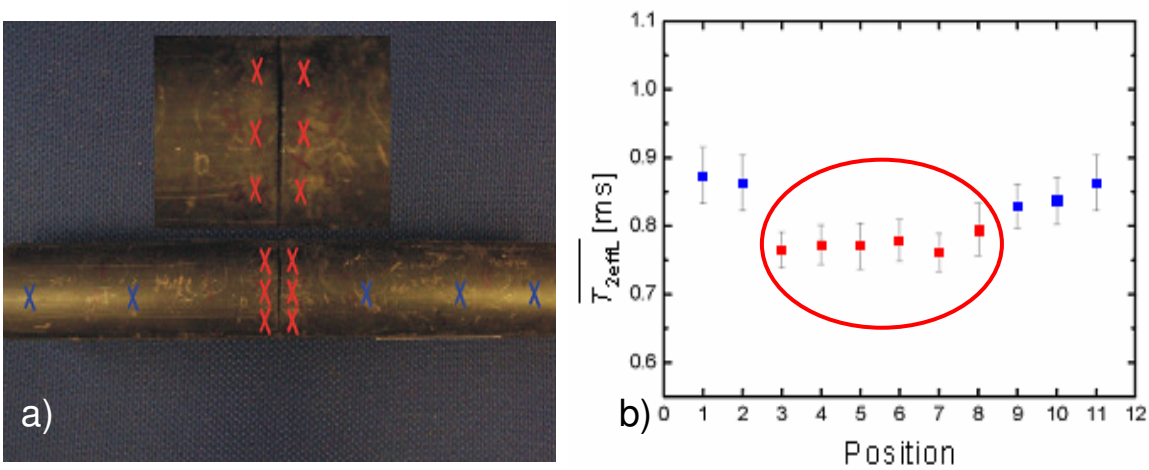

Fig. 4.7 a) Aged PE pipe with a cut (zoomed in) on its surface. b) $\overline{T_{2effL}}$ measured in the marked points. Again the transverse relaxation values obtained along the cut are encircled.

It is obvious that depending on the type and strength of the mechanical action applied upon the pipe, the degree of heterogeneity at the damaged position will be different. In our case, the fluctuations of $\overline{T_{2effL}}$ are larger for the cracked pipe (Fig 4.6b) than for the cut one (Fig. 4.7b). It can be explained by the regular shape of the cut. Other strong mechanical actions like impact, stress, torsion, produce instead a defect with a random shape and increased local heterogeneity of the material. This makes it possible to discriminate different mechanical aging agents by means of the spatial relaxation time distribution.

4.2.4 *In situ* NMR at a stress-strain device

The stress and strain characteristics are among the most important properties of elastomer and other materials. To determine the mechanical properties of a cross-linked natural rubber (NR) for example, the sample is tested with a stress-strain device to observe the fatigue with the number of strain cycles, or the stress-strain diagram of a single experiment is recorded until the sample breaks. Spatial distributions of cross-links and fillers result in a distribution of the material properties most importantly the modulus over the product. Thus, the characterization of the changes induced in cross-linked NR samples by stretching is a challenging topic for mobile NMR. Consequently,

a special NMR sensor was built for measuring $T_{2\mathrm{eff}}$ *in situ* at the stress-strain device [Gog2]. The same sensor can also be used to follow the change in NMR parameters during mechanical fatigue tests for prediction of the time to failure.

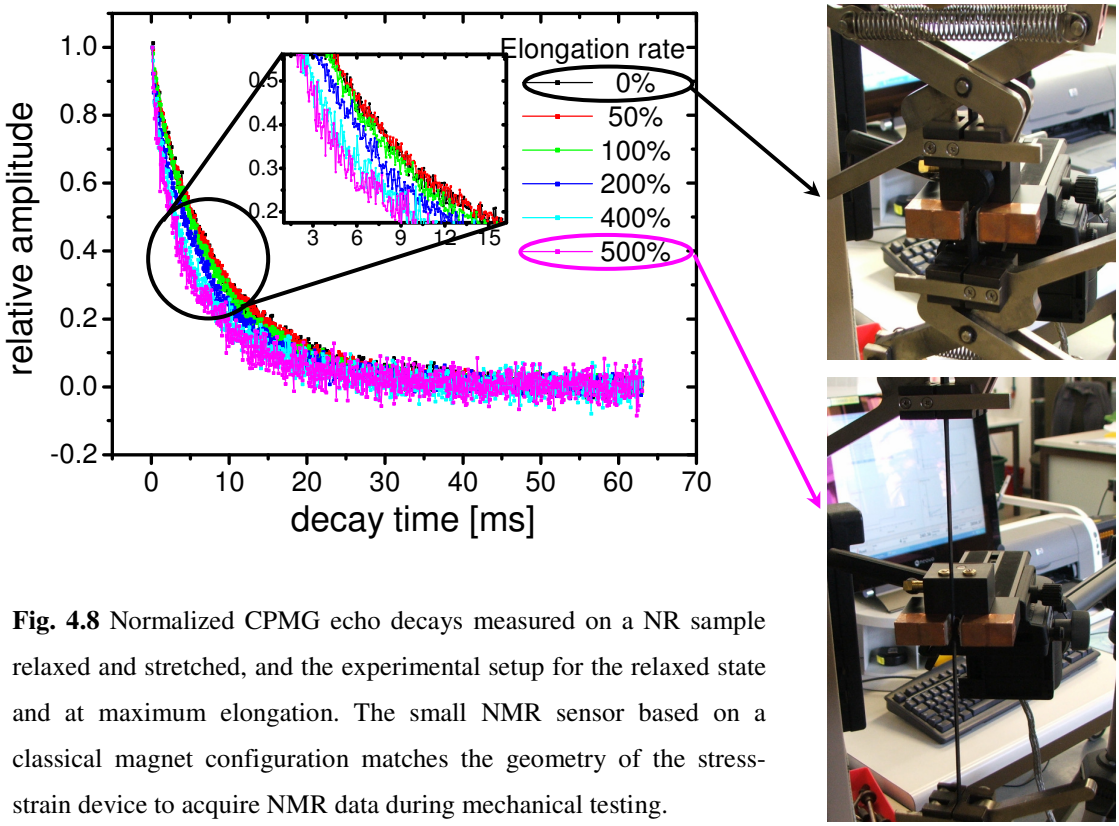

Fig. 4.8 Normalized CPMG echo decays measured on a NR sample relaxed and stretched, and the experimental setup for the relaxed state and at maximum elongation. The small NMR sensor based on a classical magnet configuration matches the geometry of the stress-strain device to acquire NMR data during mechanical testing.

Experimental

The stress-strain device could be set to stretch the sample until the desired percentage of its initial length and to hold it at any elongation as long as the NMR acquisition requires. The NMR-sensor with a special design to fit the shape and dimensions of the standard stress-strain test samples operating at the resonance frequency of 22.5 MHz was connected to a mobile preamplifier and NMR spectrometer. The special probe consists of two permanent magnets with a 4 mm wide gap inbetween. The radiofrequency (rf) coil was built from two coils in the Maxwell geometry each of them placed on the surface of a permanent magnet. During experiment the sample is fixed inside the gap of the probe and between the two windings of the rf coil (Fig. 4.8).

The stress-strain curve could be mapped simultaneously with the mechanical measurement by recording CPMG echo decay curves at different strains. The NMR sensor was always displaced in the middle of the sample. The total experimental time was 40 minutes with ca. 7 minutes per elongation step for a number of scans of 1500.

Results

As any of the exponentials showed a fitting error above the desired precision limits, another approach for the pure $T_{2\mathrm{eff}}$ weighting was necessary. The NMR echo envelopes (CPMG echo decays) have been normalized by dividing each echo train by the mean amplitude of the first twenty echoes which are predominantly encoded by the spin density. This computation eliminates the errors due to spin density variations with the strain and avoids fitting errors. Nevertheless, the sensitivity drops with increasing elongation due to decreasing amount of sample inside the sensitive volume of the sensor.

The normalized CPMG echo decays solely encoded by $T_{2\mathrm{eff}}$ can then be compared with good reproducibility. Figure 4.8 depicts the six normalized decays: for 0%, 50%, 100%, 200%, 400% and 500% elongation clearly reveal the changes in the material structure and molecular mobility with the strain. The experimental data reveal faster signal decay when the sample is stretched compared to the relaxed or less stretched states. The sample becomes more rigid as the polymer chains are higher oriented while the force necessary to elongate it increases. This variation can be quantified as a function of strain by the sum of the normalized echo amplitudes (Fig. 4.9 a).

For modeling the mechanical properties of stretched rubber test samples, the NMR data need to be converted into terms of well-known material parameters. According to this, a correlation between the stress-strain diagram and the $T_{2\mathrm{eff}}$-strain diagram could be very useful for subsequent calibrations. The inverse proportionality between the shear modulus measured in an elastomer, and the transverse relaxation time $T_{2\mathrm{eff}}$ of the deformed elastomer is already known [Lit1, Fec1]. The diagram recorded by the stress-strain device was compared with the NMR diagram representing the inverse values of the echo amplitude sums as functions of the elongation (Fig. 4.9b). The NMR–MOUSE data are in an excellent concordance with the mechanical experiment results as the NMR diagram parallels the stress-strain curve up to about 400% elongation. Such a

set-up promises to be of use for predicting the time of failure based on NMR relaxation measurements in cyclic loading tests.

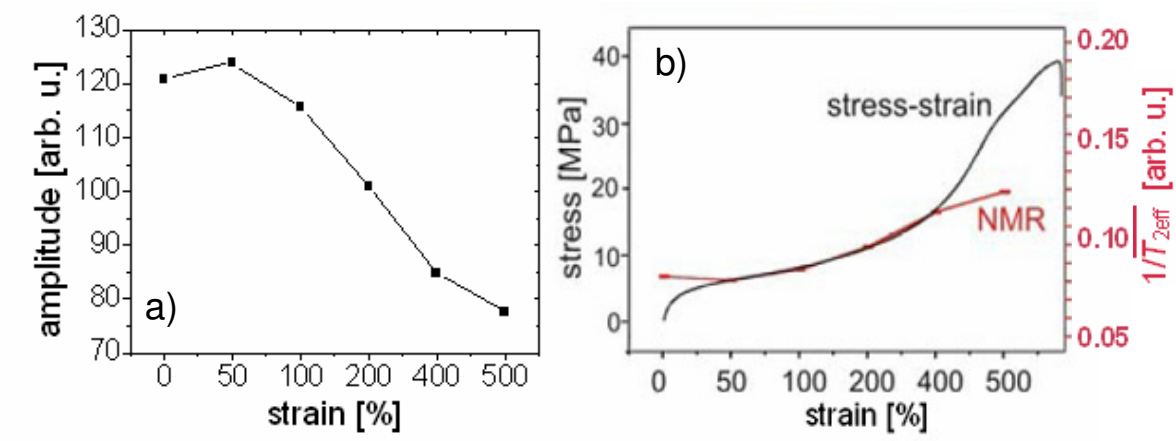

Fig. 4.9 a) Normalized CPMG echo amplitude sums versus strain [Gog2]. b) Stress-strain diagram and $1/T_{2\mathrm{eff}}$ curve for carbon black-filled natural rubber.

4.2.5 Mechanical testing versus NMR

For modeling the mechanical properties of rubber test samples, the NMR data need to be presented in terms of well-known material parameters and not in terms of NMR parameters such as $T_{2\mathrm{eff}}$. Consequently, $T_{2\mathrm{eff}}$ needs to be translated into Young's modulus of elasticity (E) or shear modulus (G). Similar correlations of $T_{2\mathrm{eff}}$ with the cross-link density and even with other parameters accessible to NMR but through much complicated experiments like the second order van Vleck moment ($\langle M_2 \rangle$) which characterize the anisotropic slow motion of the polymer chains on the mesoscopic scale, can be of great use. For this reason, a map of the E and G moduli would be an important quantity to understand heterogeneous polymers. Moreover a possibility of translating these parameters into cross-link density or second Van Vleck moment units would make the study much more powerful.

Stress distributions can be quantified via measurements of $T_{2\mathrm{eff}}$ relaxation times [Blü12]. On the molecular level, macroscopic strain changes the free volume and reduces the segmental mobility, which affects the NMR relaxation time. The transverse relaxation time T_2 becomes shorter with increasing strain for elastomers above the glass

transition temperature (T_g). The same effect upon T_{2eff} have the increasing cross-link density and consequently increasing shear modulus and second van Vleck moment [Fec1].

By measuring the relaxation time T_{2eff} in well known samples as a function of the above mentioned parameters, the latter can be assigned to similar materials non-destructively, by a simple NMR relaxometry measurement. Moreover a high-resolution T_{2eff} profile though a rubber sheet measured with a profile NMR-MOUSE can be translated in terms of moduli profiles impossible to be measured by other means.

Correlated parameters

Considerable progress has been obtained in the past in relating the structural parameters of polymer networks to the elastic properties of vulcanized rubber. The application of this type of relaxation experiments is based on the high sensitivity of the relaxation process to chain dynamics, involving spatial-scale chain motions at temperatures well above the glass transition temperature. It is well known, that the decay of the transverse magnetization of nuclear spins, induced by dipolar interactions, is an important source of information about the dynamics of polymer chains in cross-linked rubber networks in a variety of physical conditions.

From the viewpoint of NMR, elastomers above their glass-transition temperature exhibit both, solid-like and liquid-like features. Whereas the segmental motions give rise to the liquid-like behaviour, the presence of permanent or non-permanent cross-links most commonly induced by sulphur vulcanization lead to residual dipolar or quadrupolar couplings, that are responsible for the solid-like properties [Coh1]. The cross-link density C of an elastomer is directly proportional to the mechanical modulus E of elasticity

$$E = RTC = RT\rho/M_e N_e, \tag{4.7}$$

where R is the ideal gas constant, T is the temperature, and ρ is the density of the material. If the intercross-link chain is modeled by N_e freely jointed segments with molecular weight M_e, the modulus can be seen as being inversely proportional to the number of statistical segments between cross-links.

Depending on the degree of motional restrictions, the residual dipolar or quadrupolar interactions may be quite small, i.e., on the order of a few percent of those

found in rigid solids [Coh1, Col1] The stiffness of the material, which is expressed by the mechanical modulus E, directly corresponds to the average strength of the dipolar coupling between protons on an intercross-linked chain. It results from rapid but anisotropic motion which is characterized by a distribution of correlation times. This distribution can be interrogated by various NMR experiments, for example by those which measure T_2.

The cross-link density of elastomers can be monitored by transverse relaxation time measurements using the NMR MOUSE. Differences in cross-link density can be related indirectly to the molecular mobility of the polymer chains. As the dipolar coupling is large for ^{1}H, the $T_{2\mathrm{eff}}$ relaxation time, which is sensitive to slow motions, is affected by changes of the effective dipolar coupling. Therefore, $T_{2\mathrm{eff}}$ should reveal differences in cross-link densities.

Of great importance for characterization of anisotropy of chain dynamics and segmental order in polymer networks of cross-linked elastomers are the parameters of the dipolar correlation function (DCF) obtained from the mixed echo decays [Fec1]. The mixed echo refocuses the homogeneous and inhomogeneous spin interactions. It allows the investigation of the fluctuation of the dipolar interaction of polymer chains in the slow motional regime.

A model involving the distribution of correlation times can be used to fit the mixed echo decay [Fec1]. The method takes into account the multi-spin dipolar interactions and eliminates the interference of linear spin interactions due to chemical shielding, magnetic field inhomogeneities, local susceptibility variations, and hetero-nuclear dipolar interactions. For ideal polymer chains, the most significant and distinctive property is the Gaussian distribution of the end-to-end distances. By considering the different segments of the freely jointed chain which are statistically independent and can be represented by a Markov chain, one can derive the correction to the Gaussian distribution of the end-to end distances (see Appendix). Using the corrected Gaussian distribution function one than gets:

$$\langle M_2 \rangle \propto \frac{5}{3}\frac{1}{N^2} - \frac{2}{3}\frac{1}{N^3}. \tag{4.8}$$

Within the limit of the approximation used, it is concluded that the residual second van Vleck moment scales with $1/N^2$ for high numbers of statistical segments, i.e., for N ? 1,

which means for low cross-link densities, a regime which is not valid for all cross-linked natural rubber formulations investigated using DCF [Fec1] and later by NMR relaxometry. The effective number N of statistical segments is defined by the number $N^{(0)}$of segments between physical cross-links or topological constraints and the number $N^{(C)}$ of segments between chemical cross-links. If we assume that the contributions to the residual dipolar coupling are additive and topological constraints are independent of the degree of chemical cross-linking, we can write $(N)^{-1}$? $(N^{(0)})^{-1}+(N^{(C)})^{-1}$. In this case, one expects (cf. Eq. 4.8) that $\langle M_2 \rangle$ has a polynomial dependence on cross-link density or shear modulus. Based on the dependence of the residual second moment on $1/N$ given by Eq. 4.8, the measured $\langle M_2 \rangle$ values can be fitted by a polynomial up to the forth power in the shear modulus G, ie,

$$\langle M_2 \rangle = a_0 - a_1 G + a_2 G^2 - a_3 G^3 + a_4 G^4. \tag{4.9}$$

If only the first four values of $\langle M_2 \rangle$ corresponding to an intermediate regime of cross-linking are considered, the G_2 term dominates the dependence as it is expected from a Gaussian distribution of end-to-end vectors. With this assumption, the model became relatively simple, however, it has been shown [Fec1] that the distribution function of correlation times which describes the slow motion of the network chains scale with the cross-link density in a much more complex manner. The development of NMR methods that allow accurate measurements of residual second van Vleck moments and distributions of correlation times yields new tools to test polymer network theories that are more sophisticated than the theory of the freely jointed chain corresponding to a Markov chain.

Samples

The investigated elastomer samples are from commercially available natural rubber SMR 10 (Malaysia). The additives were 3 phr ZnO and 2phr stearic acid. The sulfur and accelerator contents were 1:1 from 1 phr to 7 phr. The accelerator was of the standard sulfenamide type (TBBS, benzothyazil-2-*tert*-butyl-sulfenamyde). After mixing the compounds in a laboratory mixer at 50^0 C, the samples were vulcanized at 160^0 C in a Monsanto MDR-2000-E vulcameter. The degree of cross-linking was measured by the

low frequency shear modulus or torque G at a temperature of 160^0 C in the vulcameter directly after vulcanization. The measurements were performed with oscillation amplitude of ± 0.5^0 and a frequency of 1.67 Hz. The stress-strain curves measured at room temperature at a strain velocity of 3 mm/min ranged between 1-15% strains.

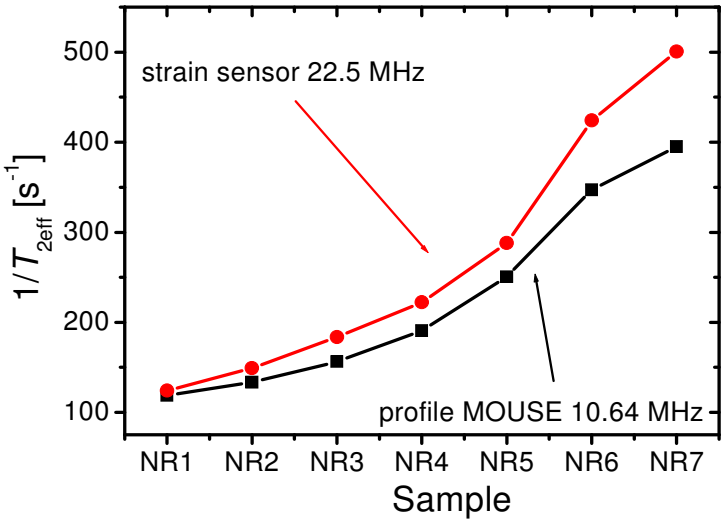

Fig. 4.10 T_{2eff}^{-1} versus cross-link density measured under the same experimental conditions with two different single-sided NMR sensors. The higher polarizing field is characterized by stronger field gradients and consequently faster decay of the transverse magnetization.

Correlations of parameters

The changes in transverse magnetization relaxation and ^{1}H residual dipolar couplings can be correlated with the polymer chain stiffness. The chain stiffness variations due to strain, fatigue, aging, etc can be quantified by NMR relaxation times. To convert T_{2eff} into terms of chain stiffness or Young's modulus of elasticity, a good correlation between the NMR data and the macroscopic values should be established and the calibration curves should be drawn. The aim of this study was to generate cross-link density maps of E and G moduli for known elastomer samples and to calibrate the ^{1}H residual second order van Vleck moments [Fec1] on the same series of NR samples. Other plots i.e., cross-link density versus shear and Young's moduli or versus second van Vleck moments have already been reported [Fec1]. Consequently, the above mentioned parameters will be studied in the following only as functions of the effective transverse magnetization relaxation measured with a single-sided NMR sensor. At the

end of this study, the whole set of parameters which apparently seem to be achievable exclusively trough destructive methods, will turn out to be accessible trough a non-destructive investigation method by means of a low-cost mobile sensor as well.

One-sided NMR sensors with different configurations and magnetic field strengths were tested for this purpose. When doing such a study, one must not forget that each sensor is unique from the point of view of the magnetic field profiles. Thus a parameter map built by the aid of a given sensor is valid only for that sensor (see Fig. 4.10) and exclusive at the temperature at which the calibration has been done. Nevertheless, considering a linear variation of $T_{2\mathrm{eff}}$ with the temperature, and knowing the change in the field profiles with the magnet temperature in a given range, extrapolations to any temperature in the considered regime can be done.

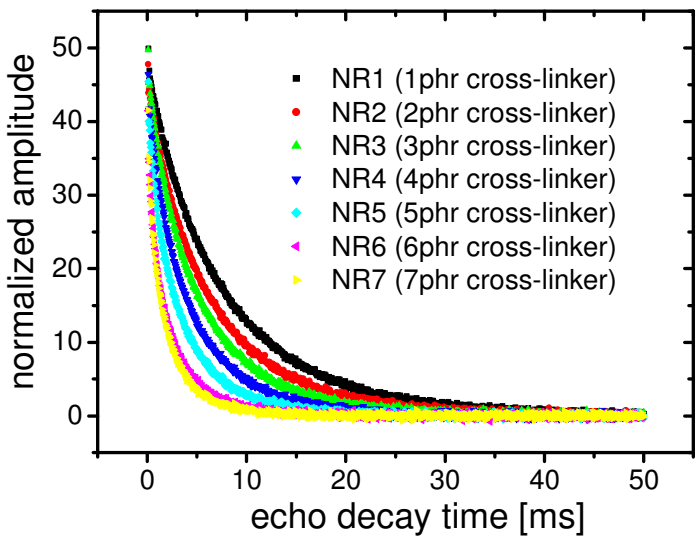

Fig. 4.11 Normalized CPMG echo decays for vulcanized natural rubber samples with 1 phr to 7 phr content of sulfur.

The decays of the mixed ^{1}H echo represented by a combination of the magic and the Hahn echoes were previously reported for a series of cross-linked elastomers [Fec1]. The multi-spin dipolar correlation functions characterizing the mixed echo decays were derived in the approximation of a distribution of correlation times. Based on these dipolar correlation functions the ^{1}H residual second van Vleck moment was determined for the series of natural rubber samples with different cross-link densities. The transverse relaxation times have been measured for the same series of carbon-filled NR samples

using an NMR-MOUSE operating at the resonance frequency of 17.23 MHz for protons. The *G* and *E* moduli have been measured by conventional methods [Fec1] with a reproducibility of the results corresponding to the homogeneity of the samples.

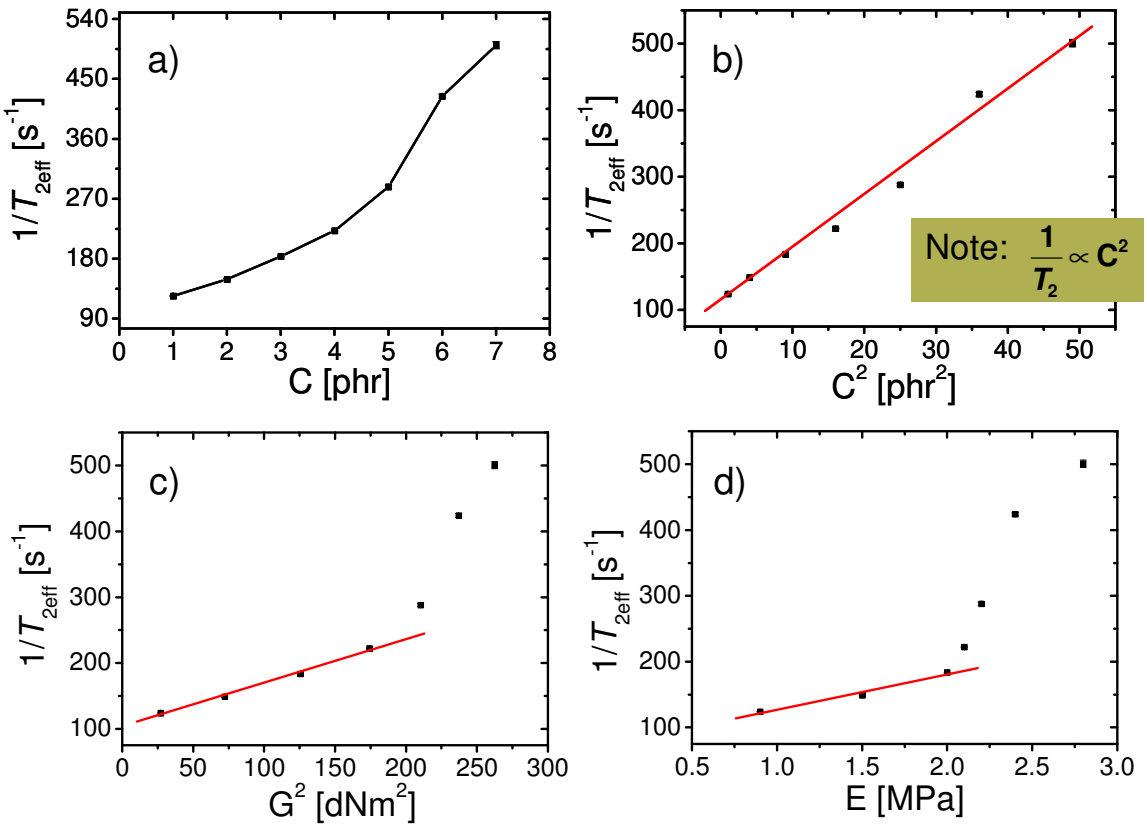

Fig. 4.12 a) $1/T_{2eff}$ measured with the NMR-MOUSE as function of the cross-link density. b) $1/T_{2eff}$ versus C^2; according to the theory, for small cross-link densities, the dependence should be linear, which is experimentally observed even at high cross-link densities; c) The variation of $1/T_{2eff}$ as a function of the square shear modulus G^2. Up to a sulfur content of 4 phr the dependence is linear revealing the ease of calibration of the two parameters in this interval; d) $1/T_{2eff}$ versus Young modulus. The linearity is present up to a sulfur content of 3 phr.

A first comparison between samples was done in terms of the normalized CPMG echo decays. As expected, the NMR echo envelopes decay faster for higher cross-link densities (Fig. 4.11). The higher the cross-link density, the higher is the chain stiffness. Since dipole-dipole interactions are the main reason for relaxation in most polymers, it can be shown that the NMR relaxation times depend on the motion of the nuclei as characterized by a correlation time. Thus, the consequences of the increasing cross-link density due to increasing cross-linker concentration are the increasing residual dipolar

couplings and correlation times that can be translated into shorter NMR relaxation times. The $T_{2\text{eff}}$ obtained from mono-exponential fits of the echo decay envelopes have been analyzed as functions of the cross-link density C (Fig. 4.12a and b). $1/T_{2\text{eff}}$ increases with increasing cross-link density. The dependence is not linear, although the two parameters follow the same trend. Thus we can say that the increase of $1/T_{2\text{eff}}$ with increasing C is monotonous. Nevertheless, following the calibration curve, (Fig. 4.12a) the cross-linker amount of an unknown sample can be easily determined by a simple NMR relaxometry experiment with the specification that the probe (NMR frequency and field gradients) must be the same.

The theory of ideal chain networks predicts a quadratic dependence in G of the residual dipolar couplings [Fec1]. Knowing the theoretical relationship between $T_{2\text{eff}}$ and G, which, following the theory is directly proportional to the cross-link density, $1/T_{2\text{eff}}$ has been also studied as a function of the square of the cross-linker concentration, C^2 (Fig. 4.12b). The linearity was verified proving a good concordance between the theoretical prediction and the experimental behavior even at high cross-link densities.

In a subsequent the NMR relaxation data were correlated with the Young`s and shear moduli, E and G respectively. $1/T_{2\text{eff}}$ linearly increases with G^2 for low cross-link densities (up to 4 phr) (Fig. 4.12c). For a higher degree of chain stiffness the ideal case linearity is not verified. But, it was previously shown that in real elastomers due to a violation of the Gaussian approximation for the end-to-end vector, this dependence can be described as a polynomial in G [Fec1]. Thus, some deviations of $1/T_{2\text{eff}}$ from a linear dependence in G^2 can be attributed to this effect. The same happens while correlating E with the inverse of the transverse magnetization relaxation. Like in the previous plot, the linearity of $1/T_{2\text{eff}}$ versus E is verified only for low cross-link densities (Fig. 4.12d). Above 4 phr sulfur content an exact calibration of parameters is more difficult to be done.

Because of the quadratic dependence in G of the residual dipolar couplings, the residual second order van Vleck moment varies like G^2. This aspect requires an analysis of $1/T_{2\text{eff}}$ as a function of $\langle M_2 \rangle$. As in the plot which correlates $1/T_{2\text{eff}}$ to C^2 the theoretical linearity of the diagram representing $1/T_{2\text{eff}}$ as a function of $\langle M_2 \rangle$, was experimentally verified (Fig. 4.13). The small fluctuations of the data points around the fit line are the consequence of the impossibility to prepare an ideal cross-linked polymer

chain network according to the theory and also of the experimental and fit errors. Nevertheless the plot can be used with good precision for calibrations of experimental values.

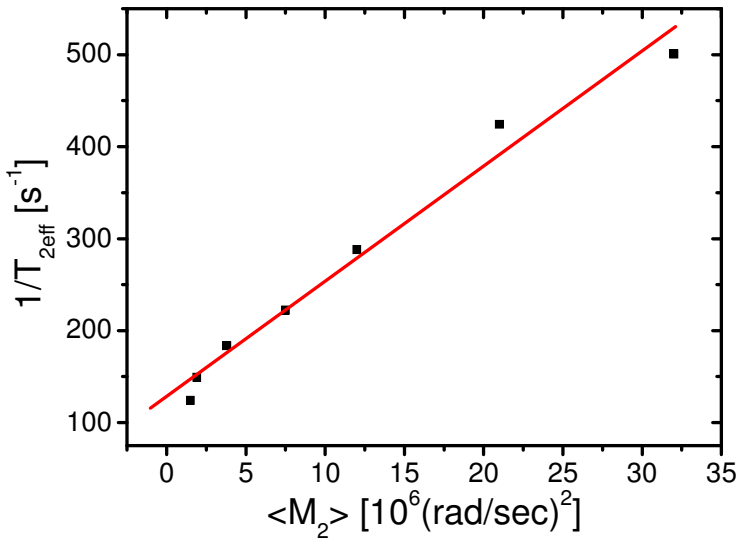

Fig. 4.13 $1/T_{2eff}$ profile as a function of the second order van Vleck moment. The linearity requested by theory is experimentally verified even at high cross-link densities.

4.3 Single-sided NMR imaging

In the last years, special efforts have been spent to achieve spatial localization with single-sided systems. The implementation of three-dimensional imaging techniques on such sensors converts the tool in a truly non-invasive open tomograph useful to resolve the structure of arbitrary large samples. Many new examples demonstrate the potential of single-sided sensors to assist in the design of materials with improved properties and these will be the topic of this subsection.

4.3.1 Method

The NMR-MOUSE was initially intended to scan the surface of large objects by repositioning the device with a lateral resolution defined by the size of the rf coil.

Although the use of a smaller coil improves the lateral resolution, it is at the expense of the maximum penetration depth. Thus, in practice, only a coarse resolution of the order of a centimeter can be achieved. To resolve finer structures inside the sensitive volume, Fourier imaging based on pulsed gradients has been implemented [Pra1, Cas2]. This approach required the optimization of the magnet geometry to improve the static gradient uniformity, the design of the single-sided gradient coils, and the development of an imaging technique which is suitable to such grossly inhomogeneous fields. The strategy to produce three-dimensional (3D) images takes advantage of the static gradient to achieve slice selection at different depth inside the sample. Once a slice at a given depth is excited, 2D phase encoding, which requires the generation of two perpendicular pulsed gradients, is used to achieve lateral resolution [Pra2, Per2]. Besides the important hardware improvement accomplished in the last years, a determining issue to put this method to work was the development of a multiecho acquisition scheme which affords the reduction of the experimental time by up to two orders of magnitude [Per2, Cas3]. This new imaging sequence offers the possibility to produce contrast in the image in a simple way either by T_1 or T_2, or by molecular self-diffusion.

The open tomograph

To retrieve 3D spatial localization by combining 2D images of a number of slices selected at different depths, the method requires a static magnetic field with a uniform gradient perpendicular to the surface of the sensor. As the static field generated by the first magnet geometries did not fulfill this condition, a magnet based on a U-shaped geometry (Fig. 4.14) was optimized by including a number of magnet blocks that allowed modifying the spatial dependence of the field to generate flat slices of constant frequency perpendicular to the depth direction *y*. Due to the finite dimensions of the magnet, the flatness of the slices depend on the lateral dimension of the excited volume along both *x*- and *z*- directions. For this design a deviation smaller than half a millimeter is obtained when working inside a lateral field-of-view (FOV) of 40 by 30 mm, which is selected by a 40 mm squared rf coil [Per2]. The sensor surface is defined by the position of the rf coil, which is located at 30 mm above the surface of the magnet. At this position, the resonance frequency is 8.35 MHz and the field possesses a constant gradient along *y* of about 2.5 T/m. The probe allows manual tuning between 8.35 MHz

and 7.35 MHz covering a depth range of 10 mm. Finally, the gradient coil system built to provide two perpendicular pulsed gradients along the *x*- and *z*- axes was positioned inside the gap between the magnets and underneath the rf coil (Fig. 4.14).

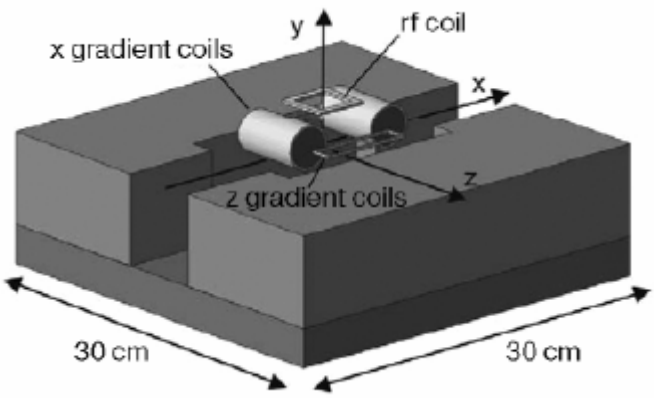

Fig. 4.14 U-shaped magnet for imaging – an open NMR Tomograph. This geometry produces a static field with a main component along *z*. Two solenoids 34 mm diameter, 54 mm long and separated by 74 mm from center to center generate G_x, while two rectangular coils 17 by 70 mm^2, separated by 75 mm from center to center, provide G_z. Both gradient coil pairs are placed with their centers at 10 mm from the magnet surface. The 40 mm square rf coil is positioned at 30 mm above the magnet. The origin of the coordinate system is on the upper side in the center of the magnet.

Imaging sequence

To achieve spatial resolution in the presence of the static gradient, a pure phase encoding method was implemented in combination with a Hahn echo sequence [Pra1]. In this way the phase spread introduced by the static gradient is refocused, while the gradient pulses applied during the evolution intervals encode positions in the phase of the echo signal (encoding period in Fig. 4.15). This technique was originally implemented to achieve 1D and later 2D spatial resolution, but the poor sensitivity imposed by the large bandwidth of the signal acquired in the presence of such a strong gradient led to impractical unfeasibly long acquisition times [Pra1, Cas2].

The basic idea to speed up data acquisition is based on the fact that the echo time t_{EE} used for the Hahn echo sequence is usually much shorter than T_2 of the sample, and a train of echoes can be generated by applying a Carr-Purcell-Meibum-Gill (CPMG) sequence. The echoes of the train can be than coadded in order to increase sensitivity

during detection, leading to a reduction of the experimental time by roughly a factor proportional to the number of echoes acquired. However, the extension from a single- to a multiecho imaging was not straightforward because the phase encoded by the gradient pulses is lost after a few echoes due to the off-resonance excitation. The solution is based on the fact that, even while off-resonance, a train of refocusing pulses preserves one of the components of the signal without distortions. The final sequence combines two experiments, a first one with refocusing pulses applied with phase *x* (CP) is used to sample one of the quadrature channels, while the second one with refocusing pulses with phase *y* (CPMG) is used to sample the second channel. The CP and CPMG channels are later combined to build the complex *k*-space signal [Per2]. The maximum sensitivity improvement is obtained when the echoes of the entire echo train are co-added. The full addition is used in cases where uniform T_2 or $T_{2\mathrm{eff}}$ (decay during the CPMG sequence) but different densities are expected across the sample.

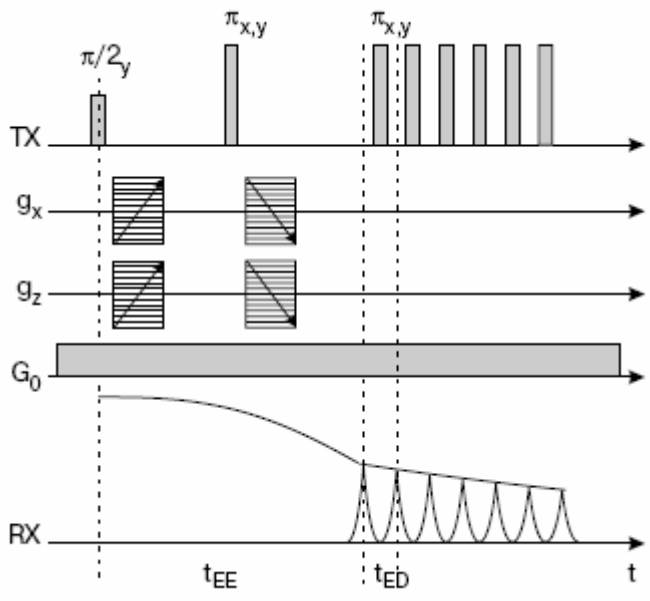

Fig. 4.15. CP plus CPMG multiecho sequence applied to sample the complete echo decay train. To reduce signal attenuation during the encoding period, gradient pulses are applied simultaneously along each direction and in both free evolution periods of the Hahn echo sequence. The shortest t_{EE} is determined by the length of the gradient pulses plus a stabilisation time during which the gradient pulse goes to zero. To maximize the number of echoes that can be generated during the detection period, the echo time is reduced after the formation of the first echo. The detection echo time t_{ED} is determined by the dead time of the probe.

When $T_{2\mathrm{eff}}$ changes with position across the sample, the contrast between different structures can be enhanced by adding different echoes of the decay before reconstructing the image. Moreover, there are cases where different regions in the sample possess similar $T_{2\mathrm{eff}}$, but a different T_2 (decay during the Hahn echo sequence). In this case the encoding time t_{EE} in the multi-pulse imaging sequence can be increased to enhance the contrast between these regions.

4.3.2 Imaging of polymers and biological materials

Polymer morphology and defects

Materials with heterogeneous morphology can be investigated by simple NMR imaging techniques which translate the physical heterogeneity into spin density contrast. However, this turns out often to be of little relevance for materials which can provide strong T_1, T_2 or $T_{2\mathrm{eff}}$ contrasts instead. To achieve high sensitivity in reasonable experimental times, the multi-echo sequence (Fig 4.15) supposes a combination of all these contrast parameters.

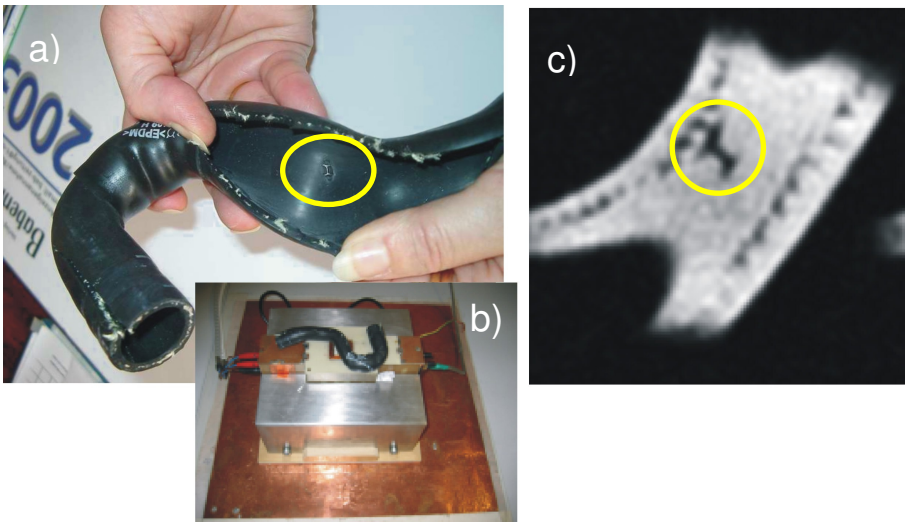

Fig. 4.16 Imaging of a defect in the rubber hose. a) Photo showing the failure originated in the production of a textile-reinforced rubber hose. b) Experimental setup – unilateral NMR tomograph with the sample in place. c) Cross section obtained with the open tomograph at 4 mm inside the tube wall. The FOV was 4 by 4 cm^2, the lateral spatial resolution of $(0.8\ mm)^2$, the slice thickness of 0.66 mm, and the imaging time was 120 min.

Usually $T_{2\mathrm{eff}}$ weighted spin-density images are obtained with the open tomograph by adding many echoes in the CPMG decay. An example where the echo train is completely added to achieve the maximum sensitivity improvement is failure detection in a rubber hose employed in cars for cooling of the engine (Fig. 4.16a)[Blü17]. Since it works at high temperature and under high pressure, a layer of textile fibers is incorporated to reinforce the mechanical stability of the tube.

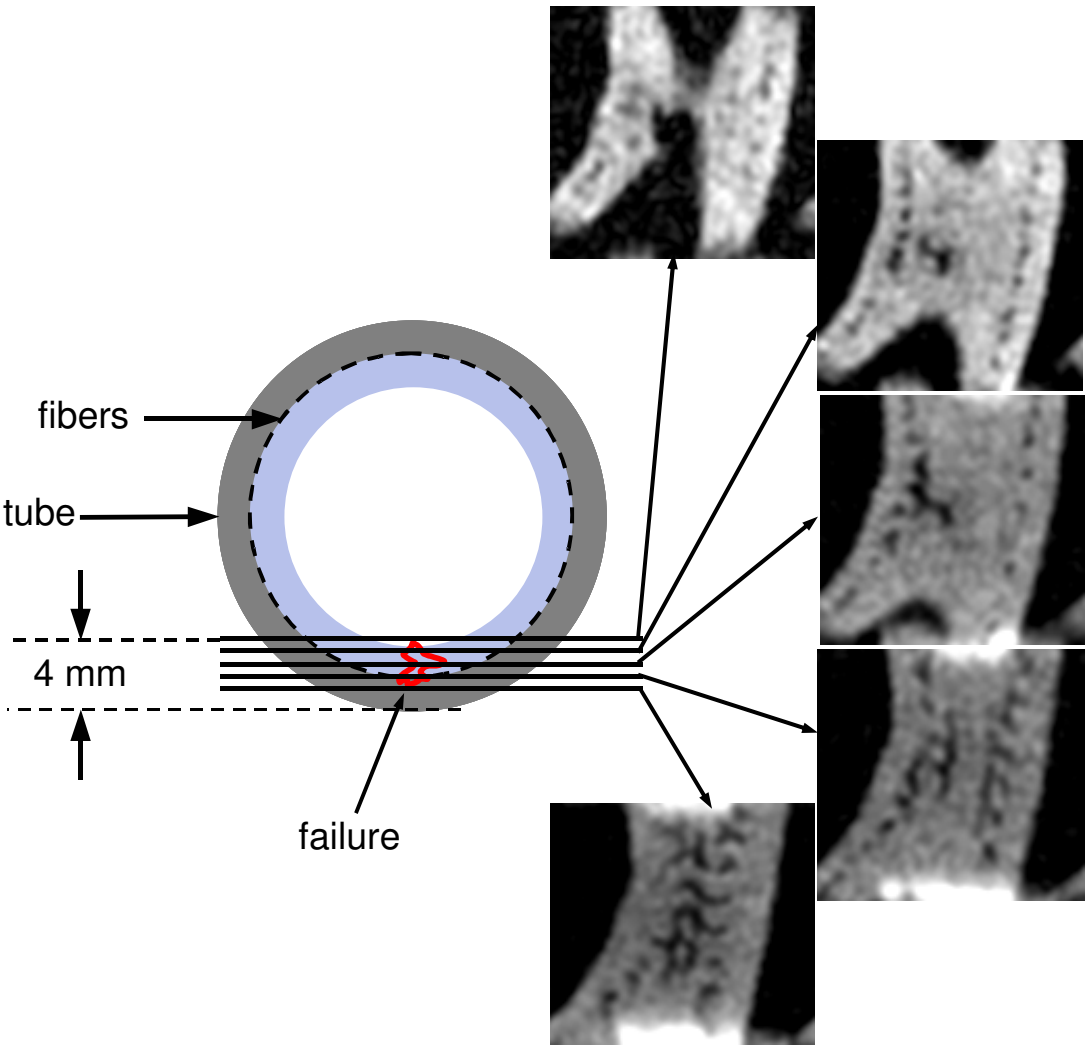

Fig. 4.17 Progressive two-dimensional 2D slices acquired step by step, from inside (up) to outside (down) in a textile-reinforced rubber hose with a defect inside, giving a 3D spatial impression of the investigated structures.

Different kind of failure may appear during the fabrication process. For example, the cross-link density may differ along the wall, bubbles may form, and the fibers may

improperly be aligned. Figure 4.16c shows a cross section of a slice selected at 4 mm depth inside the wall. The defect generated in the rubber matrix by a bubble, can clearly be observed as a dark region with an "H" shape in the image, which corresponds to the crossing point of three fibers. Using the slice selection obtained by selective excitation in the linear region of $\boldsymbol{B}_{0y}$ it is possible to follow non-destructively and without distortions the shape of the bubble with depth in a 3D view (Fig 4.17). At the same time, information about the internal distribution order of the reinforced fibers inside the rubber hose is obtained. Only 16 scans were used leading to a total experimental time of 3 h for the whole 2D image set. The first image was obtained close to the internal surface inside the rubber tube. The contour of a defect inside the tube already appears at this position. In the second image this defect is more obvious. At this position, the shape of the hole which looks like an "H" can be observed. From the next images one can follow the three-dimensional shape of the failure which is not regular. In the last image, the hole appears just as an inhomogeneity of the rubber tube. The two parallel lines of reinforcement fibers become closer in the last sections. This detail shows that the tube was scanned going in steps from inside to outside.

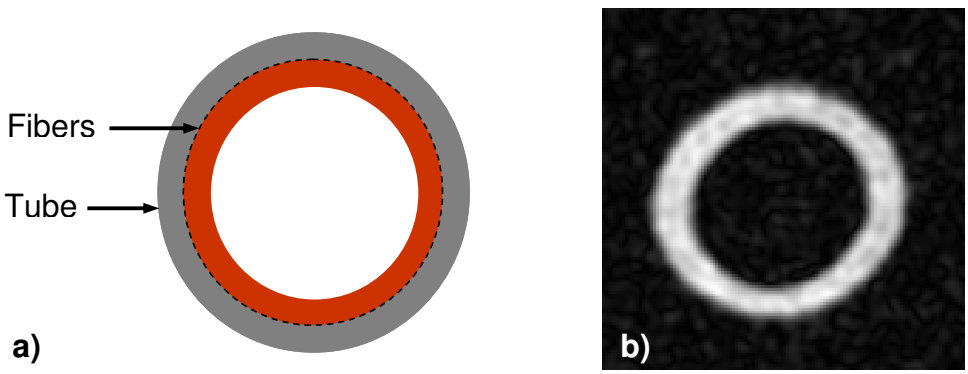

Fig. 4.18 Schematic representation of a cross-section trough a textile-reinforced rubber hose employed in cars. Two layers of rubber can be distinguished with the textile reinforcement in-between. b) Cross-sectional NMR image of the rubber hose.

The rubber hose was imaged in another position with no visible failures to investigate the distribution of fibers. The image was obtained using 64 scans in an experimental time of ca. 2h. Figure 4.18b depicts the cross sectional NMR image of the object. It reveals no heterogeneities excepting the textile layer appearing as a dark ring

in the middle separating the inner layer of the hose from the outer one. Figure 4.18a is a schematic representation of the tube reconstructed on the base of the NMR image. It contains two polymer layers with the fibers in-between.

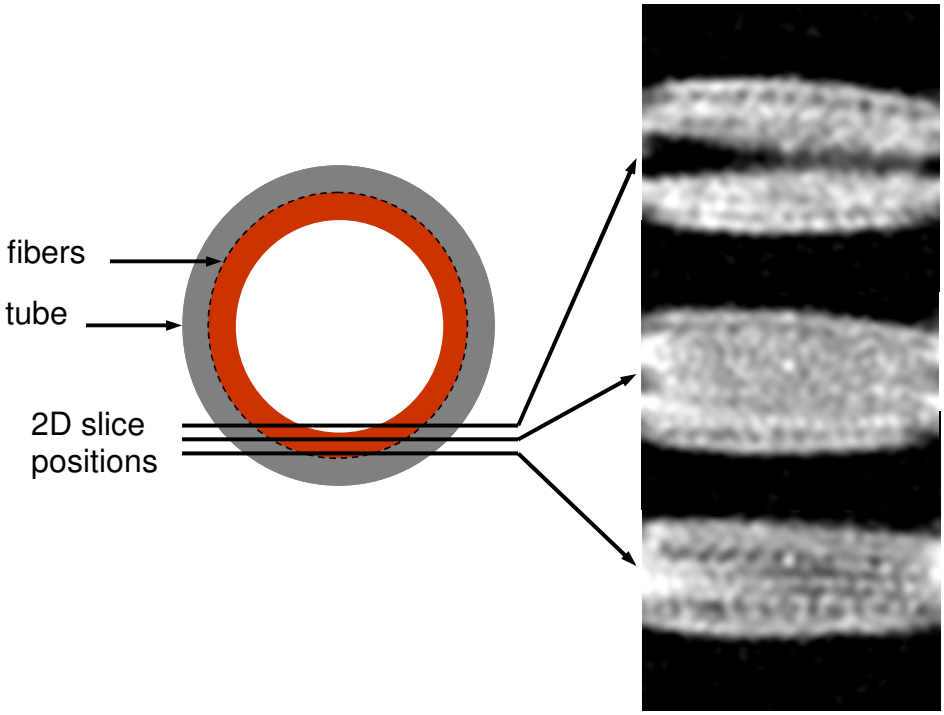

Fig. 4.19 Schematic representation of the rubber tube and its 2D NMR images measured with the unilateral NMR tomograph in the marked positions. The dark traces in the images correspond to the reinforcement fibres and are most intense in the middle of the tube wall (bottom) namely in the crossing point of the two fibre layers, longitudinal and circular.

Other sections in a perpendicular plane to the cross-section plane reveal the disposition of the longitudinal fibers along the rubber tube (Fig. 4.19). The fiber distribution can be followed step by step with the depth by the slice-selective method. The fibers appear in the image as parallel dark lines drawn along the tube. The first image was acquired at a position close to the inner surface of the tube. Two symmetric fiber lines are most obvious here. There are two other lines which are less clear as their positions are shifted below the plane of the 2D section. The next two images obtained at different positions are similar. The final image shows an increased fiber density as it was acquired at halfway through the tube wall at the position between the two rubber layers

which build up the tube. Here the textile fibers appear as woven in a lattice. No defect of the material can be observed in these images. The distribution of reinforcement fibers is also regular.

Biological structures

NMR imaging finds most of its applications in medical diagnostics of humans and pathology studies of animal models [Man2, Cal1, Blü1, Haa1, Vla1, Blü7]. The success of the method is based on the non-invasiveness of nuclear magnetic resonance and the unsurpassed soft matter contrast, which is hard to achieve with competitive methods like X-ray or computer tomography.

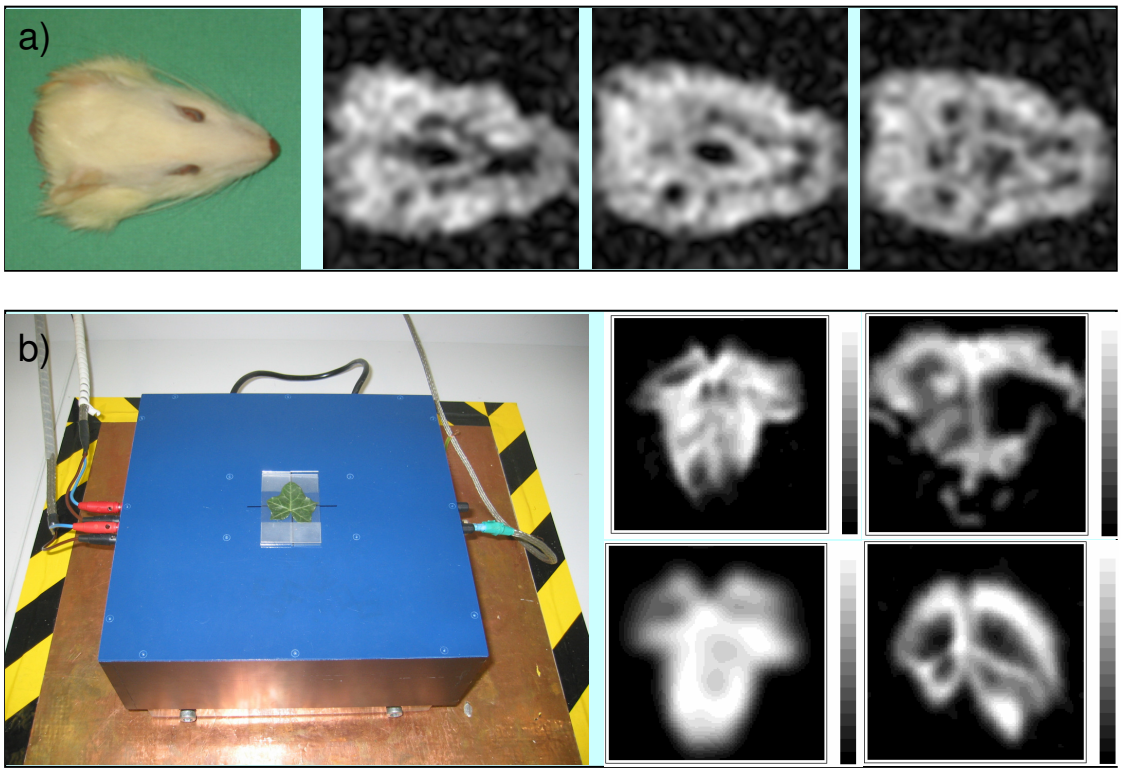

Fig. 4.20 a) The head of a rat in vitro and its corresponding 2D profiles measured with the unilateral NMR tomograph. The acquisition time of one image was ca. 30 minutes for a field of view of 4 cm x 4 cm. The planar resolution of each image is 0.8 mm^2. b) Imaging of plant leaves in vitro. The sensitivity of the single-sided sensor is excellent even for such thin samples.

A promising application of a mobile low-cost single-sided tomograph is diagnostic imaging of bones and joints with potentially important applications in the

maxilo-facial surgery [Gog2]. The multi-echo imaging sequence was implemented to produce cross-sections trough a rat *mandibula* in vitro. For data analysis, the entire echo trains were evaluated, so that a voxel with the tissue having long relaxation time and a high proton density appears bright in the image, while the hard structures like the bone and teeth appear dark. A set of 2D profiles of the *mandibula* was acquired at different positions by changing the relative position of the sample with respect to the probe. The images (Fig. 4.20a) reveal the *mandibula* morphology at each position of the slice with a T_2-weighted spin density contrast. The maximum planar resolution was 0.8 x 0.8 mm^2. The measurement time was ca. 30 minutes for a field of view of 4 x 4 cm^2. The teeth as well as the bone structures can be easily discriminated in the images.

Another interesting application is to implement the method for studying plants. To have access to functional information in plants, a much more complicated setup would be necessary. Even so, the experiment would last too long because of the slow processes under study. Nevertheless, one may have access to morphological information trough imaging techniques non-destructively as we deal with living entities.

The same setup as for imaging the rat *mandibula* was used to image plant leaves in vitro (Fig 4.20b) with the specification that doing the same process in vivo requires no supplementary effort. The portability of the sensor makes it possible to bring the experimental hardware to the living plant. This is one of the special cases when the sensitive volume is thicker than the sample and in consequence good sensitivity is required. The unilateral NMR tomograph provides sufficient flatness of the $\boldsymbol{B}_0$ isosurface in the *xz* plane and excellent sensitivity for imaging such thin samples. In both biological applications, the spatial resolution still cannot compete with other microscopic methods, but the great advantages like the portability of the device, and the low costs of the method can be good reasons for a potential use of the unilateral NMR imaging for biomedical or botanical analysis.

Contrast induced by network strain

The possibility to produce relaxation contrast enables one to spatially resolve physical parameters that influence the relaxation times. It has been observed before, for example, that the relaxation time of polymers change under stretching [Hai1, Gog2]. However,

one should be aware that T_2 and $T_{2\mathrm{eff}}$ are usually encoded by different molecular parameters.

When regions with different $T_{2\mathrm{eff}}$ need to be discriminated, the contrast between them can be enhanced by judiciously adding different echoes of the echo train before reconstructing the image. In this way, a density image can be obtained by adding the first echoes of the train, while a strong $T_{2\mathrm{eff}}$ contrasted image is achieved by adding the last echoes.

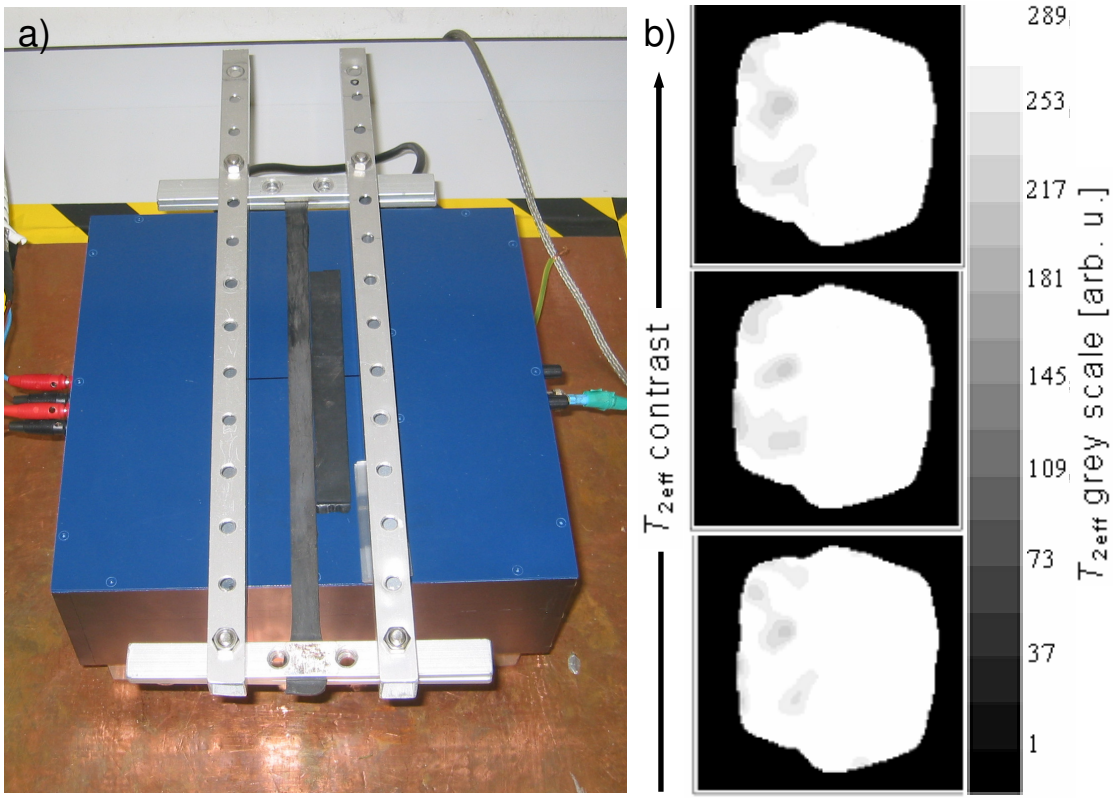

Fig. 4.21 a) Experimental setup showing two cross-linked natural rubber bands, elongated (left) and not-elongated (right) to be imaged on the unilateral tomograph. b) Set of three images obtained from the same experimental data using different $T_{2\mathrm{eff}}$ contrasts. Moving from bottom to top the contrast is progressively increased by adding 10, 20, and 30 echoes respectively in the CPMC train. The $T_{2\mathrm{eff}}$ contrast is displayed by an arbitrary grey scale where $T_{2\mathrm{eff}}$ decreases from white to black.

Figure 4.21a depicts the experimental setup for imaging the heterogeneity induced by strain in a NR band. For comparison a relaxed NR sample was placed next to the elongated one. The images of the adjoining rubber bands (stretched – left and not stretched – right) shown in Fig. 4.21b were reconstructed from the same experiment by

adding different parts of the acquired echo trains. The bottom image possesses a low T_{2eff} weight, while in the following two images the T_{2eff} contrast is progressively enhanced to differentiate between the elongated sample with short T_{2eff} and the relaxed one with longer T_{2eff}. Some slight dark spots corresponding to regions with low T_{2eff} can be identified in the elongated sample. Moreover these spots increase in size with growing T_{2eff} contrast. However the contrast between the two samples remains weak.

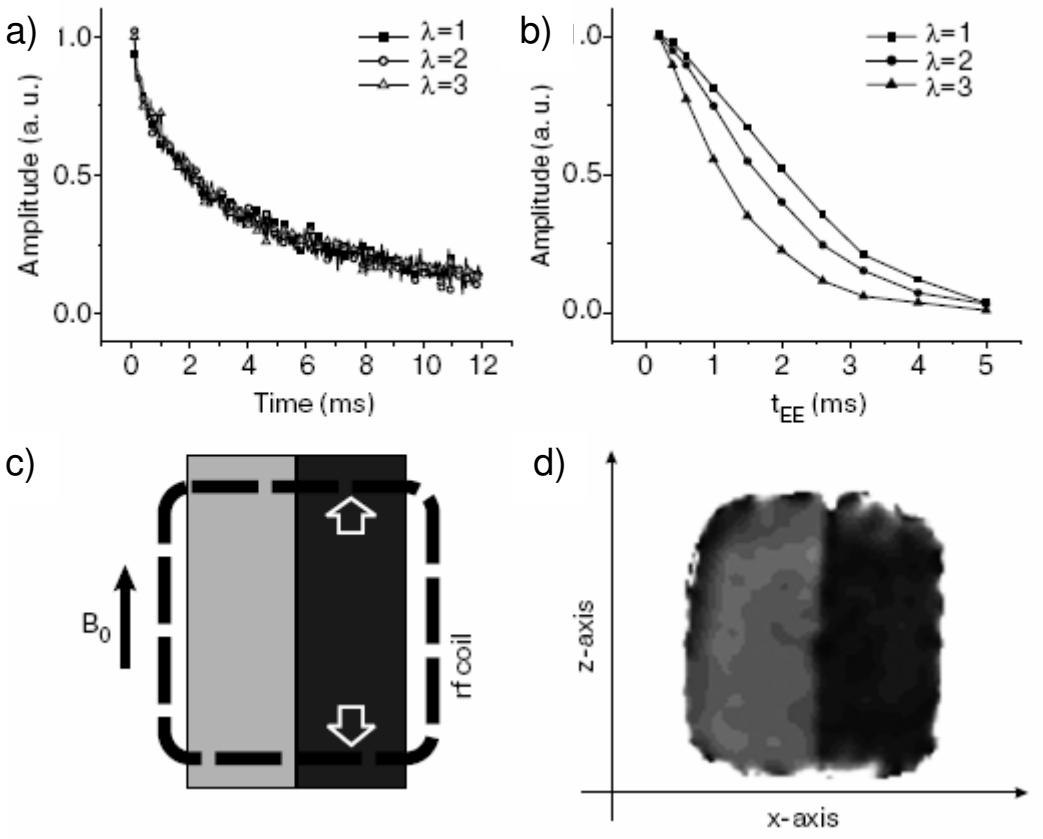

Fig. 4.22 CPMG a) and Hahn echo b) decays for different elongation ratios λ (where $l = \lambda l_0$, with l the length under stretching, and l_0 is the initial length). The maximum discrimination is observed in the Hahn echo decays. c) Scheme of the test sample. It consists of two rubber bands, one stretched to λ = 3 (dark) and the second not stretched (bright). d) Map obtained as the ratio between an image measured for t_{EE} = 1.5 ms to an image measured for t_{EE} = 0.5 ms.

This is a typical case when the variation of T_{2eff} is irrelevant (Fig. 4.22a) but still a strong contrast is observed in the Hahn echo decays (Fig. 4.22b). The contrast in this case is produced by varying the encoding time t_{EE}, while all echoes of the multiecho

trains are co-added for maximum sensitivity. By choosing a long enough encoding time, the strain can be directly measured from the pixel intensity. Obviously, this method involves $\boldsymbol{B}_1$ inhomogeneity artifacts as well as spin density artifacts across the slice. A way to eliminate these distortions requires the normalization of two images acquired for long and short encoding times. The short t_{EE} (0.5 ms) is limited by the minimum length of the gradient pulses, and the long (1.5 ms) is set to maximize the discrimination. The local strain then can be measured by converting the intensity of the map via the calibration curve.

Figure 4.22c shows a drawing of the sample composed, as in the previous experiment, of two 10 mm wide rubber bands placed next to each other parallel to $\boldsymbol{B}_0$ (z-axis). Figure 4.22d shows a map measured with a 30 mm FOV along both directions (along z the maximum FOV is limited by the rf coil to 25 mm). The image shows good T_2 contrast between the elongated (dark) and relaxed (bright) regions. Although in this experiment a uniform stretching direction is enforced, the technique can be applied to discriminate different orientations via the dependence of T_2 on the orientation of the elongation direction with respect to the direction of the polarizing field $\boldsymbol{B}_0$. Such experiment would require a set of images measured for different orientations of the object, and would provide not only the degree of stretching but also the direction thereof.

4.4 High resolution NMR profiling

It is possible to use the NMR-MOUSE in a few different ways. One of the strategies is to measure the volume-averaged properties of a sample in the sensitive volume of the sensor as was done in subsection 4.2. Another strategy is to encode space by phase or frequency in order to achieve 2D spatial resolution. In this case the 2D technique can be converted into a discrete 3D imaging technique making use of the natural gradient of the sensor. However, the slice selection performances of a conventional NMR tomograph, i.e. the one presented in subsection 4.3, are limited to at best half a millimeter.

In many cases in practice one finds that the structure of the sample under study changes only along the depth direction. Thus, a very interesting strategy is tuning the NMR-MOUSE for selection of less than 0.1 mm thin slices inside a sample. This

requires a strong and highly uniform static gradient. This profiling technique quickly found important applications in resolving multilayer structures, where even dynamic processes happening at the surface of the sample as a consequence of an exposure to the environment can be followed in real time. A short description of the technique followed by some important applications is the topic of this subsection.

4.4.1 Method

In cases where the structure of the object varies only along depth, 1D spatial resolution is sufficient for material characterization. A first strategy to measure 1D profiles takes advantage of magnets like the one described in subsection 4.3, which generates planes of constant field strength in a large depth range to select slices at different depths into the objects simply by switching the rf frequency electronically [Eid1, Pra1, Pra2, Cas2, Per2]. Although the retuning procedure is simple, and fast, it has some disadvantages. Density profiles are affected by relaxation times or self-diffusion in order to improve the discrimination of heterogeneities in the material, but when the depth is changed the values of these parameters vary introducing systematic changes in the contrast. First, the variation of the resonance frequency along the profile possesses a restriction to the use of T_1 contrast in samples with frequency dependent T_1. Second, the variation of the $\boldsymbol{B}_0$ and $\boldsymbol{B}_1$ field profiles leads to a depth dependence of the transverse relaxation time $T_{2\mathrm{eff}}$ measured by a CPMG sequence. Third, even the contrast by diffusion is distorted as a consequence of the variation of the static gradient as a function of the depth. Fourth, due to loss of $\boldsymbol{B}_1$ homogeneity and intensity with increasing depth, the proper excitation of the sensitive volume supposes increasing transmitter power (high intensity currents applied to the rf coil). Moreover there is a loss of receiver sensitivity that cannot be recovered.

The second strategy goes back to the original one used by the STRAFI technique [Hai1], where the sample profiling is performed just by changing the relative position of the sample with respect to the sensitive slice keeping the excitation frequency constant. Besides, being a distortion-free procedure, it only requires the generation of a flat sensitive slice at a single depth. This important reduction in constraints imposed to the field is exploited in refs. [Per1] and [Cas1], where a simple magnet geometry is used to

produce high depth resolution. A scheme of this sensor is shown in Fig. 4.23. It consists of four permanent magnet blocks positioned on an iron joke, two polarized along y, the others polarized along $-y$. The magnets with the same polarization are separated by a small gap d_s while, magnets with opposite polarization are separated by a larger gap d_b. By adjusting the gap widths, a constant field can be generated over a region of about 10 mm along the lateral directions. By increasing the gap d_b, the depth, where this region is defined also increases, while the field and gradient strength decrease. The size of d_b is then chosen to generate as slice at a distance from the sensor surface equal to the maximum required measurement depth. For the applications presented in this subsection a sensors with d_b = 14 mm generating the slice at 10 mm where the resonance frequency is 18.1 MHz and the gradient strength 22.4 T/m was built. Since the magnetic field is constant only in the finite region along the lateral directions, a rectangular two-turn surface coil was built to excite only this region, so that good resolution can be obtained. To vary the measurement depth, the sensor is placed on a high precision lift by means of which the sensitive volume can be shifted trough the object under investigation in steps of 10 μm. With this sensor 1D profiles with a spatial resolution better than 5 μm have been reported [Per1]. The procedure combined Fourier imaging of a slice thickness defined by the excitation bandwidth of the pulses with displacement of the sensor in steps equal to the slice thickness

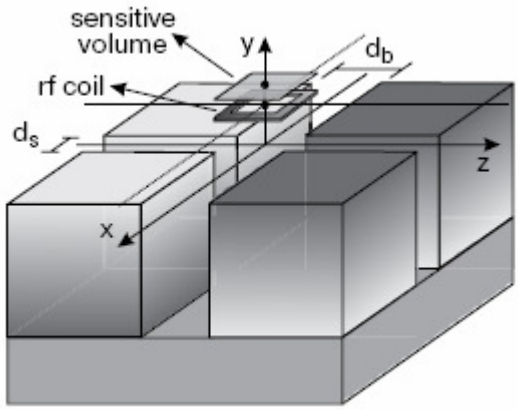

Fig. 4.23 Scheme of the profile-MOUSE showing the magnet geometry used to generate a highly flat sensitive volume. The direction of polarization of the magnets is indicated by the grey scale. The rf coil is positioned at a distance from the magnet surface in order to define the maximum required penetration depth (distance from the coil and the sensitive volume).

4.4.2 Single-sided NMR profiling of multi-layer objects

Air pressure tubes

The strong gradient of this sensor can be used to map the structure of multi-layer samples with high spatial resolution. Figure 4.24 shows the experimental setup for NMR profiling of a sample consisting of multiple layers of rubber and textile fibers. The sample is used in robotics and looks like a rubber tube with two non-magnetic metallic edges which enclose the volume of the tube. At one edge there is an opening to vary the air pressure inside the system. The rubber walls consist of a strongly reinforced elastic material and are meant to resist at high air pressures and fast pressure variations. With changing pressure the diameter of the tube changes too, due to the elasticity of the material. High inner pressure corresponds to an increase of the tube diameter at the expense of its length. When the air is let out, the diameter decreases to the equilibrium value and the tube "grows" in length to its initial state. By this simple mechanism, mechanic motion is achieved along the axis of the system.

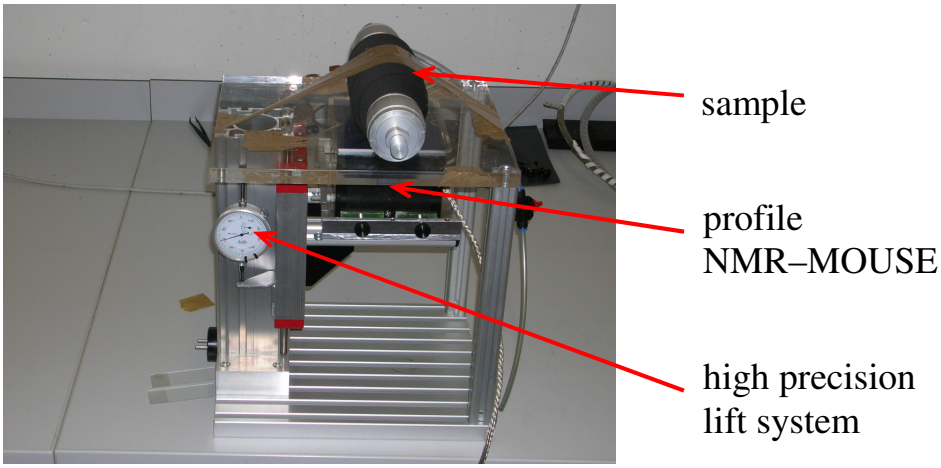

Fig. 4.24 Experimental set-up for NMR 1D profile imaging of a pressure tube. The NMR-MOSE is fixed on a lift with a sensitive distance counter. During the experiment, the sensor is moved up/down to scan the sample at different depths. The lift enables displacements of the probe with 10 µm precision.

Due to their great utility in the robotics industry, a quality monitoring of the pressure tubes is important. A good evaluation of the two states (completely relaxed and strongly tensioned) provides useful information about the systems work behaviour,

fatigue and lifetime. Obviously this kind of investigation requires a totally non-invasive technique. For this purpose, a profile NMR MOUSE operating at the resonance frequency of 18.1 MHz for protons was used to measure 1D profiles trough the pressure tube. The sensor was moved in steps of 50 µm acquiring at each position a CPMG train of 1000 echoes with t_E = 85 µs. The required resolution was obtained by using an acquisition window of 20 µs centered with the echo signal. The object was measured from outside (left) to inside (right) in three tensional states: relaxed, slightly pressurized, and at maximum pressure using the CPMG pulse sequence. The bi-exponential fits revealed variations of T_{2effL} and T_{2effS} across the material but without accurate information regarding its multi-layer morphology. Two extreme cases are depicted in Fig. 4.25a in terms of the 1D T_{2eff} profiles of the tube walls in the strongly tensioned and completely relaxed sates. The resolution in this plot is 100 µm. The T_{2effL} and T_{2effS} depth profiles are in good agreement and allow to discriminate three main layers: a ca. 0.5 mm thick outer and a similar inner layer (from 0 mm to 0.6 mm and from 1.5 mm to 2 mm respectively) with a ca. 1 mm thick less elastic layer in-between.

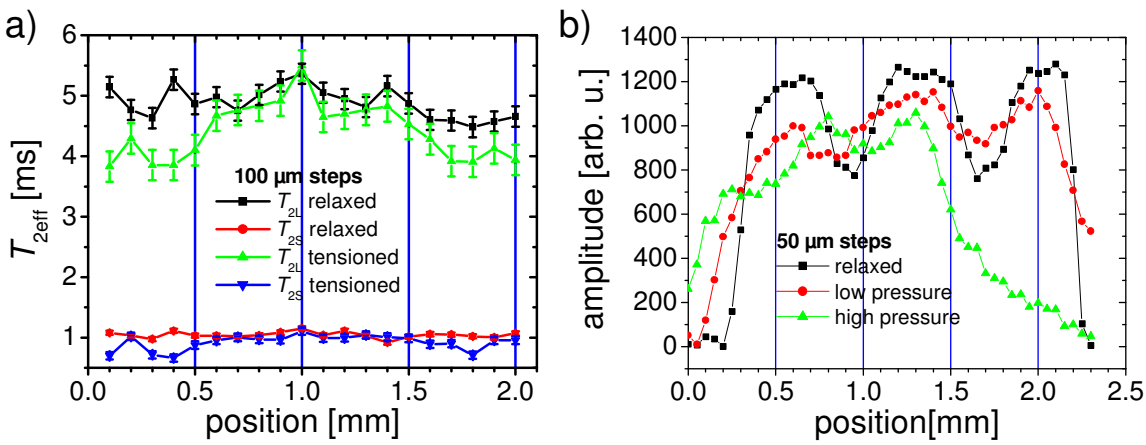

Fig. 4.25 a) T_{2effL} and T_{2effS} distributions trough the pressure tube wall in two states: relaxed and strongly pressurized. The material was scanned in steps of 100 µm; b) T_{2eff} weighted spin density profiles of the pressure tube in three physical states: relaxed, half pressurized, and strongly pressurized. Each data point is the sum of 500 echoes from a total of 1000 in the CPMG echo decay. The profile resolution is 50 µm.

T_{2eff} decreases all over along the depth when the tube is pressurised. The largest T_{2eff} drops correspond to the inner and outer layers suggesting there a strong dependence of the material hardness on strain. These regions can be interpreted as the elastic parts of the tube wall, while the middle layer, where the changes between the two states are

much smaller, can be interpreted as a rigid region. In this region there are probably some reinforcement structures to keep the system safe at the high pressures it is normally used to work.

As, a discrimination of these structures could not be done by means of transverse relaxation, spin density contrast was introduced. The $T_{2\text{eff}}$ weighted spin density depth profiles were drawn for the same sample in three different tensional states, by summing the first 500 echoes (from a total of 1000) in the CPMG decays (Fig. 4.25 b). Moreover the resolution was increased to 50 μm to enable the discrimination of narrower structures.

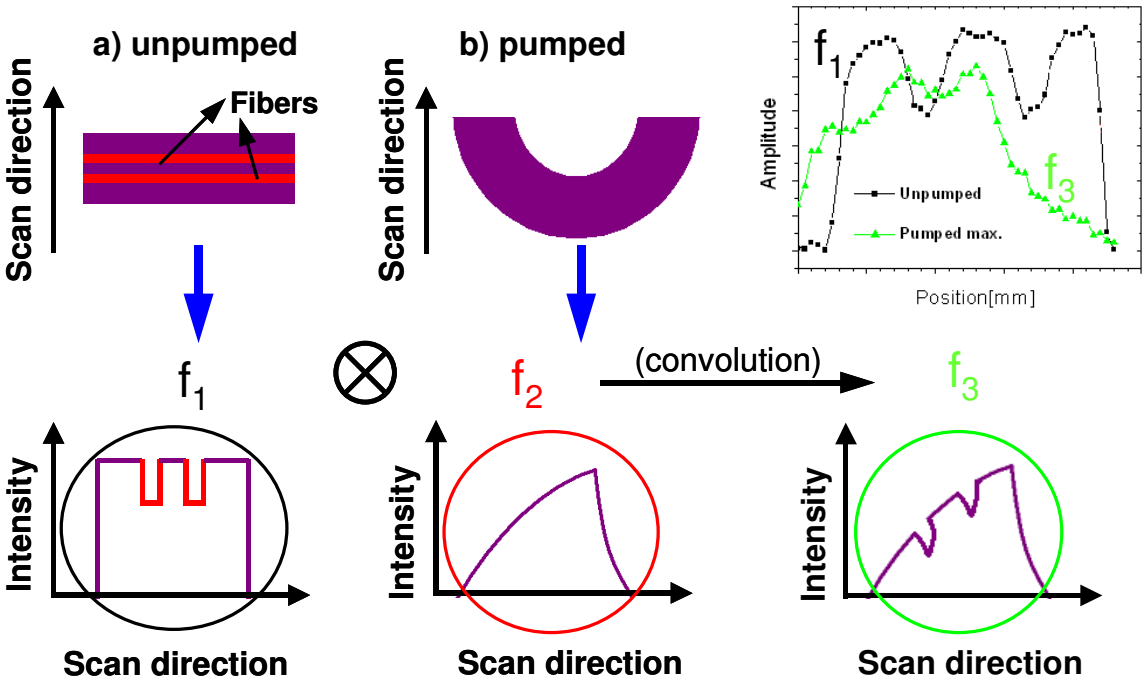

Fig. 4.26 Interpretation of the NMR profiles measured in textile-reinforced rubber tubes. The first theoretical function (f_1) modelling the intensity profile of the heterogeneous relaxed tube, and the second one (f_2) corresponding to the signal intensity of the curved object in a finite-width slice at different depths. The convolution of f_1 and f_2 gives the final function f_3 which is the theoretical intensity profile (bottom right) of the heterogeneous tensioned object. The experimental results (top right, or Fig. 4.25b) fit this model well.

The signal intensity variation trough the object reveals two layers of reinforcement fibres characterized by lower proton density (drops in the signal intensity). The total thickness of the material is exactly 2 mm. The first textile layer

starts at about 0.5 mm and the second layer ends at about 1.5 mm depth both having the same thickness of about 300 μm. This explains the $T_{2\mathrm{eff}}$ distribution diagram with the elastic inner and outer layers and the rigid central layer in-between.

Not only the multi-layer morphology, but also the shape of the sample in the different tensional states can be quantified using the high-resolution profiling method. In Fig. 4.25b there is a noticeable gradual change in material thickness and shape while going from the completely relaxed state to the highly pressurized state. The mechanism is described in Fig. 4.26. When the tube is relaxed its wall is almost flat. Scanning it in depth, one gets an intensity diagram which in the ideal case is a hat function (f_1) as wide as the thickness of the multi-layer material. The fibre layers will appear in this diagram as rectangular holes as wide as their thickness and at abscissa positions equal to their depth positions.

When pumping air inside the tube, it will progressively change its shape from flat to round. Without any error we can neglect for a moment the presence of fibres, to think only about the intensity diagram corresponding to the round shape. It can be described by a function like f_2 (Fig. 4.26) consisting of a slowly increasing part as the sensor advances in depth and the amount of material inside the sensitive volume gradually increases, and a second, faster decaying part, as the sensitive volume is already trough the wall but still intersects the object at its edges. Obviously f_2 is a function of the wall thickness as well as of the shape and lateral dimensions of the sensitive volume correlating with the diameter of the tube. The model above fits well for a rectangular sensitive volume like the one of the NMR-MOUSE used in our experiment.

The intensity diagram of the tensioned tube with the fibres inside can be easily obtained as shown in Fig 4.26 in terms of a third function f_3, which is the convolution of the “round shape effect function” with the “fibres effect function” namely f_2 and f_1. The experimental data are in very good agreement with this theoretical analysis. Moreover, the gradual decrease of the overall intensity with increasing pressure inside the tube (Fig. 4.25b), can be explained by the $T_{2\mathrm{eff}}$ weighting effect already discussed for the pure $T_{2\mathrm{eff}}$ diagram (Fig. 4.25a). When the sample is stretched it becomes harder, the signal decays faster, and the sum of the echoes will be smaller. The effect of stretching is also revealed by the change of wall thickness which for the pumped tube is with about 25 % less than for the completely relaxed one.

Oil pressure tubes

An interesting application of the profiling technique is the investigation of reinforced rubber tubes employed as pressure transmitters in technical devices. The largest domain of applications is the automotive industry where these tubes are important components of the brake systems. Thus, the investigations of the mechanical load effects (fatigue) as well as the degree of oil penetration in the material are important parameters for characterization and lifetime prediction.

The samples considered for this study were two tubes previously aged at an impulse test device (marked below as tube 1 and tube 2) and a new tube as reference. The profiles have been measured by scanning the tubes from inside to outside in steps of 0.1mm. The required resolution of 0.1 mm was obtained by using an acquisition window of 10 µs centered with the echo signal. The method used to generate and to measure the NMR signal, was the CPMG sequence. The temperature during experiment was 21° C with insignificant fluctuations, so that no temperature calibration was needed. To improve the signal-to-noise ratio, 128 scans with a repetition time of 300 ms were averaged for each step, defining a measurement time of 35 min for a complete profile.

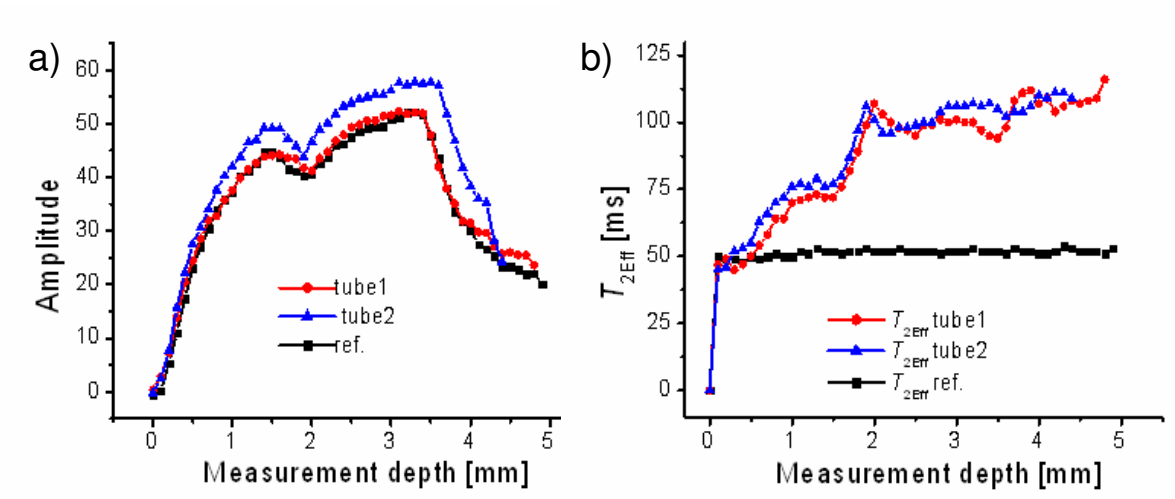

Fig.4.27 a) Amplitude profiles measured trough the three tubes. There is no major change between reference and mechanically tested tubes. b) The T_{2eff} profiles are very similar for the tested tubes and totally different from the reference which is nearly unaffected by position; T_{2eff} increases with increasing depth for the tested tubes encoded by the contribution of the oil to the average T_{2eff} of the material. Thus the T_{2eff} profile is a quantitative measure of the oil at each position and shows the direction of oil penetration (obviously from inside to outside).

The echo decay envelopes were fitted mono-exponentially to obtain the T_{2eff} information for every position. The spin density information (signal amplitude) was obtained with insignificant T_{2eff} -weighting from additions of the first 25 echoes in the CPMG decay. Nevertheless, the intensities were T_1-weighted since the repetition time of 300 ms used in this experiment is much shorter than the T_1 of the oil. Figure 4.27 a and b) shows the profiles measured trough the oil pressure tubes with a resolution of 100 µm. The amplitude profiles are roughly the same for all tubes (Fig. 4.27 a). The NMR signal amplitude gradually increases with increasing depth, a consequence of the round shape of the object. The fast decay at the end reveals a thickness of the hose wall of 3.5 mm. A reinforcement textile layer can be discriminated at about 2 mm depth in terms of a drop in signal intensity (lower proton density of oil and fibres compared with the rubber matrix).

Opposite to the previously presented case where for structure elucidation the T_{2eff} profile was irrelevant and a spin density contrast was necessary, here the spin density profiles make no discrimination between the mechanically tested tubes and reference. Nevertheless, the T_{2eff} contrast is strong (Fig. 4.27 b). This is due to the difference in transverse relaxation times of the different layers with different oil content. The oil, where the dipolar couplings are motional averaged has the longest T_{2eff} while, T_{2eff} of rubber is comparatively short because of the cross-linked macromolecular structure. Thus different oil/rubber ratios will lead to different average T_{2eff} values. In this way the T_{2eff} profiles are strongly contrasted by the presence of oil and the mechanically tested tubes can be well discriminated from the reference.

There is a monotone T_{2eff} increase from left to right as a consequence of increasing oil amount with increasing depth. The information concerning the tube wall thickness cannot be obtained from the T_{2eff} profiles with the same accuracy as from the intensity profiles. The reason is the remnant oil accumulation inside the tube channel during measurement which has an effect similar to an increased wall thickness. It appears in the T_{2eff} diagram as an oscillating end. In the spin density profile it is not obvious as the spin density of the oil used was much smaller than the one of the rubber.

The textile layers can be again well discriminated but only inside the aged hoses. They appear as tops in the T_{2eff} profiles at the same positions where the amplitude drops appeared in the intensity profiles. But, the reinforcement layer cannot be identified

in the relaxation profile of the reference hose. This facts suggest that in the cases of tube1 and tube2, the narrow top ($T_{2\mathrm{eff}}$ increase) is a consequence of the oil diffusion inside the textile layer. Nevertheless, the complementary (amplitude) profile outlines very well the reinforcement layer by the specific intensity decay seen for all hoses.

4.4.3 Surface UV aging of elastomers investigated with microscopic resolution by single-sided NMR

The action of UV light on polymers, and especially on elastomers is still not completely understood, although extensive data has been reported on the action of electromagnetic radiation on such materials [Wei1, Mil1, and Fow1]. Studying the interaction of UV irradiation with the elastomer network is an important topic in polymer science relevant to the polymer industry.

The interest in the transformation of organic polymers under the action of UV radiation relates to a number of reasons. First, polymer modification by ionizing radiation is an important technological means for functionalizing polymer surfaces [Sku1]. The reaction mechanism is complex and involves the actions of many primary particles. Second, an analysis of this process is important considering the material deterioration during processing and use in different environmental conditions. One example is the dry etching of polymer resists in microelectronics under the action of short wavelength light. Furthermore, the UV component of sun light deteriorates many polymeric materials especially in the presence of oxygen. Understanding long-term aging characteristics of elastomers is critical for performance assessment and lifetime prediction of such materials.

As the irradiation enters from the outside and is absorbed by the polymer, spatial heterogeneity develops in originally homogeneous objects. This spatial heterogeneity can be probed with microscopic resolution with a profile NMR MOUSE in terms of transverse magnetization relaxation times which are very sensitive to cross-link density variations. In this context, high resolution ^{1}H NMR depth profiles have been obtained near the surface of a rubber sample after exposing it to UV radiation for several days. An NMR observable related to the sum of the spin echoes in the Carr-Purcell-Meiboom-Gill pulse sequence was used to characterize the cross-link density changes produced by the

action of the UV radiation. An exponential attenuation law with a linear space dependent absorption coefficient was proposed to describe the measured space profiles at different irradiation times.

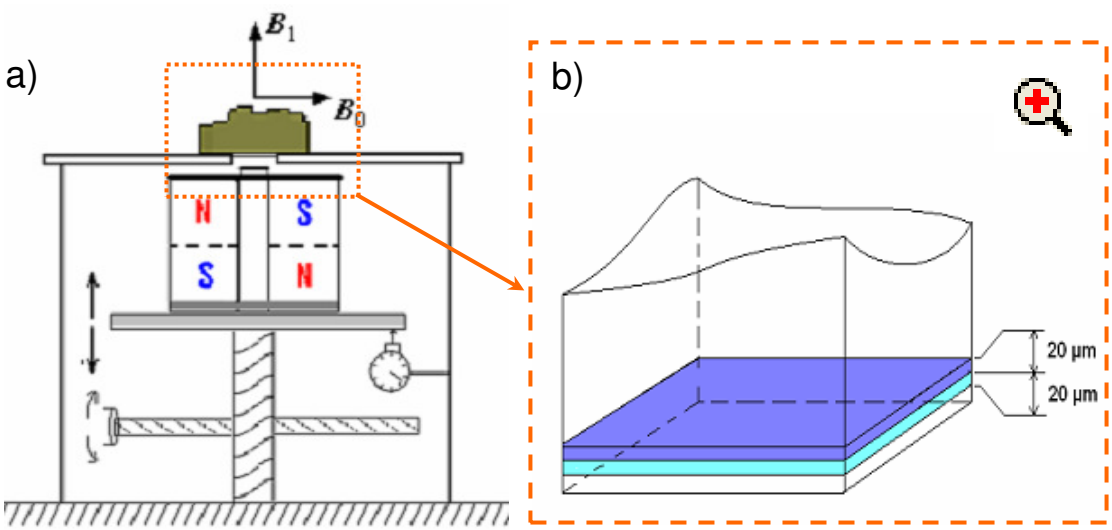

Fig. 4.28 a) Experimental setup for the measurement of microscopic profiles across a UV aged cross-linked NR sample. The Profile NMR-MOUSE is mounted on a high precision lift by which the distance between the NMR-MOUSE and the object on top of the lift can be changed with micrometer resolution. b) Schematic representation of a section of the object and the sensitive volume at two positions.

Experimental

The sample was a cross-linked NR with 3 phr sulphur content (for preparation details see Subsection 4.2.5). It was irradiated with a 300 W Osram Ultravitalux UV lamp with an emission spectrum in the 300 - 400 nm wavelength range. The total irradiation time was eight days. The NMR measurements were done after five hours, one day, two days, four days, and eight days of irradiation. The distance between sample and radiation source was 20 cm.

To characterize the segmental dynamics of the elastomer after irradiation, a set-up consisting of the profile NMR-MOUSE [Per1] and a high precision lift was used. The experimental setup is presented in Fig. 4.28a. The depth profiles were measured in increments of 20 µm (Fig. 4.28b) at a resonance frequency of 18.1 MHz in a uniform gradient of 22.3 T/m.

Carr-Purcell-Meiboom-Gill decays (CPMG) were acquired in the strongly inhomogeneous magnetic field of the sensor to measure the transverse NMR relaxation. The nominal 90° and 180° pulses were 20 µs, exciting a frequency bandwidth of ca. 50 kHz, and the acquisition time was set to 50 µs to achieve a frequency resolution of 20 kHz per acquisition step. Each sample was measured in 30 steps from the surface up to a depth of 0.6 mm. The dead time of the radio-frequency set up was 30 µs. The CPMG-train consisted of echoes acquired with echo times of 130 µs. The number of scans was 256 with a repetition time of 0.5 s. The NMR experiments were performed at 23° C with a temperature stability of ± 0.1°C.

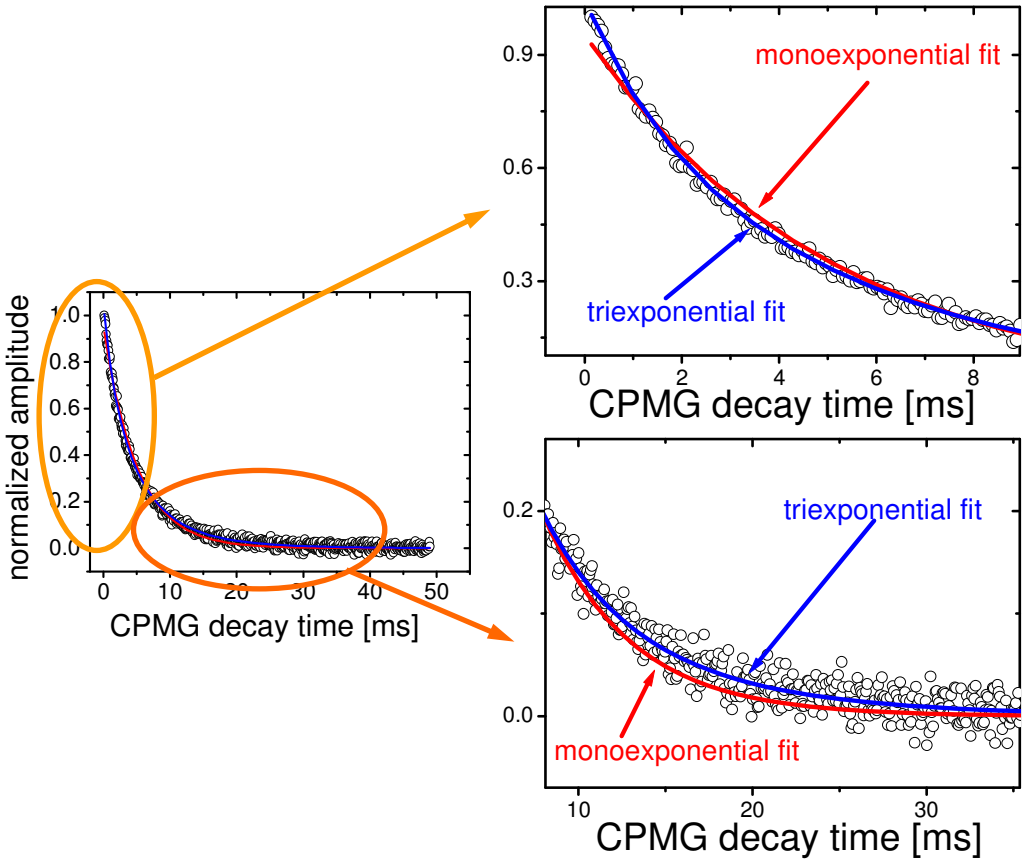

Fig. 4.29 Mono-exponential and tri-exponential fits of the CPMG echo decay measured in a 20 µm thick sheet of an UV aged NR sample. The zoomed sections of the decay reveal improvements in the fit when going from a mono-exponential to the multi-exponential fit.

Values of the effective transverse relaxation time $\overline{T}_{2\mathrm{eff}}$ were evaluated from mono-exponential fits of the CPMG echo decays. The average over the micro-

heterogeneity of the sample is denoted by a bar. A large error in the fit with a single exponential and an improvement in the quality of the fit when fitting with a bi- or tri-exponential function revealed a multi-exponential nature of the decays (Fig. 4.29). However, the use of a fit function with a large number of exponentials would have complicated this study which was mainly focused on mapping the layer structure generated by the irradiation.

A suitable NMR parameter with high sensitivity towards changes in the rubber network segmental dynamics that can be derived from the CPMG decay is the integral of the initial part of the normalized echo train. It is straightforwardly obtained as the sum of the echo amplitudes divided by the mean amplitude of the first few echoes. Moreover, a summation of N_{echo} echoes increases the signal-to-noise ratio (S/N) by approximately:

$$\frac{\mathrm{S}}{\mathrm{N}} \propto \sqrt{\mathrm{N}_{echo}} \tag{4.10}$$

The normalized sum of *N* echoes

The amplitude S_{NMR} of each point in the depth profile is derived from the envelope of the CPMG echo decay. Suppose the echo decay is described by an exponential function characterized by an average effective transverse relaxation time $\overline{\mathrm{T}}_{2eff}$. Let us denote with S_0 the amplitude of the CPMG train extrapolated to $t = 0$ by ignoring the first echo. The sum of the echoes 2 to N+1 is then given by

$$S_{\mathrm{N}} = S_0 \sum_{i=1}^{N} \mathrm{e}^{-\frac{2\tau i}{\overline{T}_{2\mathrm{eff}}}}. \tag{4.11}$$

where 2τ is the echo time. We will define our NMR variable as:

$$S_{\mathrm{NMR}} \equiv \frac{S_{\mathrm{N}}}{S_0} = \sum_{i=1}^{N} \mathrm{e}^{-\frac{2\tau i}{\overline{T}_{2\mathrm{eff}}}}. \tag{4.12}$$

After computing the sum of N terms in the geometrical progression above (Eq. 4.12) we can write:

$$S_{\mathrm{NMR}} = \frac{1-\exp\left\{-2\tau N / \overline{T}_{2\mathrm{eff}}\right\}}{1-\exp\left\{-2\tau / \overline{T}_{2\mathrm{eff}}\right\}}. \tag{4.13}$$

For an echo time 2τ that fulfills the condition $2\tau << \overline{T}_{2\mathrm{eff}}$ we finally obtain

$$S_{\mathrm{NMR}} \approx \frac{\overline{T}_{2\mathrm{eff}}}{2\tau} - \frac{\overline{T}_{2\mathrm{eff}}\left(1-\frac{2\tau}{\overline{T}_{2\mathrm{eff}}}\right)^{N}}{2\tau}. \tag{4.14}$$

If the condition $2\tau/\overline{T}_{2\mathrm{eff}} \leq 2$ is fulfilled, the second term in the expression above is small and can be neglected, so that one can write

$$S_{\mathrm{NMR}} \approx \frac{\overline{T}_{2\mathrm{eff}}}{2\tau}. \tag{4.15}$$

In the limit of short echo times, the NMR observable is proportional to $\overline{T}_{2\mathrm{eff}}$.

Results and discussion

When a polymer is irradiated with UV light, primary and secondary processes take place [Sku1]. The primary processes are first transformations which occur when the polymer chain absorbs radiation doses exceeding its ionization energy, leading to formation of charge pairs, free charges, singlet excitation, and in much smaller amount, triplet excitation. The excited states can further decompose following either a free radical path with yields of macromolecular radicals and protons, or the molecular path when molecular hydrogen is rendered with the formation of double bonds in the macromolecule. At high irradiation energies, the polymer chain can be destroyed with the formation of long chained radicals.

The rearrangements following the minimum energy rules are known as secondary processes. Here the previously formed hydrogen atoms or molecules can either recombine with the macromolecules forming molecular hydrogen-radical pairs or saturating double bonds, or the unsaturated double bonds can migrate along the macromolecular backbone. In parallel, the ionization of double bonds can result in great acceleration of the decay of double bonds in the processes of intramolecular cross-linking (cyclization) and intermolecular cross-linking. Meanwhile, ionic cross-linking and physical cross-linking (entanglements) as a consequence of increased entropy are likely to occur increasing even more the cross-link density of the irradiated polymer.

The effect of UV radiation on cross-linked natural rubber was characterized not only as function of penetration depth but also as function of irradiation time, as time cumulative UV radiation induces increased physical aging in the polymer network in

addition to the chemical aging. The main effect of both is an increase of cross-link density at the surface of the sample. This will lead to a larger attenuation of the CPMG decays and therefore, to smaller values of our NMR observable. The attenuation of the radiation intensity with the penetration depth is represented as a plot of the effective transverse relaxation rate that is proportional with $1/S_{\mathrm{NMR}}$ (Eq. 4.15), versus depth (Fig. 4.30a) and inversely proportional to the cross-link density [33]. The average attenuation coefficient $\langle\mu\rangle$ has been calculated on the basis of the Beer-Lambert law. In this case the attenuation coefficient was considered as not changing with the position inside the sample but depending on the irradiation time t, i.e., $\langle\mu\rangle = \langle\mu\rangle(t)$. In the limit of the above approximation the attenuation law of the UV radiation is written as:

$$I(x) = I_0 e^{-\langle\mu\rangle x} \tag{4.16}$$

where $I(x)$ is the intensity of the UV radiation at a distance x from the sample surface. The intensity of the radiation at the surface $x = 0$ is I_0.

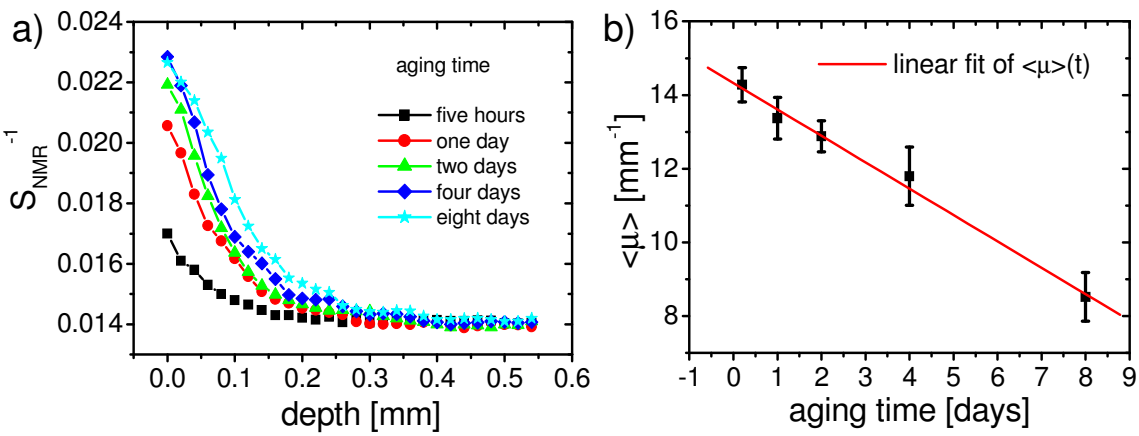

Fig. 4.30 a) Effects of UV aging versus depth for different UV irradiation times. The quantity $1/S_{\mathrm{NMR}}$ is proportional to the reciprocal of the effective transverse relaxation time. b) Variation of the average attenuation coefficient $\langle\mu\rangle$ with the UV irradiation time (depth independent attenuation coefficient approach). The quasi-linear decrease (solid-line) of the attenuation coefficient suggests time-proportional qualitative modifications inside the polymer material exposed to UV irradiation.

Fitting the experimental data shown in Fig. 4.30a with the exponential function 4.16, the $\langle\mu\rangle$ values are obtained. A plot of the average attenuation coefficient versus

aging time shows a decrease of $\langle\mu\rangle$ with increasing irradiation time (Fig. 4.30b). The quasi-linear decrease of $\langle\mu\rangle$ with increasing irradiation time could be explained by the primary processes of photolysis discussed above. The efficiency of these processes increases proportionally to the irradiation time. The more chains are broken the less attenuated the incident light intensity is at a given depth x in the material. In this scenario the secondary processes like cyclization, intermolecular cross-linking, or ionic cross-linking, which statistically occur with high probability, are neglected. Meanwhile, physical processes like entanglements (physical cross-linking) as a consequence of the higher mobility of the broken chains are likely to occur as well.

Due to these complex processes the attenuation coefficient of UV radiation can be dependent on the intensity of the radiation and therefore on the position of the sample layer from the surface. Following this approach, the topological constraints and cross-link density will change gradually from the network surface into the bulk. Therefore, not only the intensity $I(x)$ of UV radiation will change with the distance x from the surface but also the attenuation coefficient μ will become space dependent, i.e. $\mu = \mu(x)$. We can assume that μ can be written as a quantity that exponentially decreases with the distance in the sample. Therefore, we can write

$$\mu(x) = \mu_0 \exp\{-kx\}, \tag{4.17}$$

where $\mu(x)$ is the attenuation coefficient at depth x, $\mu_0 \equiv \mu(x=0)$ is the UV absorption coefficient at the surface of our sample, and k is the spatial decay constant of the absorption coefficient. This coefficient can be correlated with supplementary cross-linking induced by the UV radiation in the polymer network. In principle, both quantities μ_0 and k are functions of the irradiation time.

The attenuation law of the UV irradiation takes into account the gradual change of electromagnetic radiation intensity with the distance. The Beer-Lambert law can be generalized for the case of space-dependent absorption coefficient, and from Eq. (4.15) and Eq. (4.17) we get

$$\frac{\mathrm{d}I(x)}{\mathrm{d}x} = -\mu_0 e^{-kx} I(x), \tag{4.18}$$

where $I(x)$ is the intensity of the incident UV radiation at the depth x measured from the polymer network surface. The solution of Eq. (4.18) representing the dependence of the UV intensity *I(x)* as a function of the penetration distance x measured from the sample surface has the form

$$I(x) = I_0 \exp\left\{\frac{\mu_0}{k}\left(e^{-kx} - 1\right)\right\}. \tag{4.19}$$

where, by I_0 is denoted he intensity of UV radiation at the surface of the polymer network. When $kx << 1$, the classical law of radiation attenuation is obtained from Eq. (4.18), i.e., $I(x) = I_0 \exp\{-\mu_0 x\}$. For small variations of μ, the generalized attenuation law becomes $I(x) = I_0 \exp\{-\langle\mu\rangle x\}$ where $\langle\mu\rangle$ is the average value of $\mu(x)$.

The data shown in Fig. 4.30a represent the NMR signal as function of depth for different aging times. They were fitted with Eq. 4.19. These fits are shown in Fig. 4.31a. Figure 4.31b depicts one of the experimental data sets (sample irradiated for two days) together with the fit function. Plots of μ_0 and k versus irradiation time are shown in Fig. 4.31c, and d. Figure 4.31d depicts k as a function of irradiation time. It shows a monotonic decrease of the variation rate of μ with the irradiation time. The decrease of the quantity k suggests a tendency to reduce the variation of μ with the depth at prolonged exposure of the polymer to irradiation. When going to extremely long irradiation times, k becomes very small and the attenuation coefficient μ will be constant along the irradiation depth direction, i.e., $\mu(x) \approx \mu_0$. The plot of μ_0 versus irradiation time (Fig. 4.31c) shows an increase of the attenuation coefficient at the sample surface followed by saturation after ca. two days of irradiation. The increase of μ_0 can be explained as consequence of the increasing UV radiation induced cross-link density until saturation.

The dependence of the quantity μ_0 on the aging time can be quantified based on a law similar to the Avrami law. The increase in cross-link density with UV irradiation exposure time is plausible to be described by a relationship similar to the Avrami equation [34]. We can chose this dependence to be of the form:

$$\mu_0 = A_2 - A_1 \exp(-Kt_a^n), \tag{4.20}$$

where K and n are Avrami parameters. The difference A_2 - A_1 corresponds to the value of μ_0 at the aging time $t_a = 0$. The coefficient A_2 describes the saturation value of μ_0. This equation was used to fit our experimental data, namely μ_0 versus aging time (Fig. 6a). The quality of the fit supports the Avrami functional dependence for the interpretation of the evolution of polymer aging effects induced by UV light with the aging time.

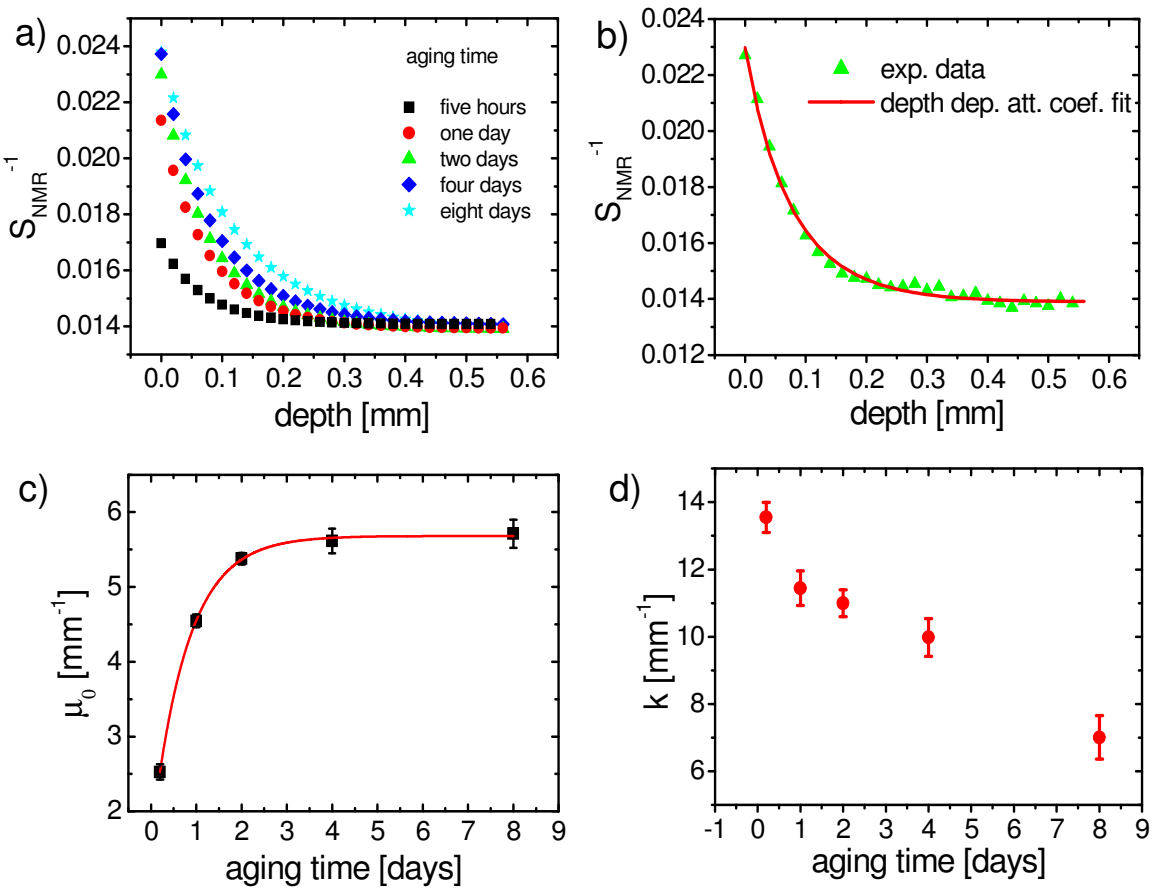

Fig. 4.31 a) Fits of $1/S_{NMR}$ with Eq. 4.19 as function of depth for different aging times. b) One of the experimental data sets (NR UV-irradiated for two days) together with the fit curve. The uncertainty of the fit is less than 4%. c) Plot of μ_0 versus aging time fitted with an Avrami model function. d) Plot of k versus UV irradiation time. The variation rate of μ has a monotone decrease with increasing irradiation

Chapter 5

Conclusions

The experiments conducted in this work demonstrate the sensitivity of single-sided NMR for detection of heterogeneities in polymers and biological materials. Elastomer materials can readily be characterized by unilateral NMR of protons in terms of a variety of parameters, which correlate with the overall molecular mobility. In this way information is obtained non-destructively about cross-link density, state of cure, the effects of aging, and product heterogeneity. For these reasons the NMR-MOUSE can be used to optimize product development, and to monitor product and production quality.

In Subsection 4.2 it was shown that the mobile NMR sensor is suitable for operation in an industrial environment. Variations in product homogeneity have been observed with the NMR-MOUSE at different steps in the production of tyres. The characterization was done for all products including the unvulcanised and vulcanized tires which are inaccessible to classical test methods like rheometry or RPA. Moreover, even in production steps where RPA could be implemented for complementary product analysis, the NMR-MOUSE showed higher sensitivity. The tyres with high $\overline{T_{2\mathrm{eff}}}$ before vulcanization showed a low spread in $\overline{T_{2\mathrm{eff}}}$ after vulcanization. As $1/\overline{T_{2\mathrm{eff}}}$ correlates with the modulus, the soft material leads to a rather homogeneous product, in agreement with a homogenization of the product being achieved during vulcanization by component diffusion.

Nondestructive testing by single-sided NMR opens a window for probing mechanical deformation at a molecular scale. Fatigue due to excessive mechanical stress is routinely tested by cyclic loading of test bodies such as rubber stripes. A small NMR sensors based on the classical permanent magnet configuration has been built to fit a stress-strain device for rubber stripes. The stress-strain curve could be mapped simultaneously with the mechanical measurement by recording CPMG decay curves at different strains. As expected from the proportionality of NMR relaxation rates and elongation, the inverse of the relaxation time $T_{2\mathrm{eff}}$ obtained from summing all the echoes of the CPMG decay parallels the stress-strain curve up to about 400% elongation. Such a set-up promises to be of use for predicting the time of failure based on NMR relaxation measurements in cyclic loading tests.

In Subsection 4.2 the possibility to generate one-dimensional maps of the distribution of Young`s and shear moduli in elastomers was reported. Elastomers are complex macromolecular systems with statistical distributions of many molecular properties. A strategic objective for investigation is the correlation of the molecular information obtained by different NMR methods with the structural and viscoelastic proprieties of polymers. Such correlations can be especially useful for the characterization of ageing in natural rubber. One-sided NMR sensors with different configurations have been tested for this purpose. The calibrations of ^{1}H transverse magnetization rates versus the elastic and shear moduli were justified based on the ^{1}H residual second van Vleck moments previously measured on the same series of natural rubber samples and reported by Fechete et. al [Fec1].

The inverse proportionality between transverse relaxation time and cross-link density was verified even at high degrees of cross-linking (up to7 phr sulphur content). However, the plots depicting $1/T_{2\mathrm{eff}}$ versus mechanical moduli (E and G), preserve the linearity of the correlation functions only at low cross-link densities (up to 4 phr sulphur content). At high cross-link densities the correlation functions become obviously more complicated. Nevertheless, for a sample with large $1/T_{2\mathrm{eff}}$ variations in this range, the correlation maps can be used with good precision to determinate the values of E and G.

The second order van Vleck moment measured at high and homogeneous magnetic field (7 T, DMX 300) was also plotted as a function of relaxation times measured with the NMR-MOUSE (0.4 T). The segmental order measured by the residual second van

Vleck moment was previously shown to scale with a polynomial dependence on cross-link density or shear modulus [Fec1]. This can be interpreted by considering high-order corrections to a Gaussian distribution of the end-to-end vectors. Like in the plot of $1/T_{2\mathrm{eff}}$ versus cross-link density, the linearity of the function describing $\langle M_2 \rangle$ versus $1/T_{2\mathrm{eff}}$ was found to be preserved even at high cross-link densities. Although the experiments were performed in different $\boldsymbol{B}_0$ field strengths and homogeneities, the two NMR parameters correlated very well following the theoretical predictions. This confirms that single-sided NMR relaxometry is a valid alternative to measurements at homogeneous magnetic fields.

Furthermore, the effects of aging in PE water pipes were studied. A U-shaped NMR-MOUSE was used for this purpose. It was showed that not only in the case of cross-link elastomers, but even for semicrystalline polymers like PE, unilateral NMR provides relevant information about morphology. The transverse relaxation times obtained from a bi-exponential fit of the CPMG decays were used to characterize the homogeneity of PE tubes employed for a long period of time underground as water pipes. A decrease of $\overline{T_{2\mathrm{effL}}}$ was observed in the failure positions of the pipes as a consequence of decreasing chain mobility. Moreover, depending on the type of mechanical impact it was found that the heterogeneous profile of the damage material changes, and this change could be discriminated in terms of transverse relaxation data.

The development of imaging techniques suitable to be implemented on single-sided sensors has opened a broad field of new applications in medicine and material science. Besides being a non-destructive technique, single-sided NMR allows *in situ* characterization of large immobile objects. In Subsection 4.3, the strategies developed to incorporate 2D and 3D spatial resolution and enhance contrast on single-sided sensors, have been presented in a number of applications that illustrate the performance of the technique in fields like quality control, medicine and material science.

When applying a pure phase-encoding sequence on a sensor equipped with a gradient system, 3D images can be reconstructed by combining cross sections of the sample measured at different depths. The method allows one to produce contrast in the images by averaging different parts of the multi-echo acquisition train. The imaging technique was used to detect failures in finished products, and to map the stress distribution in materials under load. Furthermore, it was implemented to study biological

structures like the *mandibula* of a rat in vitro with potential future *in vivo*-applications in the maxilo-facial surgery, and the morphology of plants leaves. In these domains, further improvements of the technique could provide access to functional information as well.

The generation of uniform static gradients provides a simple method to resolve layered structures changing only along the depth direction. In Subsection 4.4, a high-resolution profiling technique has been exploited to resolve multi-layer structures and to follow dynamic processes like the absorption of oil in high pressure rubber hoses or the UV aging of cross-link elastomers.

Like in multi-dimensional imaging, the contrast can be enhanced in different ways to highlight along the preferential direction the morphology changes of the material under investigation. To resolve the multi-layer structure of air-pressure tubes implemented in robotics, the spin-density contrast was found to be most proper. Later, the same technique was successfully implemented to resolve the depth structure of oil-pressure hoses. However, the effect of oil ingress in the material could not be observed from the spin density profiles. In this case the $T_{2\mathrm{eff}}$ contrast made possible the discrimination between the previously tested tubes and reference.

In a related study, the Profile NMR-MOUSE was found to be a unique tool for the characterization of changes induced by the UV irradiation in natural rubber. An NMR observable based on the sum of the initial CPMG echoes was shown to be proportional to the average transverse relaxation time and used to build the UV attenuation profiles. The aging profiles were interpreted for the first time based on a novel model in which the radiation absorption coefficient depends on the depth in the sample. The parameters describing the depth dependence of the radiation attenuation coefficients are functions of the aging time, thus an Avrami-like equation was proposed to describe the changes in the absorption coefficient with irradiation time. Being a sensitive method for the measurement off cross-link density modifications in elastomers, NMR relaxometry with high precision mobile sensors like the profile NMR-MOUSE can be used to quantitatively and qualitatively characterize the surface aging effects induced by different physical and chemical agents.

NMR is a proved powerful method for characterization of structure and motion in materials. Compared to other physical investigation methods, NMR provides unique information from a large variety of experiments which make the method irreplaceable.

In particular, single-sided NMR exhibits important advantages like non-invasiveness and non-destructiveness, portability, simplicity and not least, low costs. It shows up in its different shapes as a unique tool for characterization of a large variety of materials in an ever broadening field of applications.

Appendix

Dependence of the residual second van Vleck moment on cross-link density

For ideal polymer chains, the most significant and distinctive property is the Gaussian distribution of the end-to-end distances. Tacking into account that different segments of the freely jointed chain are statistically independent and can be represented by a Markov chain it is possible to derive the correction to the Gaussian distribution of the end-to end distances $\left|\vec{R}\right|$ [Gro1]. In the approximation of the first correction term the distribution of $\left|\vec{R}\right|$ is given by [Gro1]

$$P_N^{(c)}\left(\left|\vec{R}\right|\right) \cong P_N\left(\left|\vec{R}\right|\right)\left[1-\frac{3}{20N}\left(5-\frac{10\vec{R}^2}{Na^2}+\frac{3\vec{R}^4}{N^2a^4}\right)+\ldots\right], \tag{A1}$$

where the Gaussian distribution function is

$$P_N\left(\left|\vec{R}\right|\right)=\left(\frac{3}{2\pi Na^2}\right)^{3/2}\exp\left\{-\frac{3\vec{R}^2}{2Na^2}\right\}. \tag{A2}$$

From the distribution $P_N^{(c)}\left(\left|\vec{R}\right|\right)$ corrected in first order it is possible to calculate all moments, i.e., the averaged values of any even power of $\vec{R}$. From the Gaussian distribution function, Eq. A2, we get,

$$\left\langle\left(\vec{R}^2\right)^n\right\rangle_{\vec{R}}=\int_0^\infty\left(\vec{R}^2\right)^n P_N\left(\left|\vec{R}\right|\right)d\vec{R}, \tag{A3}$$

and finally,

$$\left\langle\left(\vec{R}^2\right)^n\right\rangle_{\vec{R}}=\left(Na^2\right)^n\frac{1\cdot 3\cdot\ldots\cdot(2n+1)}{3^n}. \tag{A4}$$

Considering a DCF over a statistical ensemble, the residual second van Vleck moment is given by [Fec1]

$$\langle M_2 \rangle = -\frac{1}{\mathrm{Tr}\{I_y^2\}} \left\langle \mathrm{Tr}\left\{(\hat{\bar{H}}_d I_y)^2\right\} \right\rangle_{\vec{R},\beta} \tag{A5}$$

in which the average is taken over the distribution of the lengths of the end-to-end vectors and their orientation relative to the static magnetic field.

In order to obtain the dependence of the residual second van Vleck moment (cf. Eq. A5) on the cross-link density or shear modulus (see below) one has to calculate the average over the end-to-end vector distance for the quantity, $\left(\frac{\vec{R}^2}{N^2 a^2}\right)^2$. Using the corrected Gaussian distribution function given by Eq. A1, Eq. A4, and Eq. A5 one finally gets [Fec1]

$$\langle M_2 \rangle \propto \left\langle \left(\frac{\vec{R}^2}{N^2 a^2} \right)^2 \right\rangle_{\vec{R}} \cong \frac{5}{3}\frac{1}{N^2} - \frac{2}{3}\frac{1}{N^3}. \tag{A6}$$

It is concluded that in the limit of the approximation used above the residual second van Vleck moment scales with $1/N^2$ for high numbers of statistical segments, i.e., for N>>1, meaning small values of the cross-link densities.

The effective number of statistical segments N is defined from the number of segments $N^{(0)}$ between physical cross-links or topological constraints and the number $N^{(C)}$ of segments between chemical cross-links. If we assume that the contributions to the residual dipolar coupling are additive and topological constraints are independent of the degree of chemical cross-linking we can write: $(N)^{-1} \approx \left(N^{(0)}\right)^{-1} + \left(N^{(C)}\right)^{-1}$. In this case it is expected (cf. Eq. A5) that $\langle M_2 \rangle$ has a polynomial dependence on the cross-link density or shear modulus. Moreover, in the limit of vanishing chemical cross-linking $\left(N^{(C)}\right)^{-1} \to 0$ the value of the residual second van Vleck moment is finite.

References

Abr1 A. Abragam, "Principles of Nuclear Magnetism", Oxford Academic Press, London, 1961.

Anf1 S. Anferova, V. Anferov, M. Adams, P. Blümler, K. Hailu, K. Kupferschläger, M. J. M. Mallett, G. Schroeder, S. Sharma, B. Blümich, Construction of an NMR-MOUSE with short dead time, Concepts Magn. Reson. 15, 15–25 (2002).

Anf2 S. Anferova, V. Anferov, M. Adams, R. Fechete, G. Schroeder, B. Blümich, Thermo-oxidative aging of elastomers: a temperature control unit for operation with the NMR-MOUSE®, Appl. Magn. Reson. 27, 361–370 (2004).

Arm1 R. L. Armstrong, A. Tzalmona, M. Menzinger, A. Cross, and C. Lemaire, in B. Blümich and W. Kuhn, eds., Magnetic Resonance Microscopy, VCH, Weinheim, 1992.

Bal1 F. Balibanu, K. Hailu, R. Eymael, D. E. Demco, B. Blümich, NMR in inhomogeneous magnetic fields, J. Magn. Reson. 145, 246–258 (2000).

Bax1 A. Bax, "Two-dimensional NMR in Liquids", Delft University Press, D. Reidel Publ. Comp., Dortrecht, 1982.

Blo1 F. Bloch, W. W. Hansen, M. Packard, Nuclear Induction, Phys. Rev. 69, 127 (1946).

Blo2 F. Bloch, The nuclear induction experiment, Phys. Rev. 70, 460 (1946).

Blo3 N. Bloembergen, E. M. Purcell, R. V. Pound, Relaxation Effects in Nuclear Magnetic Resonance Absorption, Phys. Rev. 73, 679–712 (1948).

Blü1 B. Blümich, "NMR Imaging of Materials", Clarendon Press, Oxford, 2000.

Blü2 P. Blümler, B. Blümich, Magnetization Filters: Applications to NMR Imaging of Elastomers, Magn. Reson. Imag. 10, 779–788 (1992).

Blü3 B. Blümich, V. Anferov, S. Anferova, M. Klein, R. Fechete, M. Adams, F. Casanova, Simple NMR-MOUSE® with a Bar Magnet, Concepts Magn. Reson 15B, 255–261 (2002).

Blü4 B. Blümich, S. Anferova, F. Casanova, K. Kremer, J. Perio, S. Sharma, Unilateral NMR: Principles and Applications to Quality Control of Elastomer Products, Kaut. Gummi Kunstst. 57, 346 (2004).

Blü5 B. Blümich, "Essential NMR", Spinger, Berlin, 2005.

Blü6 P. Blümler and B. Blümich, NMR imaging of elastomers: a review, Rubber Chem. Technol. 70, 469 (1997).

Blü7 B. Blümich and D. E. Demco, in V. M. Litvinov, and P. P. De, eds., "Handbook of Spectroscopy of Rubbery Materials", Rapra Technology Ltd., Shawbury, 2002.

Blü8 P. Blümler and B. Blüumich, NMR imaging of solids, NMR Basic Princ. Prog. 30, 211 (1994).

Blü9 B. Blümich, Contrast in Solid-State NMR Imaging, Part I: Principles, Conc. Magn. Reson. 10, 19 (1998).

Blü10 B. Blümich, Contrast in Solid-State NMR Imaging, Part II: Basic Filters, Conc. Magn. Reson. 11, 71-87 (1999).

Blü11 P. Blümler and B. Blümich, Aging and Phase Separation of Elastomers Investigated by NMR Imaging, Macromolecules 24, 2183 (1991).

Blü12 P. Blümler and B. Blümich, Investigation of stress distributions in filled polysiloxane by NMR imaging. Acta Polymer. 44, 125-131 (1993).

Blü13 B. Blümich, P. Blümler, G. Eidmann, A. Guthausen, R. Haken, U. Schmitz, K. Saito, G. Zimmer, The NMR MOUSE: Construction, Excitation, and Applications, Magn. Reson. Imag. 16, 479–84 (1998).

Blü14 B. Blümich, V. Anferov, S. Anferova, M. Klein, R. Fechete, An NMR-MOUSE for Analysis of Thin Objects, Macromol. Mat. Eng. 288, 312–317 (2003).

Blü15 P. Blümler, B. Blümich, and H. Dumler, *Kautsch. Gummi. Kunstst.* **45**, 699 (1992).

Blü16 B. Blümich, S. Anferova, K. Kremer, S. Sharma, V. Herrmann, A. Segre, Unilateral NMR for Quality Control: The NMR-MOUSE®, Spectroscopy 18, 18-32 (2003).

Blü17 B. Blümich, F. Casanova, J. Perlo, S. Anferova, V. Anferov, K. Kremer, N. Goga, K. Kupferschläger, M. Adams, Advances of unilateral mobile NMR in nondestructive materials testing, Magn. Reson. Imag. 23, 197–201 (2005).

Bre1 W. S. Brey, ed., "Pulse methods in 1D and 2D liquid-phase NMR", Academic Press, New York, 1988.

Bro1 J. Brossel and A. Kastler, La detection de la resonance magnetique des niveaux excites-l'effect de depolarization des radiations de resonance optique et de fluorescence, Cr. Hebd. Acad. Sci. 229, 1213–1215 (1949).

Bro2 S. B. Brown and H. W. Spiess, Advanced Solid-State NMRMethods for the Elucidation of Structure and Dynamics of Molecular, Macromolecular, and Supramolecular Systems, Chem. Rev. 101, 4125 (2001).

Bro3 R. J. S. Brown, Nuclear magnetism logging at the Coyote Institute, Magn. Reson. Imag. 14, 811– 17 (1996).

Bro4 R. J. S. Brown, R. Chandler, J. A. Jackson, R. L. Kleinberg, M. N. Miller, Z. Paltiel, M.G. Prammer, The History of NMR Well Logging, Concepts Magn. Reson. 13, 340-411 (2001).

Cal1 P. T. Callaghan, "Principles of Nuclear Magnetic Resonance Microscopy", Clarendon Press, Oxford, 1991.

Can1 D. Canet, "Nuclear Magnetic Resonance. Concepts and Methods", John Wiley & Sons, Ltd., Chichester, 1996.

Car1 H. Y. Carr, E. M. Purcell, Effects of Diffusion on Free Precession in Nuclear Magnetic Resonance Experiments, Phys. Rev. 94, 630-638 (1954).

Cas1 F. Casanova, J. Perlo, B Blümich, Nucl. Magn. Reson. Imag. Chem. Eng. (S. Stapf, S. Han, eds.), pp. 107-122. Weinheim, Wiley-VCH 2005.

Cas2 F. Casanova, B. Blümich, Two-Dimensional Imaging with a Single-Sided NMR Probe, J. Magn. Reson. 163, 38–45 (2003).

Cas3 F. Casanova, J. Perlo, B. Blümich, K. Kremer, Multi-echo imaging in highly inhomogeneous magnetic fields, J. Magn. Reson. 166, 76–81 (2004).

Cha1 N. Chandrakumar and S. Subramanian, "Modern Techniques in High-resolution FT-NMR", Springer, New York, 1987.

Chu1 J. A. Chudek and G. Hunter, Nuclear magnetic resonance chemical shift-selective microimaging of samples of degraded rubber hosepipe and of high-impact polystyrene, J. Mater. Sci. Lett. 11, 222 (1992).

Coh1 J. -P. Cohen Addad, NMR and Fractal Properties of Polymeric Liquids and Gels, Prog. NMR Spectrosc. 25, 1 (1993).

Col1 J. Collignon, H. Sillescu, and H.W. Spiess, Pseudo-solid echoes of proton and deuteron NMR in polyethylene melts, Colloid and Polym. Sci. 259, 220 (1981).

Cor1 D. G. Cory, *Annu. Rep. NMR Spectrosc.* **24**, 88 (1992).

Del1 J. -J. Delpuech, ed., "Dynamics of Solutions and Fluid Mixtures by NMR", John Wiley & Sons, Ltd., Chichester, 1995.

Dem1 D. E. Demco, B. Blümich, "Nuclear Magnetic Resonance", Encycl. Polym. Sci. Techn., 2004.

Dem2 D. E. Demco, Tetrahedral Magic Echo, Phys. Lett. 45A, 113 (1973).

Dem3 D. E. Demco and B. Blümich, Solid-state NMR imaging methods. Part I: Strong field gradients, Conc. Magn. Reson. 12, 188-206 (2000).

Dem4 D. E. Demco and B. Blümich, Solid-state NMR imaging methods. Part II: Line narrowing, Conc. Magn. Reson. 12, 269-288 (2000).

Dem5 D. E. Demco and B. Blümich, NMR imaging of materials, Curr. Opp. Solid State Mater. Sci. 5, 195 (2001).

Den1 P. Denner, B. Walker, and T. Willing, *Macromol. Symp.* 119, 339 (1997).

Eid1 G. Eidmann, R. Savelsberg, P. Blümler, B. Blümich, The NMR-MOUSE: A Mobile Universal Surface Explorer, J. Magn. Reson. A122, 104-109 (1996).

Ern1 R. R. Ernst, Nobel Lecture, December 9, 1992.

Ern2 R. R. Ernst, G. Bodenhausen, and A. Wokaun, "Principles of Nuclear Magnetic Resonance in One and Two Dimensions", Clarendon Press, Oxford, 1987.

Fec1 R. Fechete, D. E. Demco, and B. Blümich, Chain orientation and slow dynamics in elastomers by mixed magic-Hahn echo decays, J. Chem. Phys. 118, 5 (2003).

Fed1 V. D. Fedotov and H. Schneider, Structure and dynamics of bulk polymers by NMR method, *NMR, Basic Principles and Progress* Vol. 21, Springer, Berlin, (1989).

Fow1 J. F. Fowler & F. T. Farmer, Conductivity induced in Unplasticized 'Perspex' by X-rays, Nature 175, 516 (1955).

Fri1 H. Friebolin, Ein- und zwei-dimensionale NMR-Spektroskopie, VCH-Verlag, Weinheim, 1988.

Fül1 C. Fülber, B. Blümich, K. Unseld, and V. Herrmann, NMR imaging of Thermal-Oxidative Aging in SBR, Kautsch. Gummi Kunstst. 48, 254 (1995).

Fül2 C. Fülber, K. Unseld, V. Herrmann, K. H. Jakob, and B. Blümich, In situ investigation of SBR vulcanisation: A combined study of ^{1}H-NMR and vulcametry, Colloid Polym. Sci. 274, 191 (1996).

Gas1 L. Gasper, "NMR Relaxation, Spectroscopy and Imaging of Elastomeric Networks", Shaker Verlag, Aachen, 2000.

Gog1 N. O. Goga, K. Kremer, B. Blümich, Zerstörungsfreie Qualitätskontrolle in der Reifenproduktion: Die „NMR-MOUSE", GAK 58, 104–108 (2005).

Gog2 N. O. Goga, A. Pirnau, L. Szabo, R. Smeets, D. Riediger, O. Cozar, B. Blümich, Mobile NMR: Applications to Materials and Biomedicine, J. Optoelectr. Adv. Mat. 8, 1430–1434 (2006).

Gro1 A. Y. Grosberg, A. R. Khokhov, "Statisitcal Physics of Macromolecules", American Instiute of Physics, Woodbury, NY., 1994.

Gut1 A. Guthausen, G. Zimmer, R. Eymael, U. Schmitz, P. Blümler, B. Blümich, Soft-Matter Relaxation by the NMR MOUSE, in: P. Blümler, B. Blümich, R. Botto, E. Fukushima, eds., Spatially Resolved Magnetic Resonance, Wiley-VCH, Weinheim, 195-209 (1998).

Haa1 E. M. Haacke, R.W. Brown, M. R. Thompson, and R. Venkatesan, "Magnetic Resonance Imaging, Physical Principles and Sequence Design", Wiley-Liss, New York, 1999.

Hah1 E. L. Hahn, Spin Echoes, Phys. Rev. 80, 580–594 (1950).

Hah2 E. L. Hahn, Lille Conference Talk, J. Magn. Reson. 179, 9-19 (2006).

Hai1 K. Hailu, R. Fechete, D. E. Demco, B. Blümich, Segmental Anisotropy in Strained Elastomers Detected with a Portable NMR Scanner, Solid State Nucl. Magn. Reson. 22, 327–343 (2002).

Hai2 K. Hailu, R. Fechete, D. E. Demco, B. Blümich, Anisotropy of transverse 1H magnetization relaxation in strained elastomers by the NMR-MOUSE, in: Magnetic Resonance in Colloid and Interface Science, J. Fraissard, O. Lapina, eds., NATO Science Series, Series II: Mathematics, Physics and Chemistry –Vol. 76, Kluwer, Dordrecht, 525–530, 2002.

Har1 A. Hartwig, B. Wolter, NMR- Aufsatztechnik: Neue Online- Methode zum zerstörungsfreien Prüfen? Adhäsion 11, 25–29 (2001).

Hog1 B. J. Hogan, One-Sided NMR Sensor System Measures Soil/Concrete Moisture, Design News, May 5 (1986).

Hou1 D. I. Hoult, R. E. Richards, The signal-to-noise ratio of the nuclear magnetic resonance experiment, J. Magn. Reson. 24, 71-85 (1976).

Hue1 M. D. Hürlimann, D. D. Griffin, Spin Dynamics of Carr-Purcell-Meiboom-Gill-like Sequences in Grossly Inhomogeneous B_0 and B_1 Fields and Application to NMR Well Logging, J. Magn. Reson. 143, 120–135 (2000).

Jac1 J. A. Jackson, L. J. Burnett, F. Harmon, Remote (inside-out) NMR. III. Detection of nuclear magnetic resonance in a remotely produced region of homogeneous magnetic field, J. Magn. Reson. 41, 411-421 (1980).

Kas1 A. Kastler, Le Pompage Optique (à partir de 1950), J. Physique 11, 255 (1950).

Kel1 J. M. B. Kellogg, I. I. Rabi, N. F. Ramsey, J.R., and J. R. Zacharias, An electrical quadrupole moment of the deuteron; Magnetic moments of the proton and the deuteron-radiofrequency spectrum of H_2 in various magnetic fields; Electric quadrupole moment of the deuteron-radio-frequency spectra of HD and D2 molecules in a magnetic field, Phys. Rev. 55, 318 (1939); 56, 728 (1939); 57, 677 (1940).

Kim1 R. Kimmich, "NMR: Tomography, Diffusiometry, Relaxometry", Springer, Berlin, 1997.

Kle1 R. L. Kleinberg, A. Sezginer, D. D. Griffin, M. Fukuhara, J. Magn. Reson. **97**, 466 – 485 (1992).

Kle2 R.L. Kleinberg, in Encyclopedia of NMR (D.M. Grant, R.K. Harris, eds.), 4960 – 4969, New York: Wiley 1996.

Kle3 B. Klei and J. L. Koenig, NMR imaging of the competitive vulcanization of natural rubber and polybutadiene blends, Acta Polym., 48, 199 (1997).

Kli1 M. Klinkenberg, P. Blümler, and B. Blümich, ^{2}H-NMR lmaging of Stress in Strained Elastomers, Macromolecules 30, 1038 (1997).

Knö1 M. Knörgen, U. Heuert, H. Schneider, P. Barth, and W. Kuhn, Spatially resolved and integral NMR investigation of the aging process of carbon black filled natural rubber, Polym. Bull. 38, 101 (1997).

Knö2 M. Knörgen, U. Heuert, H. Menge, and H. Schneider, The use of NMR relaxation and NMR imaging in studying the aging of rubber, Angew. Makromol. Chem. 261/262, 123 (1998).

Lau1 P. C. Lauterbur, Image formation by induced local interactions – examples employing nuclear magnetic resonance, Nature 242 (1973) 190.

Lev1 M. H. Levitt, "Spin Dynamics", John Wiley & Sons, Ltd., Chichester, 2001.

Lit1 V. M. Litvinov, and Prajna P De, "Spectroscopy of Rubbers and Rubbery Materials", Rapra Technology, Shawbury, Shrewsbury, Shropshire, SY4 4NR, United Kingdom, 2002.

Man1 P. Mansfield, P.K. Grannell, NMR 'diffraction' in solids?, J. Phys. C Solid State 6, L422 (1973).

Man2 P. Mansfield and P. G. Morris, NMR imaging in biomedicine, Advanced Magnetic Resonance, Suppl. 2, Academic Press, New York, 1982.

Man3 P. Mansfield, R. Bowtell, and S. Blackband, Ingress of water into solid nylon-6.6, J. Magn. Reson. 99, 507 (1992).

Mar1 G. E. Martin and A.S. Zektzer, Two-dimensional NMR Methods for Establishing Molecular Connectivity, VCH Verlagsgesellschaft, Weinheim, 1988.

Mar2 J. L. Markley, W. T. Horsley, M. P. Klein, Spin-Lattice Relaxation in Slowly Relaxing Complex Spectra, J. Chem. Phys. 55, 3604–3605(1971).

Mat1 G. A. Matzkanin in: Nondestructive Characterization of Materials, in: P. Höller, G. Dobmann, C. O. Ruud, R. E. Green, eds., “Nondestructive Characterization of Materials”, Springer, Berlin, 1989, pp. 655-669.

McD1 P. J. McDonald, Stray Field Magnetic Resonance Imaging, Prog. NMR Spectrosc. 30, 69 (1997).

Meh1 M. Mehring, “Principles of High Resolution NMR Spectroscopy in Solids”, 2nd ed., Springer, Berlin, 1983.

Mei1 S. Meiboom, D. Gill, Modified Spin-Echo Method for Measuring Nuclear Relaxation Times, Rev. Sci. Instrum. 29, 688-691 (1958).

Mik1 F. P. Miknis, A. T. Pauli, L. C. Michon, and D. A. Netzel, NMR Imaging Studies of Asphaltene Precipitation in Petroleum Asphalts, Fuel 77, 399 (1998).

Mik2 F. P. Miknis and L. C. Michon, Some Applications of Nuclear Magnetic Resonance. Imaging to Crumb Rubber Modified Asphalts, Fuel 77, 393 (1998).

Mil1 A. A. Miller, E. J. Lawton, J. S. Balwit, The Radiation chemistry of hydrocarbon polymers: Polyethylene, Polymethylene and Octacosane, J. Phys. Chem. 60, 599(1956).

Mun1 M. Munowitz and A. Pines, Principles and Applications of Multiple-Quantum NMR, Adv. Chem. Phys. 66, 1 (1987).

Pal1 P. Palmas, R. Colsenet, L. Lemaire, and M. Sebban, Ageing of EPDM elastomers exposed to γ-radiation studied by ^{1}H broadband and ^{13}C high-resolution solid-state NMR, Polymer 44, 4889 (2003).

Par1 A. A. Parker, J. J. Marcinko, P. Rinaldi, D. P. Hendrick, and W. Ritchey, A relationship between NMR cross-polarization rates and dynamic storage modulae of polymers J. Appl. Polym. 48, 677 (1993).

Per1 J. Perlo, F. Casanova, B. Blümich, Profiles with microscopic resolution by single-sided NMR, J. Magn. Reson. 176, 64 – 70 (2005).

Per2 J. Perlo, F. Casanova, B. Blümich, 3D imaging with a single-sided sensor: an open tomograph, J. Magn. Reson. 166 (2004) 228–235.

Per3 J. Perlo, Single-Sided NMR Tomography, dissertation, RWTH Aachen University, 2006.

Pow1 J. G. Powles and P. Mansfield, Double-pulse nuclear-resonance transients in solids, Phys. Lett. 2, 58 (1962).

Pra1 P. Prado, B. Blümich, U. Schmitz, One Dimensional Imaging with a Palm-Size NMR-Probe, J. Magn. Reson. 144, 200 – 206 (2000).

Pra2 P. J. Prado, NMR hand-held moisture sensor, Magn. Reson. Imaging 21, 397 – 400 (2003).

Pur1 E. U. Purcell, H. C. Torrey, R. V. Pound, Resonance Absorption by Nuclear Magnetic Moments in a Solid, Phys. Rev. 69, 37-38 (1946).

Rab1 I. I. Rabi, Space Quantization in a Gyrating Magnetic Field, Phys. Rev. 51, 652 (1937).

Rab2 I. I. Rabi, J.R. Zacharias, S. Millman, and P. Kusch, A New Method of Measuring Nuclear Magnetic Moment, Phys. Rev. 53, 318 (1938).

Rab3 I. I. Rabi, S. Millman, P. Kusch, J. R. Zacharias, The Molecular Beam Resonance Method for Measuring Nuclear Magnetic Moments The Magnetic Moments of $_3Li^6$, $_3Li^7$ and $_9F^{19}$, Phys. Rev. 55, 526 (1939).

Raf1 D. Raftery and B. F. Chmelka, Xenon NMR spectroscopy, NMR Basis Princ. Prog. 30, 111 (1994).

Rah1 A. Rahman, “Nuclear Magnetic Resonance, Basic Principles”, Springer, NY., 1986.

Ran1 M. A. Rana and J. L. Koenig, Observation of Spatial Inhomogeneities in N-tert-Butylbenzothiazolesulfenamide Sulfur Cured High-Vinyl Polybutadiene Using NMR Imaging, Macromolecules 27, 3727 (1994).

Rhi1 W.-K. Rhim, A. Pines, and J. S. Waugh, Time-reversal experiments in dipolar-coupled spin systems, Phys. Rev. B 3, 684 (1971).

Sar1 M. Sardashti, B. A. Baldwin, and D. J. O'Donnell, NMR imaging of polyethylene pipes, J. Polym. Sci., B: Polym. Phys. 33, 571 (1995).

Sch1 J. Schraml and J.M. Bellama, "Two-dimensional NMR Spectroscopy", Wiley Interscience, New York, 1988.

Sch2 K. Schmidt-Rohr and H.W. Spiess, "Multidimensional Solid State NMR and Polymers", Academic Press, New York, 1994.

Sch3 I. Schnell and H. W. Spiess, High-Resolution 1H NMR Spectroscopy in the Solid State: Very Fast Sample Rotation and Multiple-Quantum Coherences, J. Magn. Reson. Adv. Magn. Reson. 151, 153 (2001).

Sch4 H. Schneider and H. Schmiedel, Negative time development of a nuclear spin system, Phys. Lett. 30A, 298 (1969).

Sch5 C. Schwarzbauer, J. Zange, H. Adolf, R. Deichnmann, U. Noth, and A. Haase, Fast Measurement of Temperature Distributions by Rapid T_1 Mapping, J. Magn. Reson. B 100, 178 (1995).

Sch6 M. Schneider, D. E. Demco, and B. Blümich, NMR images of proton residual dipolar coupling from strained elastomers, Macromolecules 34, 4019 (2001).

Sch7 M. Schneider, D. E. Demco, and B. Blümich, 1H NMR Imaging of Residual Dipolar Couplings in Cross-Linked Elastomers: Dipolar-Encoded Longitudinal Magnetization, Double-Quantum and Triple-Quantum Filters, J. Magn. Reson. 140, 432 (1999).

Sha1 S. Sharma, F. Casanova, W. Wache, A. Segre, B. Blumich, Analysis of Historical Porous Building Materials by the NMR-MOUSE, Magn. Reson. Imaging 21, 249 (2003).

Sim1 G. Simon and H. Schneider, Macromol. Chem. Macromol. Symp. 52, 233 (1991).

Sku1 V. E. Skurat, I. I. Dorofeev, The transformations of organic polymers during the illumination by 147 and 123,6 nm light, Ang. Makrom. Chem. 216 (1994); 205 (3877).

Smi1 S. R. Smith and J. L. Koening, Observation of crosslink density dispersion in sulfur donor-vulcanized polybutadiene using NMR imaging, Macromolecules 24, 3496 (1991).

Sot1 P. Sotta, C. Fülber, D. E. Demco, B. Blümich, and H. W. Spiess, The effect of Dipolar Interactions on the NMR Relaxation in Crosslinked Elastomers, Macromolecules 29, 6222 (1996).

Spy1 A. Spyros, R. Kimmich, B. H. Briese, and D. Jenddrossek, 1H NMR Imaging Study of Enzymatic Degradation in Poly(3-hydroxybutyrate) and Poly(3-hydroxybutyrate-co-3-hydroxyvalerate). Evidence for Preferential Degradation of the Amorphous Phase by PHB Depolymerase B from *Pseudomonas lemoignei*, Macromolecules 30, 8218 (1997).

Str1 J. H. Strange, Echoes and Imaging in Solids, Phil. Trans. Soc. Lond. A 333, 427 (1990).

Tyc1 R. Tycko, ed., Nuclear Magnetic Resonance of Molecular Dynamics, Kluwer Academic Publishers, Dordrecht, 1994.

Vla1 M. T. Vlaardingerbroek and J. A. den Boer, "Magnetic Resonance Imaging", 2nd ed., Springer, Berlin, 1999.

Wei1 J. Weiss, Chemical effects in the irradiation of polymers in the solid state, J. Polym. Sci. 29, 425 (1958).

Woe1 D. E. Woessner, The Early Days of NMR in the Southwest, Concepts Magn. Reson. 13, 77-102 (2001).

Xia1 Y. Xia, Contrast in NMR imaging and microscopy, Conc. Magn. Reson. 8, 205 (1996).

Zim1 G. Zimmer, A. Guthausen, U. Schmitz, K. Saito, B. Blümich, Weathering investigation of PVC coatings on iron sheets by the NMR MOUSE, Adv. Mater. 9, 987(1997).

Zim2 G. Zimmer, A. Guthausen, and B. Blümich, Characterization of cross-link density in technical elastomers by the NMR-MOUSE, Solid State Nucl. Magn. Reson. 12, 183-190 (1998).

Acknowledgements

I would like to express my gratitude to all those who gave a piece of their knowledge, kindness and always expensive time, to make this work complete.

I am very grateful to Prof. Bernhard Blümich for the invaluable opportunity of being part of his group during the last three years, for all interesting discussions and permanent impulse he gave me.

I would like to express my special thanks to Prof. Dan E. Demco for his theoretical advice and answers to NMR-related problems as well as for his constant encouragement and helpfulness. Many thanks also for carefully reading and correcting this work.

I would like to thank Prof. Wolfgang Stahl for accepting to be the co-referent of my PhD thesis.

Many thanks are ought to Dr. Federico Casanova for introducing me to the world of single-sided NMR, for the many hours of useful discussions on low-field NMR topics and for his practical help. Thank you for being around anytime I needed.

I would like to say thanks to Dr. Kai Kremer for the great help, collaboration, and guidance he offered me from my first day in Aachen.

Special thanks are ought to my colleague Dr. Adrian Parnau from the "Babes-Bolyai" University of Cluj-Napoca, to Dr. Ralf Smeets from the Maxillofacial Surgery Department of UK Aachen, and to "my master students": Agnes Haber, Robert Ferencz, Ioan Botiz (Bobo), and Laszló Szabó for the nice collaboration and great work we did together.

Many thanks to Dipl.- Ing. Michael Adams for his assistance in the electronic problems related to the low-field NMR spectrometers and to Klaus Kupferschläger for his constant helpfulness and great hand in building "impossible" parts for my sensors.

I would like to say thanks to my office mates, Claudiu Melian and Jürgen Kolz for being always kind and helpful.

Many thanks to Dr. Mihai Voda, and Dr. Markus Küppers, for their support in computer-related problems.

A big thanks to my colleagues and good friends from the Tex-MC group, Cristian Vaida, Dragos Popescu and Mark Hans, for their caring and the nice time we had together these years.

Many thanks are also ought to all those group members, too numerous to mention, whose support was continuous all these years.

Thanks also to Professor. Dr. Onuc Cozar from the Faculty of Physiscs, the “Babes-Bolyai” University of Cluj-Napoca, for the chance of coming and studying at RWTH Aachen as a Socrates Student.

On the top of all I would like to say thanks to my mother Elizabeta and my father Nicolae. Many thanks to your words and thoughts for always blessing me; thank you for believing in me, and for always giving me the strength and reason to go straight. I am also blessed to have Elisabeta and Mihai as sister and brother, who always keep my momentum moving on.

The last thoughts are for my beloved wife Ljubow. Thank you for constantly encouraging me, for all your love, undestanding, and permanent support which only superlatives can describe.

Curriculum Vitae

Nicolae-Octavian Goga

Birth date and place: 22 March 1980, Satu-Mare/Romania

E-mail: no_goga@ yahoo.com

Nationality: romanian

Education/Qualifications

20.08.2007	Defence for the Doctoral Degree in Natural Sciences
Thesis:	"Non-destructive characterization of materials by single-sided NMR"
2004-2007	Ph.D. at "Makromolekulare Chemie", (Prof. B. Blümich) RWTH-Aachen, Germany
2002-2003	Master of Science (Biophysics and Medical Physics), Babes-Bolyai University, Cluj-Napoca, Romania, Faculty of Physics, in collaboration with Makromolekulare Chemie, RWTH-Aachen, Germany
Dissertation:	"Characterization of elastomers by the NMR-MOUSE®"
1998-2002	Dipl. Phys., Faculty of Physics, Babes-Bolyai University, Cluj-Napoca, Romania
Diploma:	"Method and apparatus for the physiological stress reduction in human pacients"
1994-1998	Highschool (chemistry-biology class), "Ioan Slavici" National College, Satu-Mare, Romania
1990-1994	Secondary School, Livada (Satu-Mare), Romania
1986-1990	Primary School, Livada (Satu-Mare), Romania

Work/Research experience

2004– Research at Lehrstuhl für Makromolekulare Chemie, ITMC, RWTH Aachen

2003–2004 Research at Babes-Bolyai University, Cluj-Napoca, Romania, Faculty of Physics

Seminars and laboratory work with first and second year students at the Faculty of Physics

Publications

N. O. Goga, K. Kremer, B. Blümich, Zerstörungsfreie Qualitätskontrolle in der Reifenproduktion: Die „NMR-MOUSE“, GAK 58-2 (2005).

B. Blümich, F. Casanova, J. Perlo, S. Anferova, V. Anferov, K. Kremer, N. Goga, K. Kupferschläger, M. Adams, Advances of Unilateral, Mobile NMR in Nondestructive Materials Testing, Magn. Reson. Imag. 23, 197-201 (2005).

N. O. Goga, A. Pirnau, L. Szabo, R. Smeets, D. Riediger, O. Cozar, and B. Blümich, Mobile NMR: applications to materials and biomedicine, J. Optoelectr. Adv. Mat. Vol. 8, No. 4, 1430-1434 (2006).

J. Kolz, N. Goga, F. Casanova, T. Mang, and B. Blümich, Spatial Localization with Single-Sided NMR Sensors, Appl. Magn. Reson. 32, 171-184 (2007).

N. O. Goga, D. E. Demco, J. Kolz, R. Ferencz, F. Casanova, and B. Blümich, Surface UV aging of elastomers investigated with microscopic resolution by single-sided NMR, J. Magn. Reson. 192, 1-7 (2008).